Investigating the potential magnetic origin of wind variability in OB stars

by

Alexandre David-Uraz

A thesis submitted to the
Department of Physics, Engineering Physics & Astronomy
in conformity with the requirements for
the degree of Doctor of Philosophy

Queen's University
Kingston, Ontario, Canada
May 2016

Abstract

In this thesis, the origin of large-scale structures in hot star winds, believed to be responsible for the presence of discrete absorption components (DACs) in the absorption troughs of ultraviolet resonance lines, is constrained using both observations and numerical simulations. These structures are understood as arising from bright regions on the stellar surface, although their physical cause remains unknown.

First, we use high quality circular spectropolarimetric observations of 13 well-studied OB stars to evaluate the potential role of dipolar magnetic fields in producing DACs. We perform longitudinal field measurements and place limits on the field strength using Bayesian inference, assuming that it is dipolar. No magnetic field was detected within this sample. The derived constraints statistically refute any significant dynamical influence from a magnetic dipole on the wind for all of these stars, ruling out such fields as a cause for DACs.

Second, we perform numerical simulations using bright spots constrained by broad-band optical photometric observations. We calculate hydrodynamical wind models using three sets of spot sizes and strengths. Co-rotating interaction regions are yielded in each model, and radiative transfer shows that the properties of the variations in the UV resonance lines synthesized from these models are consistent with those found in observed UV spectra, establishing the first consistent link between UV spectroscopic

line profile variability and photometric variations and thus supporting the bright spot paradigm (BSP).

Finally, we develop and apply a phenomenological model to quantify the measurable effects co-rotating bright spots would have on broadband optical photometry and on the profiles of photopheric lines in optical spectra. This model can be used to evaluate the existence of these spots, and, in the event of their detection, characterize them. Furthermore, a tentative spot evolution model is presented. A preliminary analysis of its output, compared to the observed photometric variations of ξ Persei, suggests the possible existence of "active longitudes" on the surface of this star.

Future work will expand the range of observational diagnostics that can be interpreted within the BSP, and link phenomenology (bright spots) to physical processes (magnetic spots or non-radial pulsations).

Acknowledgments

First and foremost, my warmest thanks go to my supervisor, Prof. Gregg Wade, from whom I have learned tremendously over the last 4 years. He has helped me at every step of the way, displaying great patience, humour and martial arts skills (especially when pranked at supervisory committee meetings). I also want to thank Prof. Dave Hanes, my co-supervisor, for his support, as well as my new postdoctoral supervisor, Prof. Véronique Petit, for her helpful guidance.

A special thanks as well to my academic brothers. Jason, our overlap was short but very helpful (for me at least)! To James, I say "hang dai", to Zsolt, "egészségedre", and finally to Matt, "haha, I won". My gratitude also extends to the other graduate students, staff and professors at both Queen's University and the Royal Military College of Canada.

Finally, to my close ones who have supported me, I would like say thank you. That includes countless friends and colleagues in Kingston and Montreal (yes, I truly am *that* popular), but in particular my roommate Amanda, who undoubtedly contributed to delay my graduation by the length of a few games of GTA V (worth it), my mother Johanne, who *literally* made all of this possible, and my sweetheart Laure, who has had to endure a lifetime of whining in a mere few years.

Du fond du cœur, merci à vous tous!

Statement of Originality

The work presented in this thesis is constituted of published, and soon-to-be published, material. These studies were collaborative efforts, but in each case, as lead author, I wrote the contents and was responsible for most of the analysis presented in them. Here is a more detailed account of my involvement in each of these studies.

For the study of dipolar fields, I gathered the archival data, performed normalization of the spectropolarimetric observations, crafted made-to-measure line masks for each star and used them to perform Least-Squares Deconvolution and to calculate longitudinal field measurements. However, I did not perform the Bayesian inference, but I compiled all of the results and wrote, edited and submitted the paper.

For the hydrodynamical models, the codes used to perform both the hydrodynamical models and the Sobolev Exact Integration were already in existence, but I modified them, ran them and performed all subsequent analysis of the results, also writing and editing the paper.

Finally, for the empirical modelling, using a code that already existed to implement magnetic spots, I stripped it to its core and built it to my specifications (to produce synthetic light curves and spectra). I also wrote the spot generation module, ran all codes and compiled all the results, writing and editing the paper.

Contents

List of Tables

List of Figures

Abbreviations

Here is a list of abbreviations used throughout this thesis.

BRITE	BRIght Target Explorer
BSP	Bright Spot Paradigm
CFHT	Canada-France-Hawaii Telescope
CIR	Corotating Interaction Region
DAC	Discrete Absorption Component
H-R	Hertzsprung-Russell
IUE	International Ultraviolet Explorer
LBV	Luminous Blue Variable
LDI	Line Deshadowing Instability
LDW	Line Driven Wind
LP	Large Program
LPV	Line Profile Variability
LSD	Least Squares Deconvolution
MHD	Magnetohydrodynamical

MOST	Microvariability and Oscillations of STars
RTE	Radiative Transfer Equation
SC	Survey Component
SNR	Signal-to-Noise Ratio
TBL	Télescope Bernard-Lyot
TC	Target Component
UV	Ultraviolet
WR	Wolf-Rayet

Chapter 1

Introduction

1.1 Massive stars

A star is a self-gravitating ball of plasma which undergoes thermonuclear reactions in its core. The energy generated by these reactions is transported (either radiatively or convectively) to the star's photosphere, or effective "surface", from where it propagates in every direction in the form of electromagnetic radiation[1]. The closest star to us is the Sun, and as such it is by far the best-studied of all stars. It is considered to be a fairly "average" star; however, stars are very diverse and their properties span a huge parameter space. For instance, they range in mass[2] from about 0.08 $M_\odot$ [Richer et al., 2006] to approximately 300 $M_\odot$ [Crowther et al., 2010][3].

[1]Since stars do not possess a rigid outer boundary, the *stellar surface* (or *photosphere*) is defined as the wavelength-dependent limit from which roughly half of the emitted light can escape the atmosphere; the temperature at that limit is called the *effective temperature*, and the spectral energy distribution (SED) of the light that leaves the stellar surface can be approximated by that of a black body with that effective temperature.

[2]Stellar properties are often expressed in terms of solar properties, which are denoted by a subscript consisting of a circle with a dot in its center.

[3]It should be noted that this upper limit is still controversial and the object of active studies.

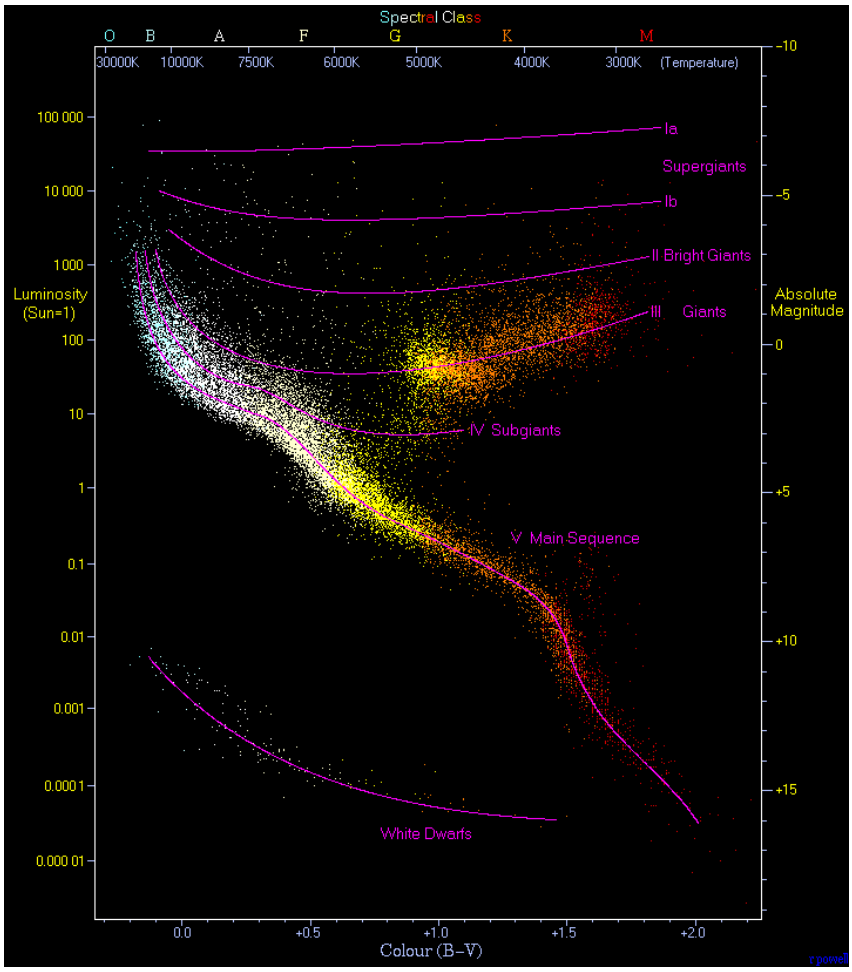

Figure 1.1: H-R diagram, with massive stars occupying the upper left part (Courtesy of Richard Powell / CC BY-SA-2.5).

Two other important stellar properties are total luminosity and effective temperature. They are often plotted one against another in what is called a *Hertzsprung-Russell diagram* (or H-R diagram), an example of which is shown in Fig. 1.1. A few important characteristics of stars can be identified by looking at this diagram:

- Stars range in effective temperature from about 2.3 kK to nearly 50 kK, and in luminosity from about $10^{-5}L_{\odot}$ to $10^{6}L_{\odot}$.

- Stars form "sequences" in this diagram which relate to their evolutionary state. The thick sequence which crosses the diagram diagonally is called the *main sequence* and comprises over 90% of all stars; it correponds to the core hydrogen-burning phase.

The position of a star along the main sequence depends on its mass: more massive stars will tend to be more luminous and hotter, while less massive stars are dimmer and cooler. As both the most luminous and the hottest stars in the universe, *massive stars* occupy the upper left part of the H-R diagram. In terms of spectral type, massive stars, also designated as *OB stars*, range from the earliest spectral types up to B2 on the main sequence (later types may also be included, up to B9, for evolved stars with higher luminosity classes, from IV to I, Reed 2003). Massive stars are distinguished from their lighter cousins by their ultimate fate: while lower-mass stars end their lives quietly by shedding their outer envelopes, thus forming planetary nebulæ and revealing their degenerate cores, which are henceforth designated as *white dwarfs*, massive stars on the other hand end their lives in a catastrophic explosion called a *supernova*, leaving behind a neutron star or a black hole remnant. Current models place a lower initial mass limit of about 8 times the mass of the Sun for such a scenario to unfold [Heger et al., 2003]. Hence massive stars are formally defined as those with initial masses of $8M_{\odot}$ and above.

Massive stars are, in many ways, the "rockstars" of the Universe. Even though they are quite rare, they are the most noticeable stellar objects: massive stars account, in a typical galaxy, for 1% of the total number of stars, but for 99% of the total light budget[4]. They also live dramatic lives, literally burning themselves out: an O star's

[4]These fractions are estimated using a Kroupa initial mass function [Kroupa, 2001] and using $L_{\rm bol} \sim M^{3.5}$.

lifetime is about 10 million years, whereas the lifetime of a star similar to our Sun is rather of the order of 10 *billion* years, a factor of 10^3 larger. These shorter evolutionary timescales also increase their influence on the galactic medium, since over the course of the Sun's lifetime, up to a thousand generations of massive stars will have come and gone. Finally, even once they are gone, their legacy lasts on: massive stars significantly alter their environment, be it through their dense supersonic radiatively driven winds, or their spectacular deaths as supernovae, injecting into the interstellar medium chemically enriched matter as well as tremendous amounts of energy and momentum. Because of their important effects on their surroundings, as well as the distinct and unique physical phenomena involved in these interactions[5], we aim to achieve a more intimate knowledge of these stars.

One of the most important processes affecting OB stars during their lifetimes is the continuous loss of mass via supersonic, radiatively-driven *stellar winds*. The existence of this process was first evidenced by the discovery of unusual spectral lines in the Luminous Blue Variable (LBV) P Cygni [Maury and Pickering, 1897], later interpreted as resulting from an expanding envelope (e.g., McCrea 1929, Beals 1929, 1932). Typical mass-loss rates of O stars are of the order of $10^{-7} M_\odot$/yr (e.g., Vink et al. 2001), as compared to only $10^{-14} M_\odot$/yr in the case of the Sun, and their winds can reach velocities upwards of 2000-3000 km/s.

Mass loss has been playing an increasingly important role in evolutionary models (e.g. Cuntz and Stencel 1992) for massive stars, as it contributes to mixing and fundamentally changes their stellar parameters with time (e.g. reduces the rotation rate by transporting angular momentum away from the star). Mass loss also accounts

[5]Given the intense conditions found in these stars, which cannot be reproduced on Earth, they consitute in a way a "laboratory" for extreme physics.

for various types of interaction between a massive star and its surroundings. Indeed, stellar winds impart energy and momentum to the circumstellar medium, resulting in shocks, bubbles and other similar structures (for a nice review of such structures, see Chu 2003, for a basic theoretical model of these shocks, refer to Weaver et al. 1977). In parallel, the huge ionizing UV flux emitted by OB stars – the fundamental source of the wind's kinetic energy – also influences their immediate neighbourhood, sometimes sparking new bursts of star formation around OB associations. The physical underpinnings of massive star winds will be explored in further detail in the next chapter.

1.2 Wind variability of massive stars

OB stars are known to exhibit various forms of variability. These variations can manifest themselves in different types of observational data. When changes occur within the absorption or emission lines of their spectra, they are designated as *line profile variability* (LPV). Such variability can originate from the stellar surface or from the wind, depending on the lines that are being studied. Photospheric LPV can be of pulsational origin, or it can possibly be caused by inhomogeneities on the stellar surface (e.g., chemical abundance spots), whereas wind variability arises from structures in the stellar outflow.

We can distinguish between two major timescales for LPV in the wind-sensitive lines of hot stars. Short-term variability occurs on timescales varying from minutes to hours, and is usually due to *small-scale* wind structures, which arise stochastically. Massive star winds are not smooth and continuous, but rather "clumpy". This is partly due to inherent instabilities in the driving mechanism, e.g., Line Deshadowing

Instability (LDI; Owocki et al. 1988, Feldmeier 1995). These clumps can influence the spectrum (this is particularly observed in the case of very evolved Wolf-Rayet stars, where the clumps appear as small spikes travelling atop the broad emission lines in their spectra). Evidence of spectral features due to clumps is found at different evolutionary stages of the most massive stars [Lépine and Moffat, 2008]. They can also lead to forms of variability which are observable through means other than spectroscopy. For instance, wind-embedded shocks often generate X-rays, so stars with strong, clumpy winds can be strong X-ray emitters and show X-ray variability [Hillier et al., 1993].

Long-term variability occurs on longer timescales, typically days, weeks or even longer. Such variability is usually believed to be caused by coherent, *large-scale* structures in the wind. For instance, in close massive binaries, the winds from both components of the system collide, producing a shock cone which leads to excess emission. This emission is modulated by the orbital period of the binary and can be modelled to provide information about the interaction geometry, and ultimately about the winds of each component (e.g., Luehrs 1997, David-Uraz et al. 2012).

When massive stars are in the later stages of their lives, they sometimes undergo extreme eruption episodes, which cause important optical photometric variability (one notable case being the famous luminous blue variable η Carinae, which underwent a *great eruption* in 1843, which led to a brightening of almost 2 magnitudes, e.g., Smith and Frew 2011). Such changes to the global properties of the atmosphere and wind of a star are typically accompanied by a change in spectral type as well.

A particularly interesting class of long-term variability occurs in seemingly single stars, and might possibly inform us about the photospheric properties of massive

stars and the surface-wind interface. Such variability includes phase bowing, which appears as a modulation of the optical depth in the absorption trough occuring quasi-simultaneously at all velocities (as in HD 64760, Fullerton et al. 1997), and most importantly discrete absorption components (DACs), which are inferred to be caused by azimuthal structures extending through the wind (an hypothesis which is partly tested in this thesis)[6].

DACs constitute one of the most important forms of LPV in the spectra of hot stars since they are inferred to be ubiquitous in OB stars [Howarth and Prinja, 1989]. This suggests that they result from a very general formation mechanism common to all massive stars. Therefore, finding their origin equates to obtaining a better global understanding of hot massive stars.

Interestingly, DACs also appear in the spectra of central stars of planetary nebulae (CSPN; e.g., Prinja et al. 2012). These objects correspond to a transition stage in lower mass stars between the asymptotic giant branch and white dwarf phases where the naked core is still very hot, with a surface temperature comparable to that of an OB star. This might suggest an even more fundamental underlying cause.

As their name suggests, DACs appear as narrow absorption features, in the UV resonance lines of massive stars – spectral lines that are formed in the outer regions of the atmosphere and are typically used to diagnose wind processes. Over time, DACs migrate through the wind velocity space; this pattern is illustrated in Fig. 1.2, which shows a time-series of spectra, with distinct diagonal features travelling bluewards as time advances. Coherent modulation of other features (e.g. recombination lines like Hα, Kaper et al. 1997, as well as UV excited state lines, Massa and Prinja 2015) independently indicates, since these features can probe different parts of the wind,

[6]For a more extensive review of wind variability in OB stars, see [Fullerton, 2003].

that the structures inferred to be responsible for DACs extend through the entire range of the wind.

DACs have recurrence periods which are correlated with their star's projected rotational velocity, $v \sin i$, suggesting that they are related to stellar rotation [Prinja, 1988]. The recurrence periods are typically shorter than the rotation period of the star (as inferred from the projected rotational velocity and the stellar radius), with usually two DACs appearing per period (although in some cases it can be three or more, but always an integer, Kaper et al. 1996). However, they are not strictly periodic, since taken at different epochs, they do not remain in phase. This suggests that whatever structure causes them might be transient in nature.

Mullan [1986] observed that DACs could possibly be explained using Corotating Interaction Regions (CIR), similar to those observed in the solar wind. CIRs are large-scale, spiral-like, azimuthal structures in the stellar wind with enhanced density; as the star rotates, the part of the CIR which intersects with the line of sight becomes more and more distant from the surface of the star. Given the velocity law for the wind[7], this means that it is observed at higher velocities towards the observer, corresponding to an increasing blueshift.

Apart from their migration through the velocity space, DACs follow other characteristic patterns. Indeed, quantitative analysis of their behaviour provides a greater insight into their evolution: as they travel towards terminal velocity, they become stronger and narrower (see Fig. 1.4). Simulations of CIRs should reproduce these trends to be considered successful.

This scenario has been further investigated by Cranmer and Owocki [1996], who have conducted hydrodynamical simulations to evaluate whether CIRs represent a

[7]The wind accelerates away from the star, as will be shown in the following chapter.

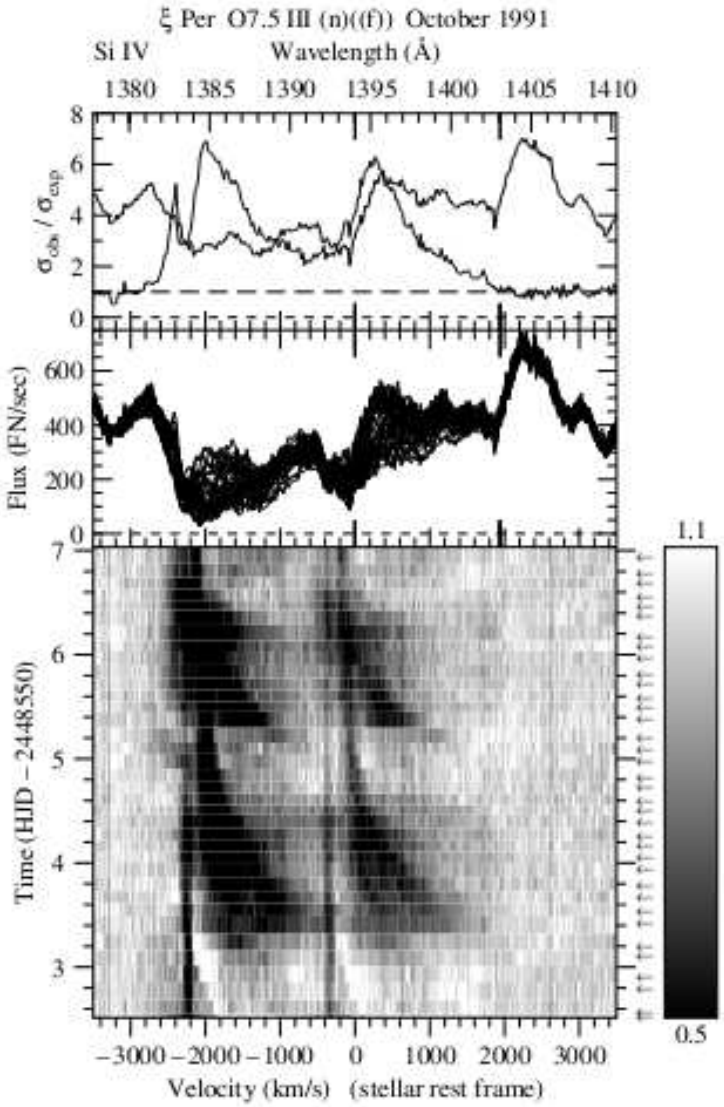

Figure 1.2: Time-series of the quotient spectra for the Si IV resonance doublet (λ1394, λ1402) from the star ξ Per; the top panel shows the reference spectrum (grey line) by which all the other spectra (shown in the middle panel) were divided to obtain these profiles, as well as the level of variability (black line). The vertical axis in the bottom panel corresponds to time, and the greyscale corresponds to the quotient spectra, in which DACs are seen to migrate through the absorption troughs in a cyclical manner (Kaper et al. 1997; reproduced with permission © ESO).

viable process to create DAC-like variability in the spectra of a star. In their model, CIRs are created by a perturbation at the base of the wind which either enhances or diminishes the outflow locally. These perturbations can take two generic forms: either a bright "hot" spot, driving a slower, but denser wind, or a dark "cold" spot, driving a faster, sparser wind. The CIRs are then created by the shock between the wind driven by these spots and the rest of the wind as the star rotates, creating a "garden hose" effect, with the shock region bowing around the star in a spiral form (see Fig. 1.3). This study concluded that the model most capable of producing realistic DAC signatures is one with bright spots. However, no physical explanation is offered as to what can cause these spots.

Two main hypotheses have been proposed to explain the physical origin of DACs [Kaper et al., 1997]: magnetic fields and non-radial pulsations (NRP). Some stars observed to possess DACs have also been shown to host NRPs, thus suggesting that there might be a link between both phenomena (e.g., de Jong et al. 1999, 2001). NRPs also cause LPV in optical lines, and are believed to drive CIRs by dividing the surface into areas with different properties (e.g., velocity, temperature). However, since DACs are believed to occur most often twice per rotational cycle, it has also been very tempting to imagine a model with a large-scale dipolar poloidal magnetic field producing two diametrically opposed hot spots at the surface of the star, thus producing CIRs in the wind and DACs in the spectra (not only is this option tempting, but it is reasonable given that the magnetic fields which have been detected on the surfaces of OB stars mostly have this configuration; Wade et al. 2014). Furthermore, some studies have suggested that NRPs might not explain the presence of DACs in all stars [Henrichs et al., 1994], thus favoring the magnetic hypothesis. Magnetic

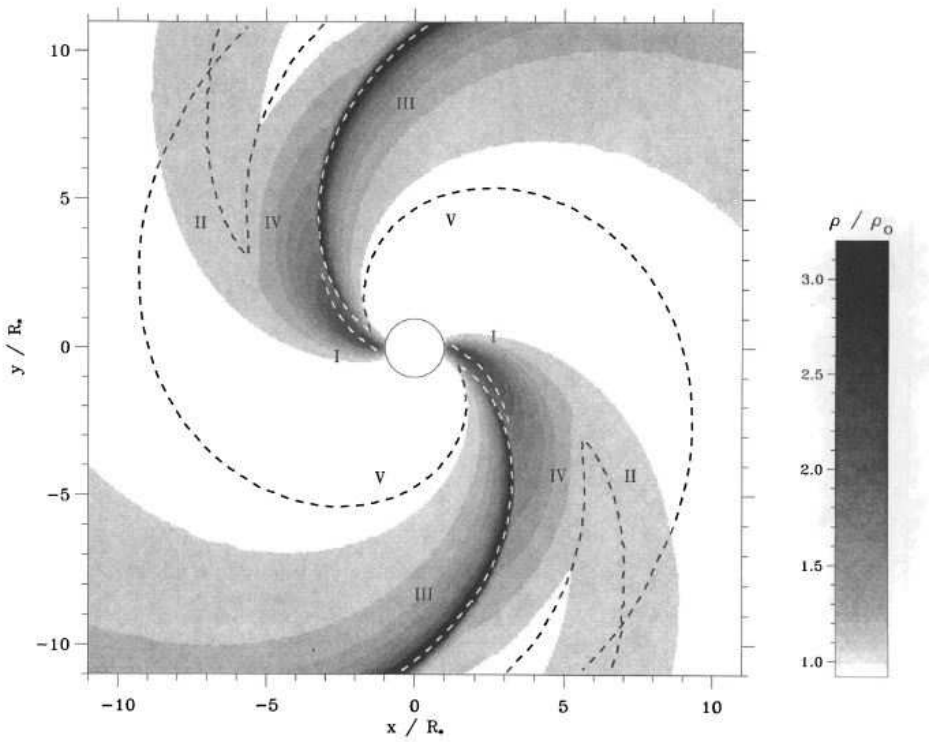

Figure 1.3: Density plot of the stellar wind in the equatorial plane of a rotating star, as derived by Cranmer and Owocki [1996]; it shows two diametrically-opposed CIRs generated by *ad hoc* hot spots placed at the surface of the star. Darker regions correspond to higher density, as indicated by the greyscale on the right. The numbered regions correspond to different features relating to material being shocked as the star rotates. © AAS. Reproduced with permission.

fields are already known to produce other forms of LPV, but they are certainly not detected in all OB stars [Schnerr et al., 2008]. Finally, the existence of weak, small-scale magnetic fields has been proposed by Cantiello and Braithwaite [2011] (this will be discussed in greater detail in Sect. 2.2.3). Such magnetic "spots" would constitute an attractive physical counterpart to the phenomenological "bright spots" used by Cranmer and Owocki [1996]. A summary of these hypotheses and their advantages and problems is presented in Table 1.1.

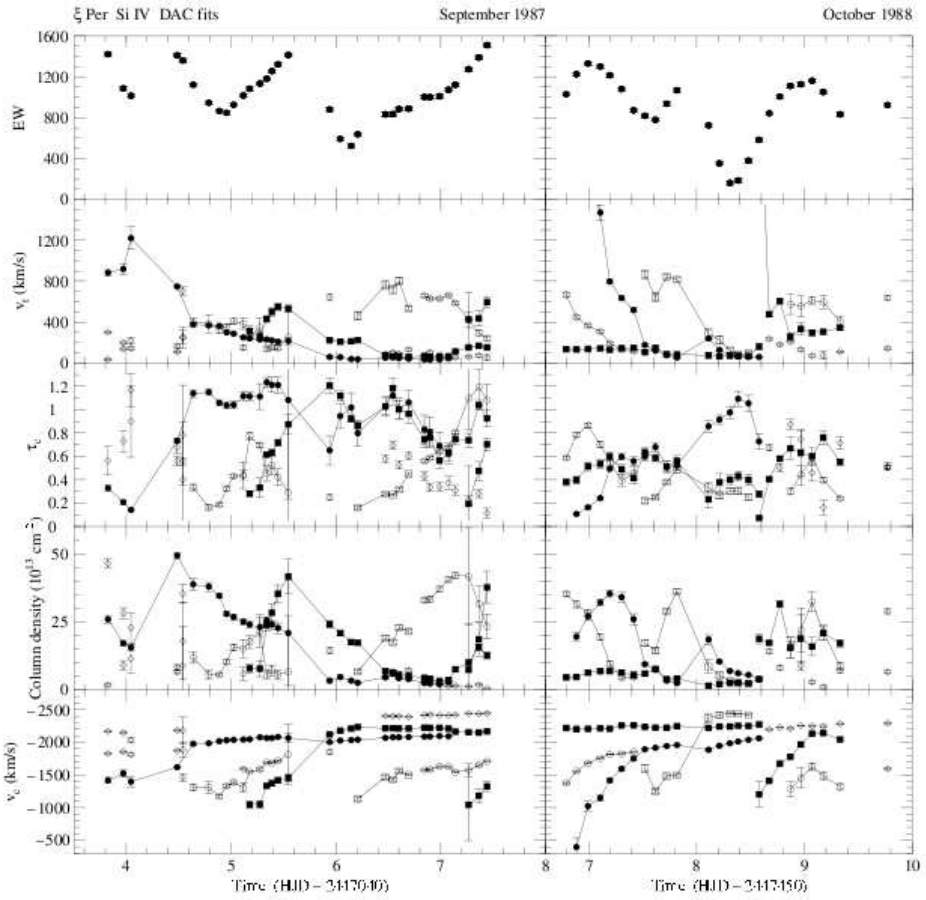

Figure 1.4: From top to bottom, plots showing the evolution of the equivalent width, width, central optical depth, column density and central velocity of DACs in the spectra of ξ Persei as a function of time. The panels on the left show the evolution of these properties during observations in September 1987, while panels on the right show data from October 1988 (Kaper et al. 1999; reproduced with permission © ESO).

While these hypotheses have been discussed in some detail, there has been no systematic study to try to evaluate them quantitatively and to constrain their parameter space. This is the main motivation for this thesis.

1.3 Goals

As mentioned in the previous section, DACs are inferred to be linked to large-scale azimuthal structures in the winds of massive stars. These structures can be modelled using photospheric perturbations, phenomenologically inferred to be "bright spots", albeit of unknown physical origin. This thesis aims to evaluate the magnetic hypothesis through three lines of inquiry:

- using the highest-quality observational data and the best analytical tools available to diagnose the presence of magnetic fields in the atmospheres of stars with well studied UV spectroscopic time-series exhibiting DACs (Chapter 4);
- constraining the properties of phenomenological bright spots based on both indirect and direct observational diagnostics (in the first case, evaluating what their inferred influence on the wind should be, and therefore how they impact wind-sensitive lines, as described in Chapter 6, and in the second case, assessing how brightness inhomogeneities on the surface should lead to total brightness variations as the star rotates, as well as variability in photospheric lines, as discussed in Chapter 7) and
- using the derived constraints to make quantitative, falsifiable predictions of the nature of the physical mechanism responsible for DACs (also in Chapters 6 and 7).

To accomplish this, a three-pronged approach is used: this thesis relies on observational, numerical and empirical methods to fully investigate this problem. However, given this large arsenal, additional background information will be needed to understand all the techniques used in the context of this project. A broader introduction to the theory of massive star winds and magnetic fields is presented in Chapter 2. Chapter 3 describes some of the concepts and practical aspects involved in the detection and measurement of stellar magnetic fields that are used in Chapter 4. Details about hydrodynamical modelling, radiative transfer and broadband optical photometry constitute the focus of Chapter 5 and will prove useful in understanding the techniques used in both Chapters 6 and 7. Finally, a summary of the work presented in this thesis and of the main conclusions that can be drawn from it, as well as a preview of future work to be conducted on this topic, is provided in Chapter 8.

	Large-scale dipolar magnetic fields	Small-scale magnetic fields (Magnetic spots)	Non-radial pulsations
Advantages	– Observed in massive stars [Wade et al., 2014] – Consistent with number of DACs per rotational period [Kaper et al., 1996]	– Possibly consistent with cyclical nature – Consistent with rotational modulation [Prinja, 1988]	– Observed in a few well-known DAC stars [de Jong et al., 1999] – Detectable using current instruments
Problems	– Magnetic stars show UV variations that are inconsistent with DACs (e.g., θ^1 Ori C, Stahl et al. 1996) – Only observed in small fraction of OB stars [Wade et al., 2014]	– Very difficult to detect [Kochukhov and Sudnik, 2013] and yet to be observed – Motivated by recent theoretical advances that are still poorly constrained [Cantiello and Braithwaite, 2011]	– Bright and dark regions not predicted to reproduce observed variability [Cranmer and Owocki, 1996] – Harder to reproduce recurrence periods [de Jong et al., 1999]

Table 1.1: Three main hypotheses concerning the physical origin of DACs as well as their advantages and problems.

Chapter 2

Mass loss and magnetic fields of massive stars

2.1 Massive star winds

As mentioned previously, an important driver of massive star evolution and of the interaction between massive stars and their environments is their winds. Typically, material in the stellar atmosphere is in hydrostatic equilibrium, meaning that the inwards gravitational force is compensated by the outwards thermal pressure. However, in a case where there is a net outward flux of material from the surface, as is the case in a stellar wind, there needs to be some additional force to overcome gravity at the surface of the star. There are a few physical phenomena which can account for this force.

In cool, low-mass stars like the Sun, the driving force leading to an outflow of particles is gas pressure, which is greatly enhanced in the sparse, super-heated (a few times 10^6 K) corona [Parker, 1958]. However, stars with spectral types earlier than F typically do not host this kind of structure in their upper atmospheres [Güdel, 2004]. Winds are often modelled as spherically symmetric, but that is not the case in general. For instance, in the Sun, the rotating magnetic field can lead to structures in

the wind known as *Parker spirals*, and small-scale structures called *helmet streamers* can develop over active regions (e.g., Kallenrode 2004). Other mechanisms such as acoustic waves in stars with convective envelopes [Landau and Lifshitz, 1959] and Alfvén waves [Parker, 1965] can help complement the picture of how the winds of low-mass stars are driven from their surfaces. Furthermore, while winds are taken to be outflows which are driven from the entire surface of stars (although not generally isotropic), localized outflows can also occur, such as those which feed decretion disks in Be stars. These stars have near-critical rotation and the additional force which allows them to shed mass from their equators is believed to be provided by pulsations [McSwain et al., 2008].

The most important mechanism to launch material from the photophere in high-mass stars, however, involves its interaction with the stars' intense UV radiation. The *Eddington limit* refers to the value of the stellar luminosity for which the radiative pressure is equal to the gravitational force. Thus, a star with a luminosity greater than the Eddington limit will have its outer layers pushed outwards via continuum-driven winds. Taking into account only electron scattering within a fully ionized hydrogen plasma, the obtained limit is [Eddington, 1926]:

$$L_{\rm Edd} = \frac{4\pi G M m_{\rm P} c}{\sigma_{\rm T}} \tag{2.1}$$

where G is the universal gravitational constant, M is the mass of the star, $m_{\rm P}$ is the proton mass, c is the speed of light and $\sigma_{\rm T}$ is the Thomson electron scattering cross-section.

For the large majority of massive stars (especially those on the main sequence),

their luminosity is well below the Eddington limit; therefore their luminosities are insufficient to lift material from the stellar surface via electron scattering. Hence, their winds cannot be continuum-driven. In evolved stars with expanded atmospheres, this deficit can be surmounted by the condensation of dust particles, which have high opacities and can lead to continuum-driven winds (e.g., Netzer and Elitzur 1993). However, for main sequence stars, another mechanism must be invoked. The *line-driving mechanism* (e.g., Castor et al. 1975) provides a framework to understand most massive star winds. Even though metallic ions are not very abundant in the atmospheres of massive stars, they possess a large number of electronic transitions with significant opacities. In a static atmosphere, photons with wavelengths corresponding to the energies of these transitions would have a short mean free path, as they would be quickly absorbed and the associated spectral lines would saturate, leading to a limited transfer of momentum to the outer layers of the star. However, in the wind, this is compensated by the fact that these lines are systematically Doppler-shifted as the ions are monotonically accelerated outwards, broadening the frequency range of absorption of the photons that can drive them. Indeed, as will be shown in the following section, the velocity profile of the outflowing winds is often approximately parametrized with a "β law":

$$v(r) \simeq v_0 + (v_\infty - v_0)\left(1 - \frac{R_*}{r}\right)^\beta \tag{2.2}$$

where $v(r)$ is the radial velocity of the wind at a certain distance r from the center of the star, v_0 is its speed at the star's surface (usually considered to be the sound speed), v_∞ (the *terminal velocity*) is its speed at a large distance from the star, R_* is the radius of the star (at the photosphere, i.e., defining the star's surface) and β is a

power-law index which depends on the stellar type. For the hottest stars (O stars), $\beta \sim 0.8$ [Pauldrach et al., 1986].

2.1.1 Line-driven winds and the CAK formalism

The equation of motion of material located at the surface of a star can be expressed using the Lagrangian derivative of the radial velocity (v)[1]:

$$a = \frac{\mathrm{D}v}{\mathrm{D}t} = \frac{\partial v}{\partial t} + v\frac{\partial v}{\partial r} \tag{2.3}$$

where a is the radial acceleration, t is time and r is the distance from the center of the star. Assuming a steady-state configuration for the wind, the first term on the right-hand side is null. Also, spherical symmetry allows us to replace the partial derivative by a total derivative. Using Newton's second law, we obtain:

$$a = v\frac{\mathrm{d}v}{\mathrm{d}r} = -\frac{\mathrm{d}P/\mathrm{d}r}{\rho} - \frac{GM}{r^2} + g_{\mathrm{rad}} \tag{2.4}$$

where the first term on the right-hand side is the radial derivative of pressure (P) divided by density (ρ), or in other words, the thermal gas pressure term; the second term is the gravitational force (where G is the universal gravitational constant and M is the mass of the star); the last term corresponds to the (outward) acceleration provided by radiation. In massive stars, the first term is negligible because the temperature at their surfaces (typically tens of kK) is not sufficient to create a large gas pressure. The last term typically falls off as $1/r^2$, like gravity, and can be expressed as x_{rad}/r^2. Therefore the Eq. 2.4 can be rewritten:

[1]The derivation presented in this section is partly inspired by Owocki [2013].

$$\frac{1}{2}\frac{\mathrm{d}(v^2)}{\mathrm{d}r} = \frac{x_{\mathrm{rad}} - GM}{r^2}. \tag{2.5}$$

Integrating this equation from the stellar surface ($r = R_*$) to a given radius, we obtain the following velocity profile:

$$v(r) = \sqrt{2(x_{\mathrm{rad}} - GM)(1 - R_*/r)} \tag{2.6}$$

Noticing that in the limit $r \to \infty$, we have $v \to v_\infty = \sqrt{2(x_{\mathrm{rad}} - GM)}$, we can write:

$$v(r) = v_\infty \left(1 - \frac{R_*}{r}\right)^{1/2} \tag{2.7}$$

which is the β law using $\beta = 0.5$. As mentioned in the previous section, O stars typically have $\beta = 0.8$, corresponding to a less steep velocity profile. This profile is illustrated in the top panel of Fig. 2.1. Using the mass continuity equation, it is also possible to determine the density profile of the wind:

$$\rho(r) = \frac{\dot{M}}{4\pi r^2 v(r)} \tag{2.8}$$

where $\dot{M}$ corresponds to the mass-loss rate, which will be calculated shortly.

That density profile is shown in the bottom panel of Fig. 2.1. Both profiles in that figure correspond to a spherically-symmetric ideal wind.

However, while this derivation provides insight into the behaviour of the wind, it does not shed light on the nature of g_{rad}. As explained earlier, electron scattering does not provide sufficient force because massive stars typically have luminosities well below the Eddington limit. Instead, the driving mechanism occurs due to line scattering: UV photons are scattered by metallic ions in the wind. Despite the

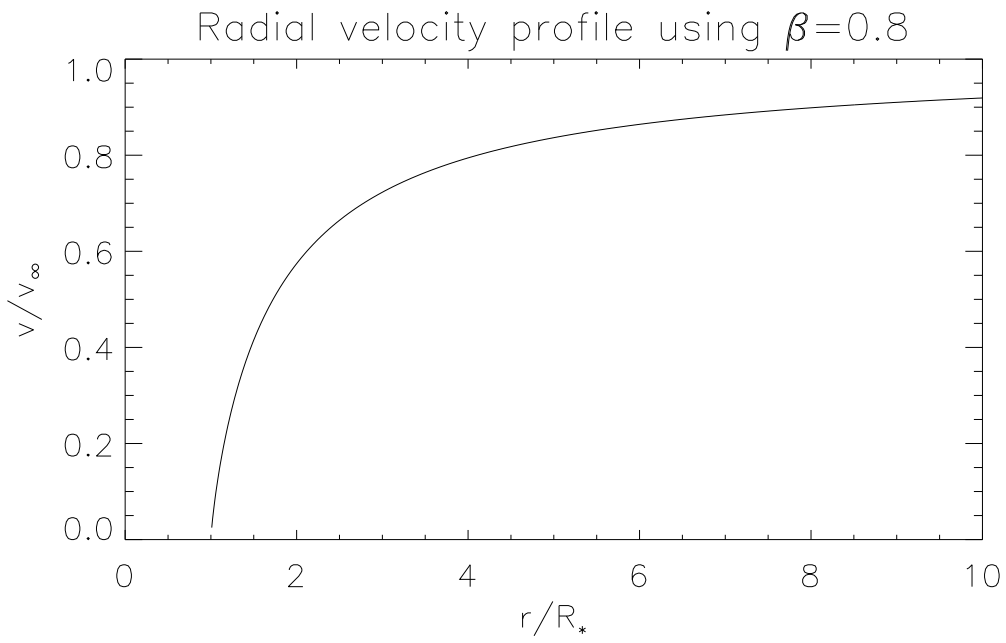

(a) Radial velocity profile.

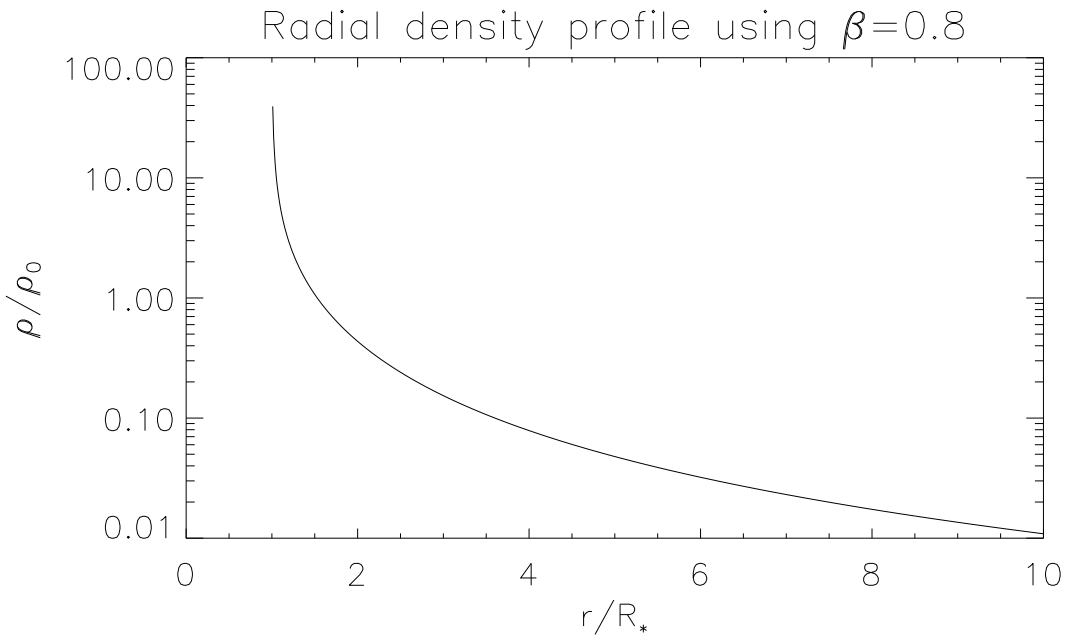

(b) Radial density profile.

Figure 2.1: Computed velocity and density profiles for line-driven spherically-symmetric winds using $\beta = 0.8$; the velocity is scaled with respect to the terminal velocity, while the density is scaled with respect to some, characteristic density. Both of these scaling factors depend on the physical parameters of the star.

small interaction cross-sections involved as well as the discrete nature of the binding energies within these ions, the resonant nature of the interaction, and the Doppler shift induced by the outward-accelerating wind compensate and allow this mechanism to drive dense, supersonic winds in massive stars.

The formalism used to express the cumulative force due the scattering of an ensemble of lines was developed in large part by Sobolev [1960] and Castor et al. [1975] (hereafter referred to as "CAK"), but its full derivation is considered to fall outside the scope of this short review. Instead, we will focus on the most useful results.

Firstly, the *Sobolev approximation* [Sobolev, 1960] allows us to compute the total optical depth of radiation propagating radially through the resonance of a single line in terms of local variables rather than having to perform the entire integral along the path, providing that the velocity gradient is steep enough for that resonance to be localized:

$$\tau_s = \frac{\rho q \kappa_e c}{\mathrm{d}v/\mathrm{d}r} \tag{2.9}$$

where τ_s is the Sobolev optical depth, q corresponds to the line strength, κ_e is the Thomson scattering opacity and c is the speed of light.

Then, the CAK theory computes the collective line force. Given a distribution of line strengths q which is a power law of index α, the line-driving force for a point star can be written as:

$$g_{\mathrm{CAK}} = \frac{1}{1-\alpha} \frac{\kappa_e L_* \bar{Q}}{4\pi r^2 c} \left(\frac{\mathrm{d}v/\mathrm{d}r}{\rho c \bar{Q} \kappa_e} \right)^{\alpha} \tag{2.10}$$

where L_* is the stellar luminosity and $\bar{Q}$ is a cumulative line-strength parametrization

(developed by Gayley 1995 and typically equal to roughly 2000 in massive stars). If we denote the ratio of the radiative acceleration to the gravitational acceleration $\Gamma \equiv g_{\rm CAK} r^2/GM$, we then obtain the following maximum mass-loss rate:

$$\dot{M}_{\rm CAK} = \frac{L}{c^2}\frac{\alpha}{1-\alpha}\left[\frac{\bar{Q}\Gamma}{1-\Gamma}\right]^{(1-\alpha)/\alpha}. \tag{2.11}$$

The terminal velocity is:

$$v_\infty = v_{\rm esc}\sqrt{\frac{\alpha}{1-\alpha}} = \sqrt{\frac{2GM\alpha}{R_*(1-\alpha)}} \tag{2.12}$$

where $v_{\rm esc}$ is the escape velocity at the surface of the star, defined as:

$$v_{\rm esc} \equiv \sqrt{\frac{2GM}{R_*}}. \tag{2.13}$$

This derivation holds for a point source (i.e., if the star consisted of a single point located at its center), but finite disk correction factors can be computed to take into account the finite extent of the stellar disk. Line-driven winds are also inherently subject to instabilities. The *line deshadowing instability* (LDI; e.g., Owocki and Rybicki 1984, 1985) can introduce important structures in the radial velocity profile (forming dense clumps in the wind which shock and produce X rays, Feldmeier et al. 1997) which, when modelling wind-sensitive lines, can be treated using a velocity dispersion parameter analogous to the microturbulent velocity.

2.2 Massive star magnetism

As mentioned earlier, stars are composed of plasmas, and these plasmas are dynamic and move on global (e.g., rotation) as well as local (e.g., convection) scales. This

naturally gives rise to magnetic fields. Since magnetic fields have been hypothesized as being a possible cause of DACs, it is important to understand the possible origins of these fields in OB stars.

2.2.1 Basic dynamo theory

The evolution of the magnetic field **B** is given by the magnetohydrodynamic (MHD) induction equation:

$$\frac{\partial \mathbf{B}}{\partial t} = \nabla \times (\mathbf{u} \times \mathbf{B} - \eta \nabla \times \mathbf{B}) \tag{2.14}$$

where **u** is velocity and η is the magnetic diffusivity of the medium[2]. From this equation, we can separate two idealized cases. First, if the second term within the parentheses on the right hand side dominates, then Ohmic dissipation slowly decays the field. Otherwise, if the first term is much larger, in the ideal MHD limit, the flow can help amplify the magnetic field.

Resistive decay

First, we consider a case where the Ohmic dissipation term dominates over the inductive term. This would correspond to a situation where there is an initial magnetic field present, but no inductive contribution to amplify it, so that it is left to decay over time. The typical timescale τ associated to the decay of the magnetic field is called the *magnetic diffusion time*. In order to estimate its value, we must first perform a dimensional analysis of the MHD induction equation. Given a typical length

[2] A typical value of this parameter on the surface of a main-sequence B0 star is roughly 2.5×10^6 cm^2/s (as derived from the electrical conductivity values provided by Kopecký and Kotrč 1973).

scale l which characterizes the distance on which the field (and flow) vary, we obtain (replacing the time derivatives by $1/\tau$ and spatial derivatives by $1/l$):

$$\frac{B}{\tau} = \frac{u_0 B}{l} + \frac{\eta B}{l^2} \tag{2.15}$$

where u_0 and B are considered to be typical (average) values of the flow velocity and of the magnetic field strength, respectively. If we neglect the first term (provided that on average, the velocities cancel each other) and solve for τ, we get

$$\tau = \frac{l^2}{\eta} \tag{2.16}$$

This is a first-order estimate of the Ohmic dissipation timescale. A more in-depth treatment consists in separating the magnetic field into poloidal and toroidal components. These components can then be expressed in terms of spherical harmonics, and solving for the most simple case (the fundamental mode of a dipolar poloidal field, [Mestel and Weiss, 1974]), we get:

$$\tau = \frac{R^2}{\pi^2 \eta} \tag{2.17}$$

where R is the radius of the star. This extreme case will be discussed in more detail in the context of fossil fields (Sect. 2.2.2), but it should be kept in mind that Ohmic dissipation is an issue for all stars and that therefore, dynamos must compensate for this effect.

Amplification of magnetic fields

One way of amplifying magnetic fields is by stretching magnetic field lines. Indeed, in the ideal MHD limit (when the diffusive term in the MHD induction equation is negligible), we can derive the following expression for the evolution of the field within a fluid element:

$$\frac{\partial \mathbf{B}}{\partial t} + (\mathbf{u} \cdot \nabla)\mathbf{B} = \frac{\mathrm{D}\mathbf{B}}{\mathrm{D}t} = \mathbf{B} \cdot \nabla \mathbf{u}. \tag{2.18}$$

Therefore, the field lines, which, according to *Alfvén's theorem* [Alfvén, 1942], are frozen within a given fluid element in this ideal MHD limit, will become stronger if that element is stretched (right hand side term). This effect is called *shearing* and is an important means of magnifying magnetic fields.

One intuitive illustration, taken from Charbonneau [2010], is to consider a flux tube shaped as a cylinder. If the cylinder is stretched in the direction of the field lines, its radius will shrink in proportion (due to conservation of mass). On the other hand, conservation of flux requires that the field become stronger to compensate. The increase in field strength will be proportional to the stretch. An important application of this shearing amplification is the so-called Ω effect: the production of a toroidal field under the influence of differential stellar rotation.

Apart from differential rotation, another type of flow typically involved in dynamos stems from the turbulent motions found within convective zones. However, these turbulent motions are local, with scales typically very small compared to the scale of the global magnetic field. The basic idea is that the electromotive force provided locally by these turbulent motions can amount to large-scale magnetic field generation. The induction generated by the small-scale turbulent motions can feed

the magnetic field, transforming toroidal fields into poloidal fields and vice-versa. This effect (called the α *effect*) can be calculated using mean-field electrodynamics, but its derivation is outside the scope of this thesis.

Both effects can occur simultaneously and mutually support each other to form a full dynamo. Different families of dynamos are represented by the $\alpha\Omega$ effect and by the α^2 effect. In the first case, differential rotation (shearing) transforms poloidal field into toroidal field, and the α effect provides the inverse transformation. In the second case, the α effect produces both transformations.

2.2.2 Fossil field hypothesis

While most main-sequence cool (F, G, K) stars show evidence for magnetic activity, detections of magnetic fields in massive stars are much less frequent. Current statistics indicate that the fraction of known OB stars with magnetic fields is of the order of 7% [Wade et al., 2014]. The most broadly accepted origin for magnetic fields in massive stars, both theoretically and observationally, is the *fossil field hypothesis*. It assumes that the magnetic fields that we observe today are remnants of fields generated earlier in the star's formation or evolution, e.g., initial seed magnetic fields present in the star-forming region, fields generated by dynamos in the pre-main sequence (PMS) phase, or created during mergers. These fields are expected to evolve and decay over a very long timescale which is typically much larger than the lifetime of the star on the main sequence. Indeed, as seen in Sect. 2.2.1, fields decay resistively, but over timescales which can be quite large. For a typical A0 star, the decay time is of order of the age of the universe [Mestel and Weiss, 1974]. Another important aspect to take into consideration is that the typical scale of length from Eq. 2.16 is equal to the

typical length of polarity reversal, which varies depending on the nature of the field, the order of the multipole and the mode. This means that different components of the magnetic field decay over different timescales. Higher order multipoles decay faster, implying that the longest lasting fields are dipolar. Even in that case, poloidal fields tend to remain the longest since a toroidal multipole of order n decays on the same timescale as a poloidal multipole of order $(n + 1)$ [Charbonneau, 2010]. Finally, as the stars expand during their evolution, the magnetic field at the surface gets weaker, not only because of Ohmic dissipation, but also due to the conservation of magnetic flux.

Observationally, the fossil field hypothesis has been constrained by the work of the *Magnetism in Massive Stars* (MiMeS) Collaboration [Wade et al., 2016]. Through a Large Program (LP) at the Canada-France-Hawaii Telescope (CFHT) on the ES-PaDOnS instrument, MiMeS obtained 640 hours of observing time, divided in two parts: a Target Component (TC), investigating some known magnetic stars as well as possible candidates presenting interesting peculiarities (e.g. X-ray emission) and a Survey Component (SC) containing a large number of O, B and A stars. This SC establishes a statistical basis for magnetism in massive stars.

On the whole, 65 massive stars were confirmed to be magnetic out of a sample of roughly 550 stars, effectively doubling the number of known magnetic massive stars. The interaction of their fields with their winds has been categorized [Petit et al., 2013], providing a much better understanding of massive star magnetospheres. Perhaps the most important result of this investigation lies in the fact that most detected magnetic fields of massive stars are essentially dipolar poloidal fields [Wade et al., 2014], and are stable over long timescales (e.g., decades in the case of σ Ori E, first detected

by Landstreet and Borra 1978). These characteristics place important constraints on the formation mechanism of the fields, and help determine whether they are of fossil origin, or are generated by contemporary dynamos.

2.2.3 Hypothesized dynamo mechanisms in OB stars

The field of stellar magnetism was first developed in the context of the Sun's magnetic field, which was observed to be very strong within the spots on its surface [Hale, 1908]. While today, after decades of research, the magnetism of low-mass stars is reasonably well understood, the same cannot be said of their hefty cousins. The reason for that discrepancy comes from the convective nature of most solar (and solar-like) dynamo models. Indeed, as seen in the previous section, one of the drivers of the dynamo is the cumulative effect of small-scale turbulent convective flows. However, convection does not occur similarly in massive stars and in low-mass stars. While cooler stars have extended convective envelopes surrounding a radiative core, massive stars have convective cores surrounded by radiative envelopes. Between these two extremes, intermediate-mass stars can be almost devoid of convection (especially around spectral type A). Therefore, dynamos in massive stars present a very different picture than dynamos in cool stars. Here is a short summary of the various scenarios which have been proposed to explain massive star magnetism using contemporary dynamos.

Core dynamos

The cores of the most massive stars are host to convection; therefore, they can be subject to the α effect, as discussed previously. Using a similar formalism to that of their less massive counterparts, a core dynamo model can be devised. The main

problem encountered, however, has to do with the surface magnetic field. Indeed, magnetic fields generated from core dynamos tend to be limited to the core and its vicinity. Adding in differential rotation, it is possible to transform some of the poloidal field of the core to toroidal field within the neighbouring layers in the radiative envelope, but simulations show (e.g., Brun et al. 2005) that the field still remains constrained to the inner region of the star (see Fig. 2.2).

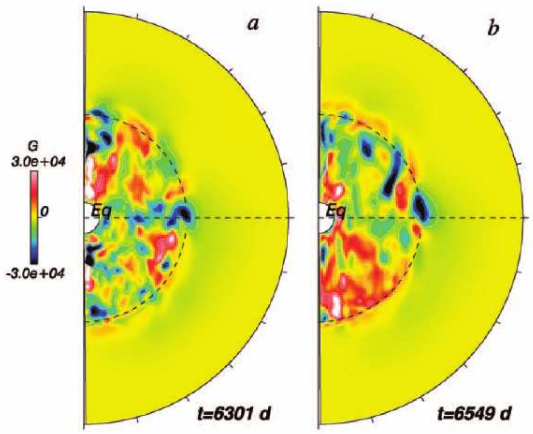

Figure 2.2: Simulations of a core dynamo with shearing at the interface between the convective core and the radiative envelope (from Brun et al. 2005). The colours represent the intensity and direction of the toroidal field. © AAS. Reproduced with permission.

Transport of the magnetic field to the surface

One solution proposed to avoid the magnetic field being trapped in the core is the buoyant rise of rings of toroidal field from the interface between the core and the envelope to the surface of the star [MacGregor and Cassinelli, 2003].

The typical timescales obtained in this study are a few orders of magnitude smaller than the lifetime of the stars on the main sequence. However, certain important effects were neglected, especially meridional circulation, which may cause the toroidal field

rings to become unstable. Nevertheless, this scenario provides a potential mechanism for the transport of the magnetic field to the photosphere.

Differential rotation and shear dynamos in the radiative envelope

A competing theory is that turbulence within the radiative envelope could produce the magnetic field instead [Spruit, 2002]. In this case, the dynamo could be provided by differential rotation within a stably stratified radiative envelope, combined with instabilities in a toroidal magnetic field, which replace convection. The proposed mechanism here is the Tayler instability [Tayler, 1973].

The main problem with dynamo scenarios in massive stars is that none of them leads to the type of fields that are actually observed in these stars, i.e., large-scale dipolar fields. Thus, we can unambiguously make the case that the fossil field scenario is the hypothesis that agrees most consistently with observations when it comes to understanding the properties of detected magnetic fields in massive stars [Neiner et al., 2015]. An important remaining challenge is to determine where these fossil fields come from and why they are not ubiquitous.

2.2.4 Sub-surface convection and magnetic spots

Cantiello and Braithwaite [2011] have proposed yet another mechanism to produce magnetic fields at the surface of massive stars. Unlike the previous mechanisms, this one does not aim to reproduce or explain observations, but arises as a possible consequence of model predictions. Iron-group elements have an enhanced opacity at a temperature of about 150 kK, thus giving rise to a thin, yet important sub-surface convection layer (as evidenced by, e.g., Cantiello et al. 2009). The turbulent motions

within the *iron convection zone* (FeCZ) could provide an efficient α^2 or $\alpha\Omega$ dynamo. Magnetic flux tubes could rise buoyantly to the surface more easily and rapidly than in the case of core dynamos, since the FeCZ is close to the photosphere. However, this would be a small-scale dynamo, so the field would manifest itself rather in the form of magnetic spots, analogous to sunspots. Therefore, the surface of a massive star could be covered with magnetic spots, thus presenting a topologically complex field which is hard to detect [Kochukhov and Sudnik, 2013]. Unfortunately, Cantiello and Braithwaite [2011] do not offer any strong constraints on the size or geometry of the spots. The strength of the field in the spots could vary from a couple tens of gauss to a couple hundreds for stars with $M_* > 20M_\odot$. Such fields have yet to be observed on the surface of massive stars.

2.3 Interacting magnetic fields and winds

Factoring in the considerations of Sect. 2.1 in the case of magnetic massive stars, the interaction between the field and the wind leads to important consequences. Given the fact that the atmosphere of a star is made up of plasma, i.e. charged matter, if the field is strong enough, it puts an additional constraint on the outflowing particles, channeling, and possibly restricting the flow, confining it to the vicinity of the star. In practice, the influence of the magnetic field on the wind of a star can be expressed through the *magnetic confinement parameter* η_* (as defined by ud-Doula and Owocki 2002):

$$\eta_* = \frac{{B_{\rm eq}}^2 {R_*}^2}{\dot{M} v_\infty} \tag{2.19}$$

where $B_{\rm eq}$ is the strength of the dipolar magnetic field at the stellar magnetic equator,

R_* is the radius of the star, $\dot{M}$ is its mass-loss rate and v_∞ is the terminal velocity that star's wind would have if the star were non-magnetic. This parameter corresponds, basically, to the ratio of the magnetic field energy density and the wind kinetic energy density at the star's surface.

A wind is considered to be magnetically confined when $\eta_* \gtrsim 1$, but the magnetic field can still produce wind perturbations for values as low as 0.1 [ud-Doula and Owocki, 2002]. Therefore, winds of stars with $\eta_* < 0.1$ will be considered to be essentially unaffected by magnetism, while stars with $0.1 < \eta_* < 1$ correspond to an intermediate regime where it is difficult to evaluate the exact effect of the magnetic field on the wind (but this effect remains potentially modest). Stars with $\eta_* > 1$ have winds which are strongly confined by their magnetic field, forming a *magnetosphere*. When it is strongly confined, the wind can fall back onto the star, and the overall mass-loss rate is therefore reduced.

Rotation also plays a role in determining what happens to this magnetosphere by providing an outward centrifugal support. Therefore, the magnetospheres of magnetic massive stars can be categorized following the relative importance of each of these processes. Petit et al. [2013] provide an extensive review of these effects.

Another mechanism whereby surface magnetic fields might affect winds indirectly consists of brightness inhomogeneities in the photosphere. Indeed, the fields might influence the structure of the atmosphere, leading to regions of lower density which appear hotter (and therefore brighter) and locally drive an enhanced outflow. This particular mechanism is further quantified in Chapter 4.

Chapter 3

Measurement of stellar magnetic fields

In the previous chapter, we have reviewed various ways by which magnetic fields can be generated and sustained, but we have yet to describe the techniques required in order to determine observationally whether they exist, and if so, to characterize them.

This chapter provides basic background information needed to better understand some of the methods used in Chapter 4. We will focus both on the theoretical underpinnings and the practical implementation and challenges related to these methods.

3.1 Zeeman effect

The Zeeman effect [Zeeman, 1897] refers to the splitting of spectral lines in the presence of a magnetic field. An external magnetic field lifts the degeneracy of certain electronic energy levels, thus giving way to transitions with slightly different energies, causing the splitting of the associated spectral line. This is a very important tool, since there are not many ways to diagnose the presence of a magnetic field in an astronomical context, e.g., on the surface of a star. The Zeeman effect provides one of the most direct measurements of such fields, not only enabling their detection, but also their measurement.

In this section, we will review the quantum mechanical basis of the Zeeman effect and summarily derive its consequences and applications.

3.1.1 Basic quantum mechanical model of the Zeeman effect

To begin, a basic quantum mechanical model has to be derived in order to determine how the magnetic field affects the atom. The treatment presented here is partly inspired by two quantum mechanics textbooks, Rae [2002] and Schwabl [2007]. The interaction with the external magnetic field will be noted as an additional term in the atom's Hamiltonian:

$$H = H_0 + V_m \tag{3.1}$$

where

$$V_m = -\mu \cdot \mathbf{B} \tag{3.2}$$

with V_m corresponding to the interaction energy in an external magnetic field $\mathbf{B}$. μ is the magnetic moment of the atom and is equal to the sum of the magnetic moments of the nucleus and of the electron(s). However, the first term (nuclear) of Eq. 3.1 is negligible in comparison to the other, so only the second one is considered.

Single electron atoms

An electron has the following value of magnetic moment, composed of the sum of two components (one for the orbital angular momentum and the other one for the spin):

$$\mu = -\frac{e}{2m_e}(\mathbf{l} + 2\mathbf{s}) \tag{3.3}$$

where m_e is the mass of the electron, and $\mathbf{l}$ and $\mathbf{s}$ are respectively its orbital and spin angular momenta.[1] The factor of 2 that multiplies $\mathbf{s}$ is given by relativistic quantum theory and is actually not exactly 2, but has a value extremely close to 2. Therefore, for means of simplicity, we will adopt the value of 2.

Thus, combining Eq. 3.2 and Eq. 3.3, we obtain:

$$V_m = \frac{e}{2m_e}\mathbf{B} \cdot (\mathbf{l} + 2\mathbf{s}) \tag{3.4}$$

and if we consider $\mathbf{B}$ to be pointing in the z-direction, without losing any generality, then we can write

$$V_m = \frac{eB}{2m_e}(l_z + 2s_z) = \hbar\omega_L(m_l + 2m_s) \tag{3.5}$$

where $m_l = l_z/\hbar$ is the *magnetic quantum number*, $m_s = s_z/\hbar$ is the *spin projection quantum number* and $\omega_L = \frac{eB}{2m_e}$ is called the *Larmor frequency*.

Multi-electron atoms

The single electron case can now be generalized to the multi-electron case. The interaction term from Eq. 3.5 now becomes a sum over all the electrons:

[1] It should be noted that in this case, the lower case is used to emphasize that these are the momenta of a single electron. This notation will be used throughout this section and there should be no confusion between the orbital and spin angular momentum vectors ($\mathbf{l}$ and $\mathbf{s}$) and the corresponding scalar quantum numbers l and s.

$$V_m = \frac{eB}{2m_e} \sum_i (l_{z,i} + 2s_{z,i}) = \omega_L (L_z + 2S_z) \tag{3.6}$$

where the uppercase L and S denote the total orbital and spin angular momenta of the atom.

3.1.2 Assumptions commonly invoked

Different assumptions can be made depending on which interactions are dominant within the atom. These assumptions usually simplify calculations. One particular set of assumptions that is used in the context of the Zeeman effect is linked to the spin-orbit coupling. Indeed, within an atom, the orbital angular momentum of the electrons can interact with their spin angular momentum, thus affecting certain conservation properties. However, these assumptions only hold if the electrons do not interact more strongly with an external magnetic field. The following derivations are partly inspired by Spaldin [2003].

LS coupling

In light atoms, the interactions between the individual spin angular momenta of the electrons and the interactions between their individual orbital angular momenta are much stronger than the spin-orbit coupling. Therefore, it is possible to define total orbital and spin angular momenta by independently adding up the spin and orbital momenta of the electrons:

$$\mathbf{L} = \sum_i l_i \tag{3.7}$$

$$\mathbf{S} = \sum_i s_i \tag{3.8}$$

It is then these total spin and orbital angular momenta which interact together, adding up to give the total angular momentum of the atom:

$$\mathbf{J} = \mathbf{L} + \mathbf{S} \tag{3.9}$$

jj coupling

In the case of more massive atoms, with many electrons, the orbital and spin angular momenta tend to interact within individual electrons, conserving the total angular momentum of each electron separately. Therefore, it is no longer appropriate in such cases to refer to the total angular momentum of the atom as the sum of the total orbital and spin angular momenta of the electrons, but rather as the sum of the total angular momenta of all its electrons:

$$\mathbf{J} = \sum_i j_i = \sum_i (l_i + s_i) \tag{3.10}$$

3.1.3 Energy level splitting

Using the LS coupling assumption, we can derive the energy level splitting brought about by the Zeeman effect. **L** and **S** are not individually conserved, so using the projection theorem, we can evaluate their expectation values:

$$< \mathbf{S} >= \frac{< \mathbf{S} \cdot \mathbf{J} >}{J^2} \mathbf{J} \tag{3.11}$$

$$< \mathbf{L} >= \frac{< \mathbf{L} \cdot \mathbf{J} >}{J^2}\mathbf{J} \tag{3.12}$$

Using LS coupling and the new quantum number $m_j = J_z/\hbar$, and including Eq. 3.4, we obtain:

$$< V_M >= \hbar\omega_L m_j \left(\frac{3}{2} + \frac{s(s+1) - l(l+1)}{2j(j+1)}\right) \tag{3.13}$$

The term in parentheses is called the *Landé g-factor* (g_L).

Finally, when the total spin of the atom is $s = 0$, Eq. 3.6 yields the following expression:

$$V_m = \hbar\omega_L m_l g_L \tag{3.14}$$

In such a case, it is obvious that the corresponding energy level will be split into $(2l + 1)$ components (since $-l \leq m_l \leq l$). This will be the basis for the so-called *normal* Zeeman effect.

However, this is a very particular case, and in no way "normal". When $s \neq 0$ (for instance in the case where $s = 1/2$), instead of considering m_l, we now consider m_j (under the LS coupling assumption), which can take an even $(2l + 2)$ number of half-integer values between $-(l + 1/2)$ and $l + 1/2$.

3.1.4 Transition diagrams, Zeeman patterns, π vs. σ components

As mentioned previously, the normal Zeeman effect occurs within an atom with a total spin of 0. In such a case, each level is split into $(2l + 1)$ levels. However, some selection rules apply in order to determine which transitions are possible. The

variation of m_l is particularly important in that regard. Indeed, transitions must occur with $\Delta m_l = 0, \pm 1$ (for a dipolar magnetic moment). Since all the levels are equally spaced and centered around one given initial level of energy, the energy of the transition will only depend on Δm_l, thus producing a triplet.

However, as mentioned above, this *normal* effect is actually a very special case and most often does not represent the line splitting correctly. This is because the total spin is not always 0. Then, we must consider the *anomalous* Zeeman effect. Both the normal and the anomalous Zeeman effect are illustrated in Fig. 3.1.

All transitions do not occur with the same intensity. The normalized strength of a transition; i.e.:

$$S_{\alpha,m'} = \frac{\tilde{S}_{\alpha,m'}}{\sum_{m'} \tilde{S}_{\alpha,m'}}, \tag{3.15}$$

where $\alpha = m_i - m_f = -\Delta m$, is computed from the unnormalized transition strengths, given by:

$$\begin{aligned} \tilde{S}_{\alpha,m'} &= \frac{1}{2}(j' - m' + 1)(j' - m' + 2) \quad \text{for } \alpha = -1, \\ &= (j' + 1)^2 - m'^2 \qquad\qquad\qquad \text{for } \alpha = 0, \\ &= \frac{1}{2}(j' + m' + 1)(j' + m' + 2) \quad \text{for } \alpha = +1. \end{aligned} \tag{3.16}$$

for a de-excitation transition [del Toro Iniesta, 2003]. In Eq. 3.16, j' and m' are the quantum numbers of the final level of the transition.

Depending on the variation of the m_l (or m_j) quantum number, the polarization of the spectral line can be either parallel (it is then noted π) or perpendicular (noted

σ) to the field. By definition, $\Delta m_l = 0$ gives a π component whereas $\Delta m_l = \pm 1$ gives the σ components.

As for the value of the displacement of a spectral line for a given transition, one can use the following equations to compute it in *Lorentz units*[2]:

$$\begin{aligned} \frac{\Delta\lambda_{\rm B}}{\lambda_{\rm B}} &= m'(g'_L - g_L) + g_L \quad \text{for } \alpha = -1, \\ &= m'(g'_L - g_L) \qquad\quad \text{for } \alpha = 0, \\ &= m'(g'_L - g_L) - g_L \quad \text{for } \alpha = +1. \end{aligned} \tag{3.17}$$

where g_L and g'_L are respectively the upper and lower Landé factors.

Finally, all this information can be summarized in what is called a Zeeman pattern. Different transitions are shown with their displacements, their intensities and their polarization. To distinguish them, π components are shown as positive and σ components appear as negative. An example of Zeeman patterns, together with the transitions that created them, is shown in Fig. 3.1; the same Zeeman patterns are presented in greater detail in Fig. 3.2.

3.2 Zeeman signatures in polarized spectra

While the splitting patterns presented in the previous section can cause a broadening of spectral lines, the magnetic fields typically detected on the surfaces of stars are too weak to produce a detectable broadening (or at the very least, a broadening which is distinguishable from other sources of broadening, which will be discussed in

[2]The Lorentz unit $\lambda_{\rm B}$ corresponds to the splitting of a normal Zeeman triplet of Landé factor unity, or for a transition occurring at a wavelength of λ_0, $\lambda_{\rm B} = \lambda_0^2 eB/4\pi m_e c^2$.

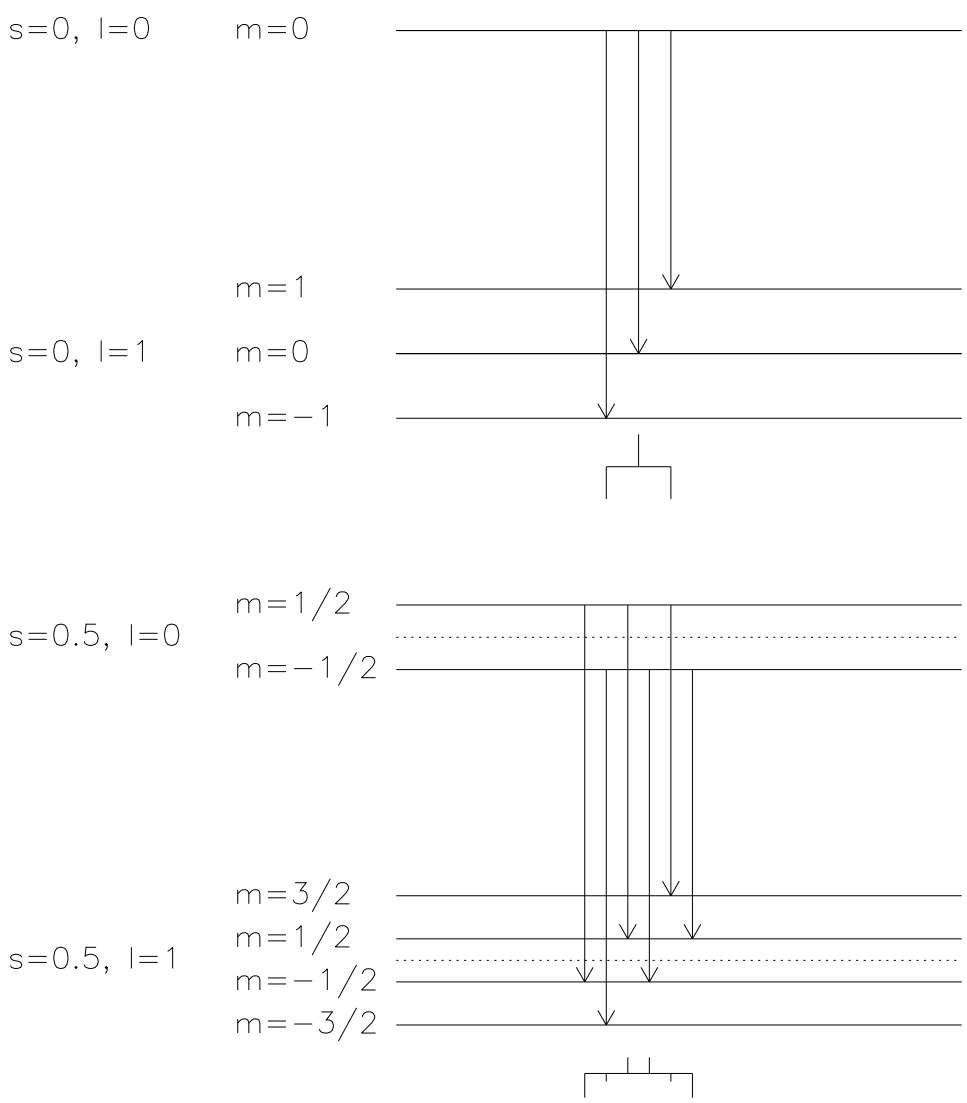

Figure 3.1: Transition diagrams for both the normal (top) and anomalous (bottom) Zeeman effect. The transitions shown all follow the selection rule ($\Delta m_l = 0, \pm 1$). The corresponding Zeeman patterns are shown underneath, with the π components appearing above the horizontal lines and the σ components below.

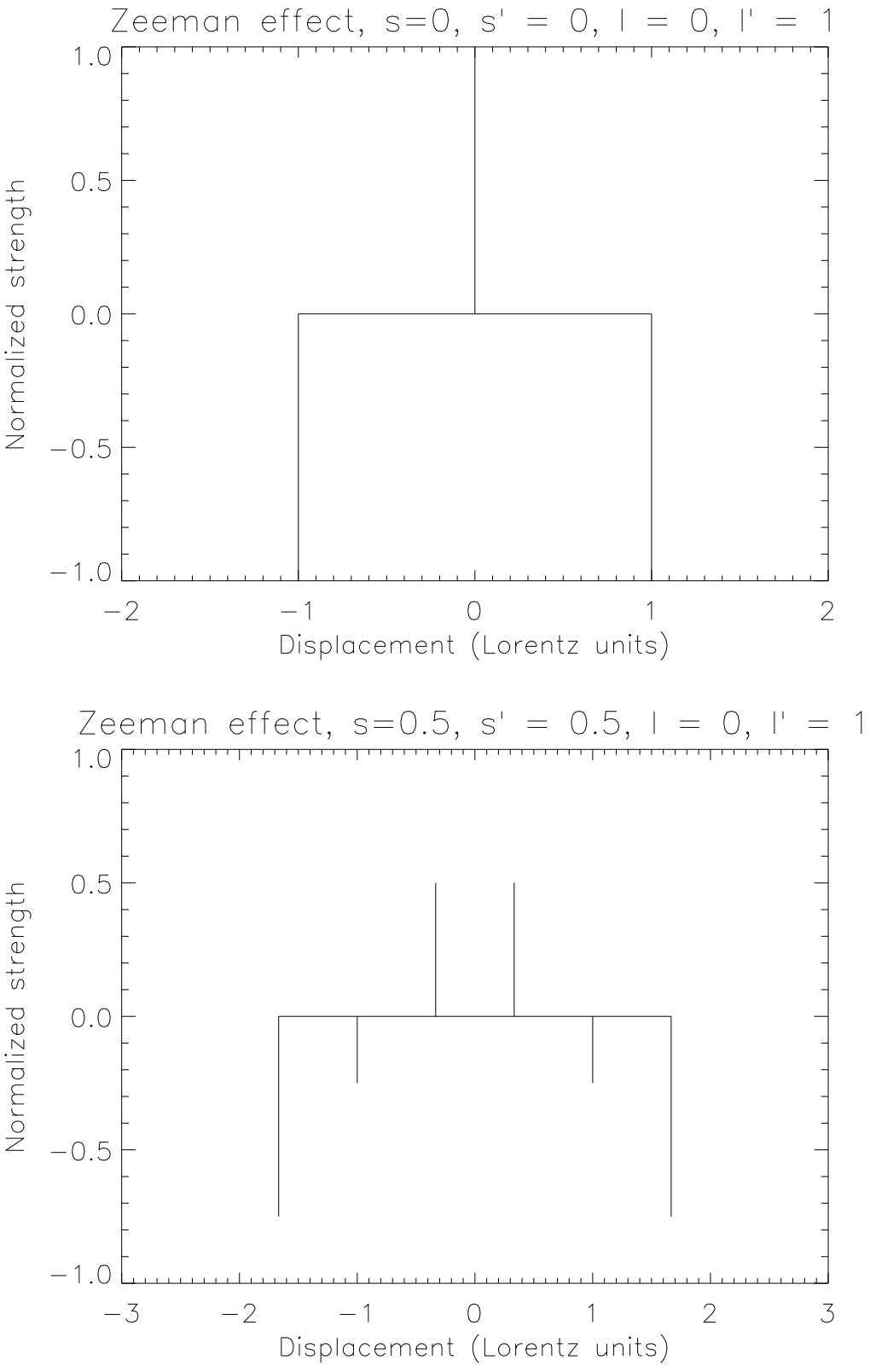

Figure 3.2: Zeeman patterns associated to the transitions shown in Fig. 3.1.

Sect. 5.3. Therefore, we need additional information to detect and measure this effect. Fortunately, the σ components of the Zeeman multiplets are circularly polarized, therefore magnetic fields can be diagnosed using spectropolarimetry. We start by briefly reviewing the quantities which will be measured.

The Stokes parameters are frequently used to describe the polarization state of an ensemble of electromagnetic waves. If we choose z to be the direction of propagation of an ideal, monochromatic wave, then the electric field $\mathbf{E}$ varies in the xy-plane and we can write the *polarization tensor* as:

$$\mathbf{C} \equiv \begin{pmatrix} E_x E_x^* & E_x E_y^* \\ E_y E_x^* & E_y E_y^* \end{pmatrix} \tag{3.18}$$

where each of the tensor elements is formed by multiplying a component of the electric field by its complex conjugate (for the diagonal elements) or by the complex conjugate of the other component.

Then, the Stokes parameters can be written as follows (e.g., [del Toro Iniesta, 2003]):

$$I \equiv \kappa(C_{11} + C_{22}) \tag{3.19}$$

$$Q \equiv \kappa(C_{11} - C_{22}) \tag{3.20}$$

$$U \equiv \kappa(C_{12} + C_{21}) \tag{3.21}$$

$$V \equiv i\kappa(C_{21} - C_{12}) \tag{3.22}$$

where κ is a dimensionless factor which converts the tensor elements into intensity units. When defined thus, I corresponds to the unpolarized, or total, intensity; Q and U describe the linear polarization of the wave; and V corresponds to the difference between the right-handed and left-handed circular polarization states. Since these correspond to the polarization states of σ components, the Stokes V parameter holds the key to detecting the line-of-sight component of a magnetic field.

Finally, if we put the Stokes parameters into a vector:

$$\mathbf{I} = \begin{pmatrix} I \\ Q \\ U \\ V \end{pmatrix} \tag{3.23}$$

we obtain the following generalized radiative transfer equation:

$$\frac{d\mathbf{I}}{d\tau} = -\mathbf{K}\mathbf{I} + \mathbf{j} \tag{3.24}$$

where τ is the optical depth, $\mathbf{K}$ is the *propagation matrix* and $\mathbf{j}$ is the polarized emissivity. Of course, this is quite reminiscent of the familiar unpolarized radiative transfer equation, which is presented in detail in Chapter 5. One major difference between these two equations is that the polarized radiative transfer equation corresponds in reality to four coupled equations and is therefore that much more complicated to solve.

One particularly useful solution to the polarized radiative transfer equation can

be obtained analytically in the case of a Milne-Eddington atmosphere, the so-called "Unno-Rachkovsky" solution [Unno, 1956, Rachkovsky, 1961]. However, in most of the cases which are relevant to us, there is a simpler method to approximate the polarized line profiles. The *weak-field approximation* [Landi Degl'Innocenti and Landolfi, 2004] can be used when the Zeeman splitting is small compared to the line width. Since massive stars typically have intrinsically broad lines, this assumption is usually valid, except for the most extreme cases (e.g., NGC 1624-2, Wade et al. 2012). In this approximation, the first-order solution to the *local* Stokes V profile emerging from a point on the stellar disk in velocity space is:

$$V(v) = -\frac{e}{4\pi mc^2} c g_{\rm eff} \lambda_0 B_z \frac{{\rm d}I(v)}{{\rm d}v} \tag{3.25}$$

where e is the electron charge, m is its mass, c is the speed of light, $g_{\rm eff}$ is the effective Landé factor[3], B_z is the line-of-sight (or longitudinal) component of the magnetic field at that point and v is the velocity. Then, to obtain the full profile, we calculate local profiles for each point on the surface and perform disk integration[4].

3.3 ESPaDOnS and NARVAL

Currently, two of the best, existing instruments to carry out spectropolarimetric observations of stars are the Echelle SpectroPolarimetric Device for the Observation of Stars (ESPaDOnS), installed on the 3.6m Canada-France-Hawaii Telescope (CFHT), and NARVAL, installed on the 2m Télescope Bernard-Lyot (TBL). They are twin

[3]This parameter simplifies the computation of the splitting for a given transition, and following the same notation as Eq. 3.17, it is defined as $g_{\rm eff} \equiv \alpha g'_L + m(g'_L - g_L)$.

[4]Disk integration will be presented in further detail in Chapter 5 when discussing photospheric line synthesis.

instruments and both have been used to obtain the data described in Chapter 4. As can be inferred from Eq. 3.25, a high spectral resolving power is required to properly resolve Zeeman signatures in the Stokes V parameter. Consequently, both instruments have a resolution of $R \sim 65,000$ (in spectropolarimetric mode), as well as a large bandwidth extending from approximately 3,600 Å to 10,000 Å, over 40 echelle orders [Donati, 2008].

To obtain a measurement of the Stokes V spectrum, each observation in spectropolarimetric mode consists of 4 subexposures. The light entering the instrument passes through one fixed quarter-wave and two rotatable half-wave Fresnel rhombs. These are configured so as to induce any desired retardation to the incoming beam, and then the outcoming light passes through a Wollaston prism which divides it into two separate beams corresponding to orthogonal (linear) polarization states. To observe circular polarization, the rhombs are rotated in order to convert circular polarization into linear polarization, and the beams coming out of the Wollaston prism each correspond to incoming light that initially had either left-handed or right-handed circular polarization. The beams are dispersed, cross-dispersed and projected onto a CCD. Each individual spectrum is extracted to 1D, and the resulting spectra (including a diagnostic null spectrum[5] used as a basis for comparison) are computed by combining them following the method described by Donati et al. [1997]:

$$I = i_{1,\perp} + i_{1,\parallel} + i_{2,\perp} + i_{2,\parallel} + i_{3,\perp} + i_{3,\parallel} + i_{4,\perp} + i_{4,\parallel} \tag{3.26}$$

[5]This is a spectrum which is computed by combining the beams in such a way that the signal cancels out, yielding a diagnostic which characterizes the level of noise in the Stokes V spectrum.

$$V/I = \frac{i_{1,\perp}/i_{1,\parallel}}{i_{2,\perp}/i_{2,\parallel}} \frac{i_{4,\perp}/i_{4,\parallel}}{i_{3,\perp}/i_{3,\parallel}} \tag{3.27}$$

$$N/I = \frac{i_{1,\perp}/i_{1,\parallel}}{i_{4,\perp}/i_{4,\parallel}} \frac{i_{2,\perp}/i_{2,\parallel}}{i_{3,\perp}/i_{3,\parallel}} \tag{3.28}$$

where I is the Stokes I spectrum, V/I is the *relative* Stokes V spectrum (in other words the Stokes V spectrum divided by the Stokes I spectrum), N/I is the relative null spectrum, and $i_{j,\perp}$ and $i_{j,\parallel}$ are respectively the perpendicular and parallel spectra produced by the Wollaston prism for the j^{th} subexposure.

This reduction, as well as the wavelength calibration, is performed using the Libre-ESpRIT reduction pipeline, which is run at CFHT [Donati et al., 1997].

3.4 Oblique rotator model

To understand the variation of the observed magnetic configuration of a massive star over time, we most often use the *oblique rotator model* developed originally by Stibbs [1950] to explain the variations observed in HD 125248. The main assumption of this model is that the magnetic field is stable and it rotates with the star; therefore, given an angle of i between the rotation axis and the line of sight and an angle β between the rotation axis and the magnetic axis, we can find the angle α between the magnetic axis and the line of sight for any rotational phase ϕ (in radians):

$$\cos\alpha = \cos i \cos\beta + \sin i \sin\beta \cos\phi \tag{3.29}$$

If we assume a purely dipolar configuration, the magnetic field $\mathbf{B}$ is given by:

$$\mathbf{B} = \frac{B_{\rm p}}{2r^3}(2\cos\theta_{\rm B}\ \hat{r} + \sin\theta_{\rm B}\ \hat{\theta_{\rm B}}) \tag{3.30}$$

where $B_{\rm p}$ is the magnitude of the magnetic field at the magnetic pole, and $(r, \theta_{\rm B})$ are the usual distance and colatitude used to express spherical coordinates in the magnetic reference frame (therefore, the magnetic axis corresponds to $\theta_{\rm B} = 0$), and the associated unitary vectors are noted with a "hat".

Given certain values of $B_{\rm p}$, i and β, it is possible to compute the surface magnetic field of the star at any given time and to rotate in the line-of-sight reference frame so as to determine the value of the longitudinal magnetic field at any point across the stellar disk. Using this knowledge together with the weak-field approximation (Eq. 3.25), it is possible to predict the variation of the Stokes V profile with phase; this will form the basis of the method discussed in Sect. 3.6.

3.5 Least-Squares Deconvolution and calculating the longitudinal magnetic field

One important problem that is encountered when performing magnetometry of massive stars is that the polarized signal in individual spectral lines is extremely faint, and would require an extremely large signal-to-noise ratio (SNR) in order to be detected. One way to accomplish this would be to observe a star for a very long time, but if the star is rotating quickly, the visible magnetic configuration might change between the beginning of the exposure and its end, therefore smearing the signal. However, since many spectral lines should all be affected by a magnetic field, it is possible to recover the signal using a multiline approach. This approach is called *Least-Squares Deconvolution*, or LSD [Donati et al., 1997, Kochukhov et al., 2010]. Since, in the

weak-field approximation, the local Stokes V profiles depend on the derivative of the total intensity profile, the disk-integrated Stokes V profiles of various lines should all be similar in shape if the Stokes I profiles are. Therefore, the spectrum can be considered as a series of Dirac δ functions with various weights (proportional to the Landé factor, the central wavelength and the central line depth; this series is called a *line mask*) convolved with a function representing the line profile. By deconvolving the spectrum, it is thus possible to recover the latter function, reducing the noise so as to recover a detectable signal.

This procedure can be written as a linear system. If we write the Stokes V spectrum ($\mathbf{V}$) as:

$$\mathbf{V} = \mathbf{M} \cdot \mathbf{Z} \tag{3.31}$$

where $\mathbf{M}$ is the line mask and $\mathbf{Z}$ is the underlying line profile, then we can recover that profile using a least-squares solution:

$$\mathbf{Z} = ({}^t\mathbf{M} \cdot \mathbf{S}^2 \cdot \mathbf{M})^{-1}\ {}^t\mathbf{M} \cdot \mathbf{S}^2 \cdot \mathbf{V} \tag{3.32}$$

Here, $\mathbf{S}$ represents a square diagonal matrix where each element is the inverse of the error bar for each spectral pixel. Part of the work involved in performing this technique is to define the line mask. To do so, there are two key variables to determine for each line: its Landé factor (g) and its central depth (d). The Landé factors can be found in atomic databases such as the Vienna Atomic Line Database (VALD; Kupka et al. 2000), while the depths can be found using the Stokes I profile (which can be considered as the convolution of a line mask consisting of Delta functions weighted

by d and a generic rotationally-broadened line profile). In practice, this is done by adjusting theoretical depths to fit the actual spectrum of a star.

There are some caveats to this method. First, the self-similarity condition usually prevents the use of certain strong lines, e.g., Balmer lines, which have a different shape than the rest. Furthermore, the hottest stars have much fewer lines than their colder counterparts, and since they are typically much more broadened, there are much more blends. While LSD does improve the signals for these stars, the constraints which can be placed on their magnetic fields are usually much worse than the constraints placed on, e.g., A stars. Nevertheless, this technique, performed on high resolution, high SNR spectropolarimetric data, yields the best magnetic constraints available today.

Finally, it is possible to calculate the disk-averaged longitudinal magnetic field using the first-order moment of the Stokes V LSD line profile [Mathys, 1989]. We obtain:

$$\langle B_z \rangle = -2.14 \times 10^{11} \frac{\int vV(v)dv}{\lambda gc \int [I_c - I(v)]dv} \tag{3.33}$$

where B_z is the mean longitudinal field (in gauss), v is velocity, $V(v)$ is the Stokes V profile, λ is the central wavelength, g is the Landé factor, c is the speed of light, I_c is the continuum intensity and $I(v)$ is the Stokes I profile.

An important practical consideration when computing this quantity is the integration limits which are used, as they will impact not only the obtained value, but especially the associated error bar. Typically, they are chosen by visually determining the extent of the Stokes I profile (e.g., Wade et al. 2000).

3.6 Bayesian statistics and inference

When evaluating the performance of various models in reproducing observational data, or trying to estimate the parameters of a model, a powerful statistical paradigm that can be used is Bayes' theorem [Bayes and Price, 1763]. It is generally expressed as follows:

$$p(H_i|D, I) = \frac{p(H_i|I)p(D|H_i, I)}{p(D|I)} \tag{3.34}$$

The term on the left-hand side of the equation represents the *posterior probability*, that is, the probability that the given hypothesis or set of parameters (H_i) is "true" given the data (D) and the prior information (I). In the numerator of the right-hand side of the equation, the first term is the *prior probability*, or in other words the probability previously assigned to hypothesis H_i given the prior information; the second term is the *likelihood* of the data, which is calculated, assuming that the model or hypothesis is correct, by calculating the probability of obtaining the dataset given the error bars on the measurements (most often considering Gaussian errors). Finally, the term in the denominator of the right-hand side is the *global likelihood* for the entire set of hypothesis and acts essentially as a normalization factor.

Bayesian statistics provide a learning model, building upon prior information with new data to obtain a revised assessment of the various hypotheses. One very powerful feature of this method is that it implicitly takes into account *Occam's razor*, meaning that simpler hypotheses will typically be favoured over complicated ones if both explain the data equally well.

The detailed implementation of this technique to infer dipolar magnetic field

strengths and orientations is described by Petit and Wade [2012]. In particular, the model being evaluated is the oblique rotator model, using a pure dipole, and the recovered parameters are $B_{\rm p}$, i, β; Stokes V profiles are computed using the weak-field approximation for a grid of parameters and compared to the data, and *probability density functions* are evaluated for each individual parameter by performing "marginalization", i.e., integrating the posterior probability over the other parameters. Another advantage of this technique is that it is better informed by repeated observations, since they must simultaneously correspond to two phases of the same magnetic configuration, therefore placing tighter constraints on the dipole parameters.

Chapter 4

Paper I: Placing constraints on dipolar magnetic fields

Paper Title[1]: "Investigating the origin of cyclical wind variability in hot, massive stars - I. On the dipolar magnetic field hypothesis"

[1]This chapter contains a version of a paper published in Monthly Notices of the Royal Astronomical Society as: A. David-Uraz, G.A. Wade, V. Petit, A. ud-Doula, J.O. Sundqvist, J. Grunhut, M. Shultz, C. Neiner, E. Alecian, H.F. Henrichs, J.-C. Bouret, the MiMeS Collaboration, 2014, MNRAS, 444, 429 (Oxford University Press)

4.1 Abstract

OB stars exhibit various types of spectral variability associated with wind structures, including the apparently ubiquitous discrete absorption components (DACs). These are proposed to be caused by either magnetic fields or non-radial pulsations (NRPs). In this paper, we evaluate the possible relation between large-scale, dipolar magnetic fields and the DAC phenomenon by investigating the magnetic properties of a sample of 13 OB stars exhibiting well-documented DAC behaviour.

Using high-precision spectropolarimetric data acquired in part in the context of the Magnetism in Massive Stars (MiMeS) project, we find no evidence for surface dipolar magnetic fields in any of these stars. Using Bayesian inference, we compute upper limits on the strengths of the fields and use these limits to assess two potential mechanisms by which the field may influence wind outflow: magnetic wind confinement and local photospheric brightness enhancements. Within the limits we derive, both mechanisms fail to provide a systematic process capable of producing DACs in all of the stars of our sample. Therefore, this implies that dipolar fields are highly unlikely to be responsible for these structures in all massive stars, meaning that some other mechanism must come into play.

4.2 Introduction

The importance of mass loss in the evolution of massive stars has been increasingly recognized over the past 20 years (e.g. Cuntz and Stencel 1992). However, the radiatively-driven winds [Castor et al., 1975] of OB stars are host to a number of forms of instability (e.g. Sundqvist and Owocki 2013) and other competing physical processes which are not yet fully accounted for in models. Thus an important piece

of the puzzle is missing to achieve a global understanding of these stars and of their characteristically strong outflows. This is evidenced by different forms of spectral variability in wind-sensitive lines.

First, there are stochastic variations, which can occur over very short timescales (minutes). These are believed to be related to instability mechanisms, such as clumping, and can be found notably atop the broad emission lines of Wolf-Rayet stars (e.g. Moffat et al. 1994).

On the other hand, there are also cyclical (or quasi-periodic) variations which occur typically over longer timescales (for a complete review of the various forms cyclical variations can take, see Fullerton 2003). One example consists of the so-called "periodic absorption modulations", or PAMs, observed in a number of OB stars (e.g. Massa et al. 1995) and which manifest themselves as optical depth modulations in the absorption troughs of ultraviolet (UV) P Cygni profiles. They can show a "phase-bowing", appearing at intermediate velocities and bending slightly upwards in the dynamic spectra, therefore occuring quasi-simultaneously at all velocities shortly thereafter (as in HD 64760, Fullerton et al. 1997). PAM variabilities occur on intermediate timescales (hours) and their physical cause is not known.

In parallel, one of the most common forms of cyclical variability among OB stars is the presence of so-called "discrete absorption components" (DACs). These features are formed in the UV resonance lines of hot massive stars and appear as narrow, blueward-travelling absorption structures. Their progression from low to near-terminal velocity over time distinguishes this form of variability from the aforementioned PAMs. As was first shown in time series of IUE spectra [Prinja and Howarth, 1986], DACs recur cyclically on longer timescales (days) and at relatively

well-constrained periods. These timescales were found to be correlated with the projected rotational velocity ($v \sin i$), suggesting that these variations are rotationally modulated [Prinja, 1988]. DACs are thought to be present in all OB stars. Indeed, narrow absorption components (NACs; narrow absorption features typically found near terminal velocity), believed to be snapshots of DACs, are found in nearly all massive stars observed by IUE [Howarth and Prinja, 1989]. However, this does not mean that all DACs are identical. Their depths vary from one star to another (they can even be opaque), and it is possible to find more than one DAC at a time in single observations [Kaper et al., 1996]. Because they span the full range of velocities over time, it is believed that they are caused by large-scale azimuthal structures extending from the base of the wind all the way to its outer regions [Mullan, 1986]. Cranmer and Owocki [1996] showed that a perturbation in the photosphere could lead to co-rotating interaction regions (CIRs), although the physical nature of this perturbation is not yet known. This model seems consistent with the DAC phenomenon and leads to promising simulated spectral signatures. The goal of this project is to determine what physical process constitutes the origin of DACs. Obviously, there are far-reaching implications for the general study of massive stars, since DACs are believed to be common to all OB stars.

The two leading hypotheses to explain DACs are magnetic fields and non-radial pulsations (NRPs). However, both processes present a number of challenges when it comes to explaining DACs. First, based on the statistics of the Magnetism in Massive Stars (MiMeS) survey, less than 10% of all massive stars are inferred to harbour detectable magnetic fields [Wade et al., 2014]. This is obviously a problem since DACs are thought to be common to all OB stars. On the other hand, a pulsational origin for

Table 4.1: Sample of stars used for this study; spectral types are obtained from Howarth et al. [1997] and references therein. $N_{\rm obs}$ corresponds to the total number of independent observations for each star, $\Delta t_{\rm E}$, $\Delta t_{\rm N}$ and $\Delta T_{\rm max}$ correspond respectively to the average individual total exposure time for ESPaDOnS and NARVAL, and the maximum time elapsed between the first and last observation of a star on any given night (N/A for stars with only one observation per night).

HD	Name	Spectral Type	m_V	$N_{\rm obs}$	$\Delta t_{\rm E}$ (s)	$\Delta t_{\rm N}$ (s)	$\Delta T_{\rm max}$ (d)
24912	ξ Per	O7.5 III(n)((f))	4.06	44	360	$\sim$ 1800	0.186
30614	α Cam	O9.5 Ia	4.30	11	560	920	0.037
34656		O7 II(f)	6.80	1	2600	-	N/A
36861	λ Ori A	O8 III((f))	3.30	20	$\sim$ 200	$\sim$ 400	0.039
37128	ϵ Ori	B0 Ia	1.70	70	40	$\sim$ 160	0.122
47839	15 Mon	O7 V((f))	4.64	16	640	$\sim$ 1600	0.035
64760		B0.5 Ib	4.23	9	440	-	0.033
66811	ζ Pup	O4 I(n)f	2.25	30	80	-	0.078
149757	ζ Oph	O9.5 V	2.58	65	100	180	0.061
203064	68 Cyg	O7.5 III:n((f))	5.04	8	980	$\sim$ 2000	0.053
209975	19 Cep	O9.5 Ib	5.11	33	1000	1800	0.093
210839	λ Cep	O6 I(n)fp	5.08	26	-	2640	N/A
214680	10 Lac	O9 V	4.88	36	400	$\sim$ 2000	0.051

DACs might also be problematic, since one would expect a succession of brighter and darker areas on the photosphere, whereas Cranmer and Owocki [1996] specifically identify bright spots as the possible cause for DACs. Moreover, experiments with alternating bright and dark regions, meant to simulate the brightness distribution of low-order NRPs, failed to reproduce DAC-like variations (Owocki, priv. comm.). On the other hand, rotational modulations (RMs; analogous to PAMs) have been modelled self-consistently with a 3D radiative transfer code using NRPs in HD 64760 [Lobel, 2013], a star possessing DACs; however, the NRPs produce the RMs, while the DACs are created by introducing bright spots. Finally, DAC recurrence timescales are deemed to be incompatible with pulsational periods and it has been suggested that

this problem can only be solved through complex mode superpositions [de Jong et al., 1999]. This paper investigates the simplest form of the first case: that of a purely dipolar large-scale magnetic field, inclined relative to the rotation axis. Indeed, most massive stars are thought to produce two DACs per rotational period [Kaper et al., 1996], so this configuration seems like a rather natural fit. Moreover, most detected magnetic fields in OB stars are essentially dipolar, and follow the oblique rotator model [Wade and the MiMeS Collaboration, 2010]. This is expected, since large-scale magnetic fields in massive stars are believed to be of fossil origin, relaxing into a dipolar configuration [Braithwaite and Nordlund, 2006, Duez and Mathis, 2010]. On the other hand, relatively weak magnetic fields, possibly below the threshold of detection for most MiMeS observations, could still introduce a significant modulation of the winds of OB stars.

In this paper, we examine a sample of 13 stars well known to exhibit DACs. The sample is described in detail in Sect. 4.3. In Sect. 4.4, we describe the high-resolution spectropolarimetric observations of these stars, as well as the instruments on which they were obtained. Sect. 4.5 outlines the least-squares deconvolution (LSD) procedure used to maximize the signal-to-noise ratio of the Stokes V profiles to search for Zeeman signatures. In Sect. 4.6, we present the various diagnostics used to perform the most precise magnetometry ever obtained for this class of stars. Sect. 4.7 contains notes on individual stars, while the results are discussed and analyzed in detail in Sect. 4.8, as well as the conclusions of this study and pointers for future investigations.

4.3 Sample

Thirteen OB stars (with spectral types ranging from O4 to B0.5, and luminosity classes from V to Ia, see Table 4.1) were selected to form this sample based on two main criteria: documented DAC behaviour, and available high-quality data.

All stars selected for this sample are well known to exhibit the DAC phenomenon and were extensively studied as such: 9 stars were studied by Kaper et al. [1996], ζ Pup was investigated by Howarth et al. [1995], while ζ Oph was the subject of a paper by Howarth et al. [1993]. Finally, the two B supergiants (ϵ Ori and HD 64760) were studied by Prinja et al. [2002]. The suspected ubiquitous nature of DACs indicates that the physical process causing them should be common to all OB stars. Therefore, if this process involves large-scale dipolar magnetic fields, we expect to detect such fields in most of the stars of this sample.

Furthermore, data accessibility was one of the key factors in choosing this sample. Indeed, these stars were selected because available archival data (high-resolution spectropolarimetry) related to the MiMeS Project allow us to conduct high-precision magnetic measurements and compile a self-consistent dataset.

The stellar and wind parameters of all stars in the sample are presented in Table 4.2. For consistency with Kaper et al. [1996], most of the values we use are taken from that paper. Thus, for the 11 O stars, the mass-loss rates are obtained by applying the empirical prescription of Lamers and Leitherer [1993], which relies on radio free-free emission and Hα measurements using unclumped models. As for the 2 B stars, mass-loss rates are taken from Searle et al. [2008] (based on optical/UV spectroscopy). Comparison of the adopted stellar and wind parameters with more modern values (e.g. Markova et al. 2004, Repolust et al. 2004, Najarro et al. 2011,

Bouret et al. 2012) yield only minor differences in $T_{\rm eff}$ (typically about 1 kK, $\sim 5\%$), R_* (a few $R_\odot$, $\sim 20\%$) and v_∞ (essentially identical). For the mass-loss rates, modern values typically differ from one another by a factor of a few, up to a full order of magnitude, depending on each star. In general, our values are consistent with the lower end of that range.

4.4 Observations

The observations were obtained at the Canada-France-Hawaii Telescope (CFHT) on the ESPaDOnS instrument, and on its sister instrument, NARVAL, installed at Télescope Bernard Lyot (TBL). Some observations were obtained as part of the Large Programs (LPs) awarded to MiMeS on both instruments, while a significant part of the dataset was obtained as part of individual PI programs (led by V. Petit, C. Neiner, E. Alecian, H. Henrichs and J.-C. Bouret). Both of these instruments are high-resolution ($R \sim 65,000$) fibre-fed échelle spectropolarimeters. Each exposure consists of 4 sub-exposures corresponding to different angles of the Fresnel rhomb retarders, which are then combined in different ways to obtain both the I (unpolarized) and V (circularly polarized) Stokes parameters, as well as two diagnostic nulls (which have the same noise level as the V spectrum, but no stellar magnetic signal, Donati et al. 1997). The spectral coverage is essentially continuous between about 360-1000 nm. The reduction was performed using the Libre-ESpRIT package at the telescope, and the spectra were then normalized to the continuum. Appendix A contains a summary of all the observations.

The use of these observations marks a significant improvement in the study of the role of magnetic fields in the generation of wind variability because of both their high

resolution and high signal-to-noise ratio (SNR). They constitute the highest-quality dataset compiled to date for the purpose of magnetometry on OB stars. Furthermore, the extensive time coverage obtained for a number of stars in the sample can provide extremely tight constraints on the geometry of any surface magnetic field present (see Sect. 4.6). In total, this dataset is constituted of 381 spectra, for an average of nearly 30 spectra per star (HD 34656 only has 1 observation, while ϵ Ori has 70). The data were acquired between 2006 and 2013, with a typical peak SNR of over 1000 per CCD pixel at a wavelength of around 550 nm.

4.5 Least-Squares Deconvolution

In order to improve the significance of potential Zeeman signatures in the Stokes V profile, indicative of the presence of a magnetic field, LSD [Donati et al., 1997] was used to effectively deconvolve each spectrum to obtain a single, high-SNR line profile. This was carried out using the latest implementation of iLSD [Kochukhov et al., 2010].

This procedure requires the use of a specific "line mask" for each star, which is a file containing all the necessary information about the lines whose signal will be added: central wavelength, depth and Landé factor. First, to create such a file, a line list is obtained from the Vienna Atomic Line Database (VALD, Kupka et al. 2000), by inputting the effective temperature of the star, and choosing a line depth threshold (0.01 in this case). Then, the information contained in the line list is used to create a crude preliminary mask, which can then be filtered and adjusted. This means that some lines are removed (e.g. lines which don't actually appear in the spectra, lines heavily contaminated by telluric absorption, hydrogen lines, due to their particular

shape and behaviour, as well as lines which were blended with hydrogen lines), while the depths of the remaining lines can be adjusted to better reproduce the star's spectrum. This procedure also ensures that uncertainties in $T_{\rm eff}$ have little impact on the final mask.

Several tests were made with sub-masks to determine which of the remaining lines should be included or not. In the end, masks including helium and metallic lines were used, as the helium lines provided most of the signal and did not alter the shape of the mean line profile significantly (although they do introduce extra broadening). The LSD profiles were then extracted using these masks, without applying a regularisation correction [Kochukhov et al., 2010] since it did not yield significant gain given the already high SNR of the spectra.

Another measure taken to improve the signal was to co-add the LSD profiles of spectra of each star taken on the same night. The time intervals between the first and last exposure of a given star on a given night are systematically less than 10% of the inferred stellar rotational period, therefore there was no serious risk of smearing the signal and weakening it (see Table 4.1). A mosaic of sample nightly-averaged LSD profiles for each of the stars is presented in Fig. 4.1.

4.6 Magnetic field diagnosis

The LSD profiles were used to assess magnetic fields via two techniques: direct measurement diagnostics and Bayesian inference-based modeling.

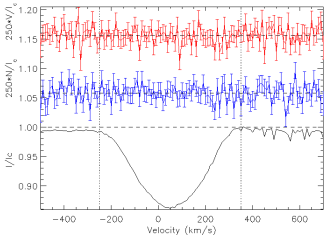

(a) ξ Per LSD profile.

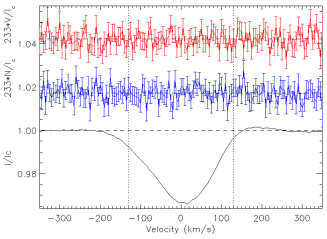

(b) α Cam LSD profile.

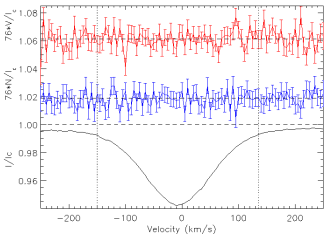

(c) HD 34656 LSD profile.

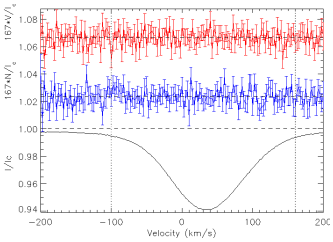

(d) λ Ori A LSD profile.

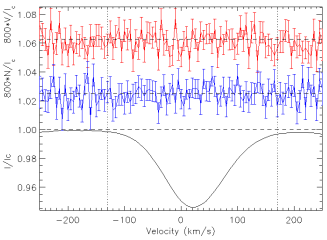

(e) ϵ Ori LSD profile.

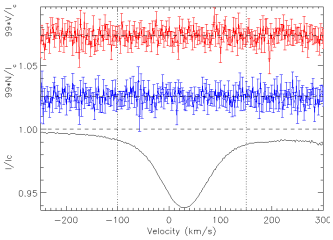

(f) 15 Mon LSD profile.

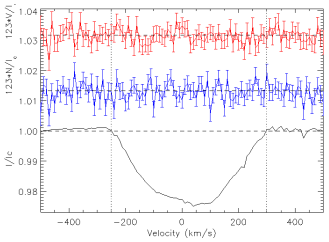

(g) HD 64760 LSD profile.

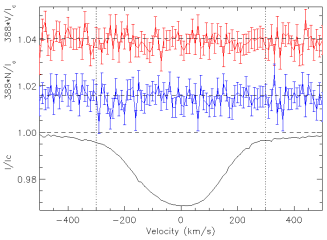

(h) ζ Pup LSD profile.

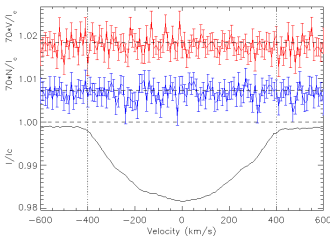

(i) ζ Oph LSD profile.

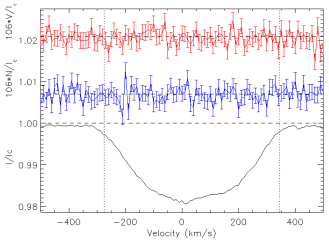

(j) 68 Cyg LSD profile.

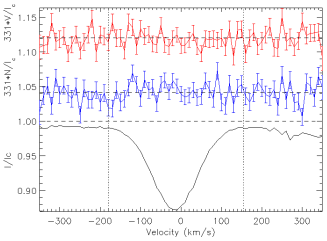

(k) 19 Cep LSD profile.

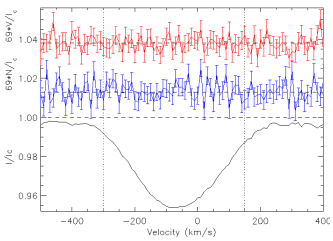

(l) λ Cep LSD profile.

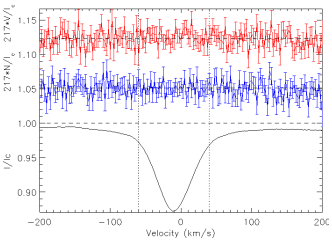

(m) 10 Lac LSD profile.

Figure 4.1: Typical LSD profiles for all stars in the sample. In each plot, the red line (top) is the Stokes V profile, while the blue line (middle) is a diagnostic null. Finally, the black line (bottom) is the Stokes I profile. The dotted lines represent the integration range for each star. We can see that no perceptible signal is found in any of the V profiles.

4.6.1 Direct measurement diagnostics

Using the nightly-averaged profiles, as well as the individual ones, the disc-averaged longitudinal magnetic field (B_z) was computed using the first-order moments method (e.g. Wade et al. 2000). The integration ranges were chosen carefully, after a few trial calculations to determine how to minimize the error bars without losing any potential signal. Visually, the limits correspond loosely to the zero-points of the second derivative of the Stokes I profiles. Nightly longitudinal field measurements are listed in Table A.1. There are no significant detections. Not only do they seem normally distributed within the error bars, but these error bars are quite small in some cases and provided very tight constraints (e.g. 4 G error bar for 10 Lac on 17 October 2007). Furthermore, the longitudinal fields are also measured using the diagnostic nulls as a sanity check. On any given night, the error bars for the longitudinal fields measured from the V profile are consistent with those measured from the nulls, and the distributions of B_z/σ_{B_z} obtained from each profile are essentially identical, which suggests that the V profile does not contain any more signal than the diagnostic nulls.

χ^2 diagnostics are also performed by comparing both the V profile and the diagnostic null to the null hypothesis ($B = 0$, therefore $V = 0$ and $N = 0$), and detection probabilities are derived from these values [Donati et al., 1997]. These calculations are performed both within the LSD profile, as well as in the continuum. A detection probability below 99.9% is considered as a non-detection, a marginal detection possesses a detection probability between 99.9% and 99.999% and a definite detection has a detection probability of over 99.999% (for a discussion of these thresholds, see Donati et al. 1997). The 400+ individual and nightly-averaged V profiles are all non-detections, except 5 cases within the profile (1 in ζ Oph, 3 in 19 Cep and 1 in

10 Lac) and 1 in the continuum (in ξ Per) all 6 of which are marginal detections. For the ones inside the line, except for a nightly-averaged observation in 10 Lac, the other 4 occurrences appear in individual observations, with a lower SNR. This could be due to somewhat noisier profiles, and since they are relatively isolated cases (for all 3 stars there are many more observations which are all non-detections), they are not perceived as being significant. As for the continuum marginal detection, it is also from a single observation and could be due to noise, as well as slight telluric contamination. On the whole, these results are largely consistent with those for the diagnostic nulls, further suggesting that there are no real detections.

In summary, both of these direct measurement diagnostics lead to the same conclusion, i.e. that no magnetic field is observed in any of these stars.

4.6.2 Bayesian inference

Additionally, to increase the SNR it is also possible to take advantage of the time resolution provided by repeated measurements. Indeed, taking into account the oblique dipole rotator model [Stibbs, 1950], data taken at different times should allow to view the surface magnetic field from different perspectives, thus lifting some of the degeneracy associated with the geometric parameters of the magnetic field, should it exist. Therefore, using the technique developed by Petit and Wade [2012], a fully self-consistent Bayesian inference method compares the observed profiles in the Stokes V and N parameters to synthetic Zeeman profiles for a grid of field strength and geometry parameters. The rotational phase of the observations is also allowed to vary freely, since rotational periods are unknown.

In order to produce synthetic Zeeman profiles to be used for this Bayesian technique, it is necessary to estimate the value of the projected rotational velocity of each star, as well as its macroturbulent velocity. These values are sometimes degenerate and difficult to determine with great precision. Instead of using previously published values, new values of $v \sin i$ were measured for all stars using the Fourier transform method (e.g. Simón-Díaz and Herrero 2007, Gray 2005). To this effect, synthetic spectra were computed with SYNTH3 [Kochukhov, 2007], and the OII λ4367, OIII λ5508, OIII λ5592 and CIV λ5801 lines were used to compare them to the data. In most cases (10/13), we get relatively (e.g. 20%) lower values of projected rotational velocity than those reported in the literature [Howarth et al., 1997], while for the 4 remaining stars, we get comparable or slightly higher results. This can be expected, since the line broadening is no longer solely attributed to rotation with this method.

Once the value of $v \sin i$ was determined, the LSD profiles (rather than individual lines, since these are the data we are looking to model) were then compared to synthetic Voigt profiles to refine the value of $v \sin i$ and determine v_{mac}. Because this process involved some level of degeneracy, the uncertainty on the obtained values could not be determined in a systematic way, but it is conservatively estimated to be about 10-20%. While this may seem large, tests using different pairs of values ($v \sin i$ and the associated v_{mac}) indicate that such a precision is quite sufficient, as errors of this magnitude do not significantly affect the results of the Bayesian analysis. A summary of these velocity measurements is given in Table 4.2, which also contains other relevant physical parameters. The macroturbulent velocities are likely to be systematically overestimated; the extra broadening from the helium lines behaves in a way similar to macroturbulence. However once again, extensive testing on our

data has shown that this overestimation does not significantly alter the results of the Bayesian inference.

Ultimately, we modeled the observed I, V and N profiles to obtain probability density functions (PDFs) for 3 variables: the dipolar field strength (B_d), the inclination angle of the rotational axis (i) and the obliquity angle between the magnetic field axis and the rotational axis (β). It is also possible to marginalize the PDFs for each variable individually. However, it should be noted that the latter two geometric parameters cannot be constrained in the case of non-detections [Petit and Wade, 2012]. Fig. 4.2 shows the marginalized PDFs for three representative stars as a function of B_d. We can see that for each star, the PDF peaks at a value of 0, which is consistent with a non-detection. Additionally, a similar analysis was performed on the diagnostic null, with consistent results. Therefore, we obtained no information about the putative field's geometry: we consider the only parameter of interest for this study to be the strength of the dipolar field. Since we only have non-detections, we can place upper limits on the dipolar field strength by using the 95.4% confidence region upper boundaries (which corresponds to the limit over which we expect the field to be detected, Petit and Wade 2012). These upper limits (noted as $B_{d,\max}$) are listed in Table 4.2 (as well as the 68.3% confidence level upper limits for comparison purposes). The highest upper limit (95.4% interval) that we derive is that of HD 34656 (359 G). This is expected, since there was only a single observation for that star, therefore a lower SNR. The tail of the PDF falls off less abruptly as well (see Fig. 4.2), since statistically speaking, the observation could correspond to a particular phase where the field configuration is not suitable for detection. It should be remembered that this technique aims to take advantage of timeseries of LSD profiles; hence

better constraints and a more peaked PDF could be obtained for this star with higher SNR observations and more extensive time coverage. All the other stars with upper limits over 100 G (5) have very high projected rotational velocities, which explains their poorer constraints. However, for the rest of the stars (7), we get extremely tight constraints, in particular in the case of 10 Lac (23 G). These values represent by far the tightest constraints ever obtained for any sample of OB stars (see Fig. 4.3 for a histogram of these upper limits).

However, even though fast rotating stars have poorer constraints on the strength of their hypothetical dipolar field, their rotation itself suggests that they do not possess such a field (or if so, a weak one). Indeed, a majority of magnetic OB stars are slow rotators. Moreover, all effectively single magnetic O stars are very slow rotators, with periods ranging from about one week to decades (e.g. Petit et al. 2013). This slow rotation is thought to be achieved by the magnetic field, which contributes to remove angular momentum from a star. This characteristic does not apply to our sample, in which nearly half (6/13) of the stars have projected rotational velocities of over 200 km/s. We can calculate a typical spindown timescale for a given magnetic field strength (see Eq. 8 of Ud-Doula et al. 2009). For example, if we perform that calculation on the supergiant HD 64760 using the 95.4% interval upper limit on the strength of the field, we get a spindown timescale of just under a million years, which seems incompatible with its projected rotational velocity of 250 km/s.

Another output of the Bayesian analysis is the *odds ratio*. This value represents the ratio of the likelihoods of each of the two hypotheses to be evaluated: H_0, corresponding to no magnetic field, and H_1, corresponding to a globally organized dipolar magnetic field. According to Jeffreys [1998], we would need an odds ratio below 1/3

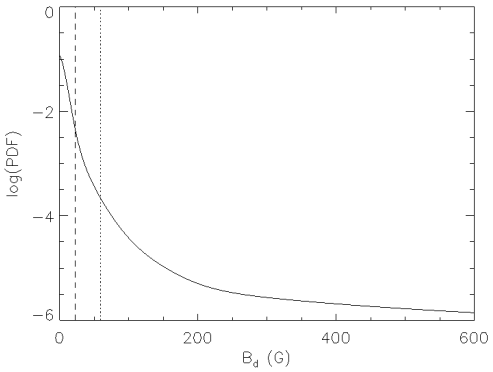

(a) B_d PDF for 10 Lac.

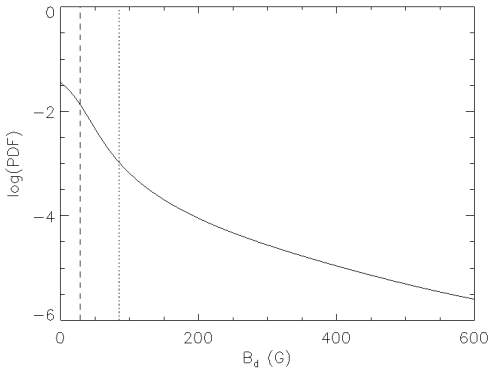

(b) B_d PDF for α Cam.

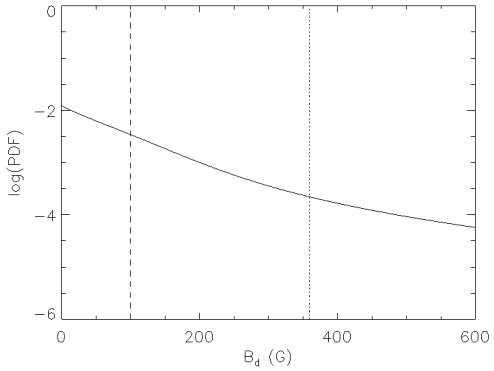

(c) B_d PDF for HD 34656.

Figure 4.2: Logarithm of the probability density functions of the dipolar field strength (B_d) for three representative stars (10 Lac with the best constraints at the top, α Cam with typical constraints in the middle, and HD34656 with the worst constraints at the bottom) as derived from the Bayesian inference technique. For each plot, the dashed line delimits the 68.3% confidence interval, while the dotted line delimits the 95.4% confidence interval.

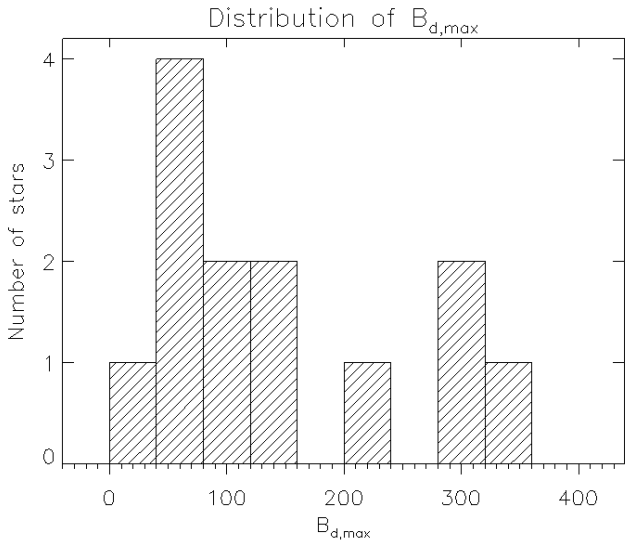

Figure 4.3: Histogram of the $B_{d,\max}$ (95.4% interval upper limit) values derived from the Bayesian analysis (Table 4.2). Most stars have an upper limit below 120 G.

to say that there is weak evidence in favour of the magnetic hypothesis. This ratio has been computed for each star (for the individual nightly observations, as well as for the entire dataset of a given star). For all V profiles, we get $odds(H_0/H_1) > 1$, except for two nightly profiles (1 for ϵ Ori and 1 for ξ Per), but they do not go under 0.68. Typical values for the joint datasets range between 1 and 10. None of the stars yield odds ratios favouring the magnetic hypothesis. These results are also consistent with the odds ratios obtained from the null spectra.

It should be noted that this approach relies on a certain stability of the field. In particular, the geometry and strength of the dipole cannot undergo significant changes during the period of observation. On the other hand, this method is insensitive to any drift of the dipole in phase (e.g. precession of the magnetic axis around the rotation axis at a non-uniform rate). We assume that the geometry of the field remains stable

over timescales of at least a few years given the temporal baseline of our observations; this assumption is found to be justified in intermediate-mass and massive stars (e.g. Wade et al. 2011, Grunhut et al. 2012, Silvester et al. 2014). In any case, for a majority of stars in the sample, most observations are grouped within a few months, periods over which secular changes in the field geometry would not be important.

Once again, this analysis supports the view that no magnetic fields are observed, but further allows us to compute quantitative upper limits on the surface dipole component, necessary for evaluating the potential influence on the stellar wind.

4.7 Notes on individual stars

The following subsections contain notes about each individual star.

4.7.1 ξ Per

ξ Per is a well-known O7.5 giant runaway star [Blaauw, 1993] whose DAC behaviour has been extensively studied in the past (e.g. Kaper et al. 1996). de Jong et al. [2001] have studied its spectral variability in a number of wind-sensitive lines and also confirm the presence of NRPs. While its high projected rotational velocity makes it harder to perform precise magnetometry, the excellent time coverage of this dataset leads to a very tight upper limit on the strength of an hypothetical dipolar field. There does not seem to be significant variation in the shape of Hα during our observing runs, but rather simply a modulation of the depth of the line (see Fig. 4.4 for a summary of the Hα profiles of all stars). Forty-four independent observations of ξ Per were acquired over 13 nights in December 2006, September 2007 and November 2011. The smallest nightly longitudinal field error bar calculated from these data is 21 G, and

Table 4.2: Stellar and magnetic parameters of the stars in the sample. Terminal wind velocities are obtained from Howarth et al. [1997] and references therein, as well as the previously published values of the projected rotational velocity (in parentheses). New values of $v \sin i$ obtained from the Fourier transform method (and refined by fitting the profiles) are reported as well. Nine stars of the sample are studied by Kaper et al. [1996] (a) and Kaper et al. [1997] (b), and all their other properties were obtained from these references (in particular, mass-loss rates are obtained using the empirical relation of Lamers and Leitherer 1993). For the B supergiants (ϵ Ori and HD 64760), Searle et al. [2008] (c) provide the radii and mass-loss rates, while the remaining parameters are obtained from Prinja et al. [2002] (d). Finally, Lamers and Leitherer [1993] (e) provide the radii, mass-loss rates and effective temperatures of ζ Pup and ζ Oph; Howarth et al. [1995] (f) detail the DAC recurrence for the former and Howarth et al. [1993] (g) do the same for the latter.

Name	R_* ($R_\odot$)	$T_{\rm eff}$ (kK)	$\dot{M}$ ($M_\odot$/yr)	v_∞ (km/s)	$v \sin i$ (km/s)	v_{mac} (km/s)	$P_{\rm max}$ (d)	$t_{\rm DAC}$ (d)	$B_{d,\rm max}$ (G)	$B_{d,68.3\%}$ (G)	$\eta_{*,\rm max}$	Ref.
ξ Per	11	36.0	$3 \cdot 10^{-7}$	2330	215 (213)	80	2.6	2.0	59	22	0.11	a
α Cam	22	29.9	$9 \cdot 10^{-7}$	1590	90 (129)	85	12.4	a few	85	28	0.48	a, b
HD 34656	10	36.8	$2 \cdot 10^{-7}$	2155	70 (91)	65	7.2	0.9	359	100	5.75	a
λ Ori A	12	35.0	$3 \cdot 10^{-7}$	2175	55 (74)	60	11.0	> 5	65	22	0.18	a
ϵ Ori	32	28.6	$2 \cdot 10^{-6}$	1910	65 (91)	55	24.9	0.7	78	29	0.31	c, d
15 Mon	10	41.0	$4 \cdot 10^{-7}$	2110	50 (67)	53	10.1	> 4.5	84	30	0.16	a
HD 64760	23	23.1	$1 \cdot 10^{-6}$	1500	250 (216)	50	4.7	a few	282	89	5.37	c, d
ζ Pup	16	42.4	$1 \cdot 10^{-6}$	2485	220 (219)	80	3.7	0.8	121	34	0.29	e, f
ζ Oph	8	35.9	$9 \cdot 10^{-8}$	1505	375 (372)	50	1.1	0.8	224	75	4.57	e, g
68 Cyg	14	36.0	$7 \cdot 10^{-7}$	2340	290 (305)	65	2.4	1.3	286	90	1.86	a
19 Cep	18	30.2	$6 \cdot 10^{-7}$	2010	56 (95)	70	16.3	~ 5	75	28	0.30	a
λ Cep	17	42.0	$3 \cdot 10^{-6}$	2300	200 (219)	80	4.3	1.4	136	50	0.15	a
10 Lac	9	38.0	$1 \cdot 10^{-7}$	1140	21 (35)	30	21.7	> 5	23	8	0.07	a

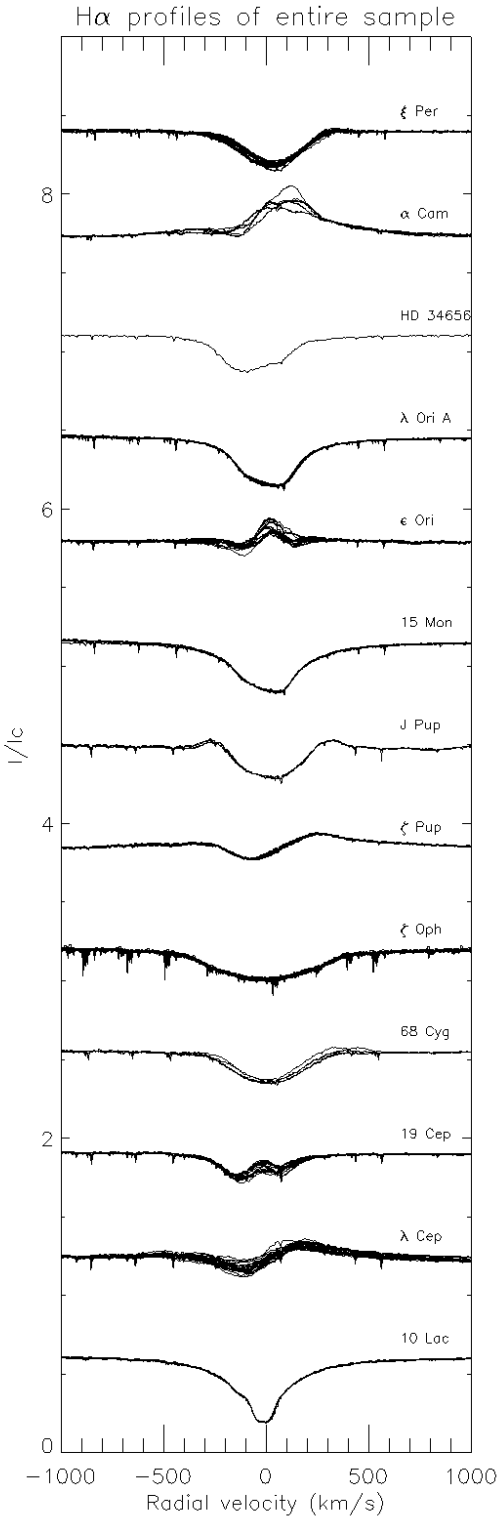

Figure 4.4: Hα profiles of all stars (offset for viewing purposes). Some stars have very little to no variability, whereas others have significant variability (variable depths, emission, etc.).

the derived dipolar field strength upper limit is 59 G.

4.7.2 α Cam

Also a runaway [Blaauw, 1993], α Cam (O9.5 supergiant) exhibits a subtler DAC behaviour [Kaper et al., 1997]. The projected rotational velocity was significantly revised (see Table 4.2). The Hα profile undergoes important changes from night to night. Eleven independent observations of α Cam were acquired over 5 nights between 2006 and 2013. The smallest nightly longitudinal field error bar calculated from these data is 10 G, and the derived dipolar field strength upper limit is 85 G.

4.7.3 HD 34656

HD 34656 is a well-studied O7 bright giant (e.g. Fullerton et al. 1991, who observed line profile variations in its spectra) with relatively low $v \sin i$, making it an interesting target for this kind of study. Kaper et al. [1996] have characterized its DAC behaviour. Unfortunately, there was only a single observation of the star in the archive, therefore it was not possible to constrain its magnetic properties with great precision. The observation of HD 34656 was acquired in November 2011. The longitudinal field error bar calculated from this observation is 38 G, and the derived dipolar field strength upper limit is 359 G.

4.7.4 λ Ori A

In a large separation double system with an early-B star (e.g. Scardia 1983), λ Ori A is a slowly-rotating O8 giant, exhibiting well-known DAC behaviour (e.g. Kaper et al. 1996). We placed a very firm upper limit on its dipolar field strength. No detectable

variations are found in Hα in our observations. Twenty independent observations of λ Ori A were acquired over 8 nights between 2007 and 2010. The smallest nightly longitudinal field error bar calculated from these data is 12 G, and the derived dipolar field strength upper limit is 65 G.

4.7.5 ϵ Ori

One of two B supergiants present in this sample, the DAC behaviour of ϵ Ori (B0) was first described by Prinja et al. [2002]. Evidence suggesting the possible presence of NRPs is offered by Prinja et al. [2004]. We derive rather tight magnetic constraints, on top of observing significant variations of the Hα profile over time. Seventy independent observations of ϵ Ori were acquired over 9 nights in October 2007, October 2008 and March 2009. The smallest nightly longitudinal field error bar calculated from these data is 6 G, and the derived dipolar field strength upper limit is 78 G.

4.7.6 15 Mon

A long period spectroscopic binary [Gies et al., 1997] with well-studied DACs [Kaper et al., 1996], 15 Mon (O7 dwarf) has low $v \sin i$, thus leading to a well-constrained field upper limit, even though it has not been observed as extensively as some other stars in this sample. Our observations of 15 Mon do not present noticeable changes in Hα. Contrarily to Hubrig et al. [2013], who claimed a 4.4 σ detection based on two observations with FORS2 and SOFIN (longitudinal field error bars of 37-52 G), we do not find evidence supporting the presence of a large-scale dipolar magnetic field despite better quality data and more numerous observations. Indeed, sixteen independent observations of 15 Mon were acquired over 8 nights in December 2006,

September-October 2007 and February 2012. The smallest nightly longitudinal field error bar calculated from these data is 20 G, and the derived dipolar field strength upper limit is 84 G.

4.7.7 HD 64760

This B0.5 supergiant was studied by Fullerton et al. [1997], who not only detect DACs, but also other forms of variability such as "phase bowing", making this star a complex but very interesting case. It is also known to exhibit signs of NRPs (e.g. Kaufer et al. 2002). However, due to its high projected rotational velocity, as well as the low number of observations, its magnetic properties are amongst the worst-constrained of this sample. There is no variation of Hα between the two nights it was observed. Nine independent observations of HD 64760 were acquired over 2 nights in November 2010 and December 2012. The smallest nightly longitudinal field error bar calculated from these data is 37 G, and the derived dipolar field strength upper limit is 282 G.

4.7.8 ζ Pup

Characterized by a very strong wind, ζ Pup is a particularly hot O4 supergiant. Its DAC behaviour was evidenced by Howarth et al. [1995], while Reid and Howarth [1996] suggest the possibility of NRPs. We provide good limits on the magnetic field, albeit with a single night of observations. Better time coverage could provide much better constraints. It is not obvious from these data whether the Hα profile varies over the course of the night. Thirty independent observations of ζ Pup were acquired over a single night in February 2012. The nightly longitudinal field error bar calculated

from these data is 21 G, and the derived dipolar field strength upper limit is 121 G.

4.7.9 ζ Oph

A well-known runaway star (e.g. Perryman et al. 1997), ζ Oph (O9.5 dwarf) possesses a very high value of $v \sin i$ and short-period DACs [Howarth et al., 1993]. Nonetheless, thanks to great time coverage, we obtain good magnetic constraints. Hubrig et al. [2013] claim this star to be magnetic, a result we do not reproduce here. Although their nightly observations possess better individual error bars, their longitudinal field curve has an amplitude of roughly 120 G and implies a surface dipole field of at least 360 G, which seems inconsistent with the 224 G upper limit we place on B_d. Period analysis performed on our longitudinal field measurements (for V and N) with PERIOD04 [Lenz and Breger, 2005] does not suggest periodic behaviour; in particular, the 0.8d and 1.3d periods reported by Hubrig et al. [2013] are not recovered. The periodogram of both the Stokes V and the null results are quite similar, further suggesting that no periodic signal is to be found. Individual Stokes I LSD profiles show strong line profile variations (LPV), in the form of bumps appearing and disappearing across the profile, which are indicative of the presence of NRPs, known to exist in this star (e.g. Walker et al. 2005). We do not detect noticeable variations in Hα from night to night in our runs. Sixty-five independent observations of ζ Oph were acquired over 46 nights in 2011 and 2012. The smallest nightly longitudinal field error bar calculated from these data is 118 G, and the derived dipolar field strength upper limit is 224 G.

4.7.10 68 Cyg

The O7.5 runaway (e.g. Gies and Bolton 1986) giant 68 Cyg is a rapid rotator with well-studied DACs [Kaper et al., 1996]. Factoring that in with a small number of observations, the putative dipolar magnetic field strength of 68 Cyg is not as well constrained as most of the other stars of the sample. However, Hα is seen to be variable, though the pattern of its variation with time is not clear. Eight independent observations of 68 Cyg were acquired over 4 nights between 2006 and 2012. The smallest nightly longitudinal field error bar calculated from these data is 46 G, and the derived dipolar field strength upper limit is 286 G.

4.7.11 19 Cep

Believed to be a multiple star system [Mason et al., 1998], 19 Cep is known to exhibit DAC behaviour [Kaper et al., 1996] and has a primary (O9.5 supergiant) with low projected rotational velocity, so it was possible to obtain a firm upper limit on the dipolar magnetic field. The Hα profiles show some signs of variability. Thirty-three independent observations of 19 Cep were acquired over 10 nights between 2006 and 2010. The smallest nightly longitudinal field error bar calculated from these data is 17 G, and the derived dipolar field strength upper limit is 75 G.

4.7.12 λ Cep

The hot (O6) supergiant λ Cep is a runaway (e.g. Gies and Bolton 1986) with a high value of $v \sin i$ and relatively short-period DACs [Kaper et al., 1996]. Extensive time coverage leads to good magnetic constraints, despite the fast rotation. This star is also believed to harbour NRPs (e.g. de Jong et al. 1999). Strong variations of the Hα

profile are observed. Twenty-six independent observations of λ Cep were acquired over 26 nights between 2006 and 2012. The smallest nightly longitudinal field error bar calculated from these data is 57 G, and the derived dipolar field strength upper limit is 136 G.

4.7.13 10 Lac

Hosting weaker (but detectable) wind variations [Kaper et al., 1996], 10 Lac is a sharp-lined O9 dwarf, leading to exceptionally tight limits on the field strength. No Hα variations are detected in our data. Thirty-six independent observations of 10 Lac were acquired over 18 nights in December 2006, September-October-November 2007 and July 2008. The smallest nightly longitudinal field error bar calculated from these data is 4 G, and the derived dipolar field strength upper limit is 23 G, both of which are the best constraints obtained for any star in this sample.

4.8 Discussion and Conclusions

As shown in the previous sections, no large-scale dipolar magnetic field is detected in any of the 13 stars of this sample. However, in order to draw conclusions on whether such fields could be the cause for DACs, it is important to investigate the different possible interactions between weak, potentially undetected magnetic fields and stellar winds.

One form of interaction that has been increasingly investigated in the past years is magnetic wind confinement. Indeed, the magnetic field can channel the wind and closed loops can effectively "confine" it, leading to material trapped in a magnetosphere of closed magnetic loops. ud-Doula and Owocki [2002] introduce the following

"wind confinement" parameter to characterize this interaction:

$$\eta_* = \frac{{B_{eq}}^2 {R_*}^2}{\dot{M} v_\infty} \tag{4.1}$$

where B_{eq} corresponds to the strength of the magnetic field at the equator (which equals half of the dipole polar field strength, B_d), R_* is the stellar radius, $\dot{M}$ is the mass-loss rate and v_∞ is the terminal velocity of the wind. In effect, this parameter corresponds to the ratio of the magnetic field energy density and the wind kinetic energy density at the stellar surface; therefore, its value gives a sense of which of the two dominates. If $\eta_* << 1$, then the wind's momentum causes the magnetic field lines to stretch out radially and the outflow is essentially unperturbed. On the other hand, if $\eta_* >> 1$, then the strong magnetic field lines are perpendicular to the outflow at the star's magnetic equator, barring the passage of charged material. Depending on the rotational parameters of the star, this can lead either to a centrifugal or a dynamical magnetosphere (for a detailed description of both these cases, see Petit et al. 2013).

In intermediate cases however, the effect of the magnetic field can be somewhat more subtle. An in-depth analysis of this regime is presented by ud-Doula and Owocki [2002] and leads to two main thresholds:

- for $\eta_* > 1$, the wind is considered to be confined by the magnetic field;
- for $0.1 < \eta_* < 1$, the wind is not confined, but its flow is significantly affected by the magnetic field.

Therefore, we will consider that for $\eta_* < 0.1$, the dynamical effect of the magnetic field on the wind is likely to be too weak to cause DACs. An upper limit on the

value of the η_* parameter was computed for each star of the sample ($\eta_{*,\max}$) using the upper limit on B_d derived from the Bayesian inference, and the results are presented in Table 4.2.

It should be noted here that the wind parameter values used to compute these η_* upper limits are determined empirically. For magnetic stars, it is necessary to use theoretical mass-loss rates instead of observed values to represent the net surface driving force, since a significant part of the outflow can be confined by the magnetic field, and would then not be detected at larger radii [Petit et al., 2013]. However, in the case of apparently non-magnetic stars, the picture is not so clear. Furthermore, our empirical values are found to be systematically comparable to or smaller than theoretical values; since we are deriving conservative constraints, it seemed more consistent to use the overall smaller empirical values. Finally, while it might be argued that there are important uncertainties associated with empirical determinations of wind parameters, theoretical prescriptions (such as Vink et al. 2001) propagate the rather sizeable uncertainties on masses and luminosities, so there is no obvious reason to choose one over the other based on such an argument.

The value of $\eta_{*,\max}$ ranges between 0.072 and 5.75, with one star below a value of 0.1 (10 Lac) and a majority of the stars below a value of 1 (9/13). As for the stars with $\eta_{*,\max} > 1$, they all have very high projected rotational velocities, thus making it difficult to tightly constrain the field strength. These results are also illustrated in Fig. 4.5, where the x-axis corresponds loosely to the wind kinetic energy density and the y-axis corresponds to the magnetic energy density. The dashed lines represent our two chosen thresholds. Given the fact that the represented values all correspond to upper limits, we can infer that at least a few of these stars do not have magnetic

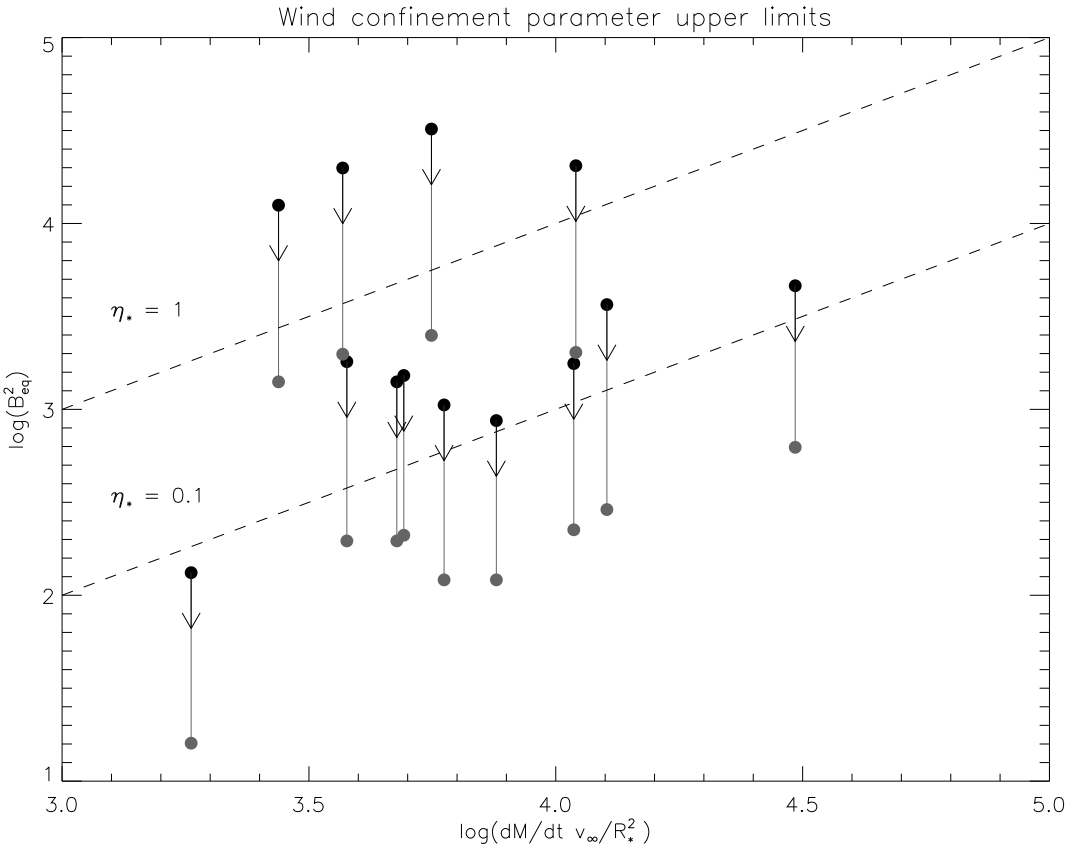

Figure 4.5: Comparison of the magnetic field energy density upper limits (vertical axis, 95.4% confidence interval upper limits indicated by black points, 68.3% confidence interval upper limits indicated by grey points) and the wind kinetic energy density values (horizontal axis) for all 13 stars of this study. Dashed lines show where $\eta_* = 1$ and $\eta_* = 0.1$. For most stars, the likelihood is greater than 95.4% that η_* is below 1, and greater than 68.3% that it is below 0.1.

fields strong enough to dynamically affect the wind outflow on the equatorial plane (as also evidenced by the 68.3% confidence interval upper limits).

In addition to the upper limits, we use the PDFs to assess the sample's distribution of confinement, assuming that each star contributes probabilistically to various field strength bins according to its normalized probability density function (constructing, in other words, a "probabilistic histogram" of field strengths). In this way, we account for both the most probable field strength as well as the large-field tail of the distributions. The top panel of Fig. 4.6 shows this global cumulative PDF for the wind confinement parameter. We expect any star selected from the sample to have $\eta_* < 0.02$ (which is well below the threshold of $\eta_* = 0.1$) with a probability of 50%, or in other words, we expect half of the sample to have a confinement parameter value below 0.02. Using this cumulative PDF, we can also calculate that 75.6% of the sample should have $\eta_* < 0.1$ and 93.9% of the sample should have $\eta_* < 1$. Assuming this small sample is representative of the larger population of stars displaying DACs, this implies that there is no significant dipolar magnetic dynamic influence on the wind for most of these stars. Under these conditions, wind confinement by a dipolar magnetic field does not seem to be a viable mechanism to produce DAC-like variations in all stars.

The derived values of η_* are sensitive to uncertainties in the values of R_*, $\dot{M}$ and v_∞. While the last parameter is essentially identical in all studies, in some extreme cases values of R_* can be up to 2-2.5 times larger than the adopted values, whereas $\dot{M}$ can be up to 10 times larger. Such differences would result respectively in a 6-fold increase and a 10-fold decrease in the inferred value of η_*. However, studies that infer larger stellar radii also tend to infer larger mass loss rates (e.g. Markova et al. 2004,

with ξ Per and HD 34656). Thus one effect approximately offsets the other. The largest potential increase in inferred η_* for a star of our sample would occur for α Cam; based on the values measured by Najarro et al. [2011] (about 1.5 times increase in radius, and half the mass-loss rate), we obtain an increase of η_* by a factor of 4. However, for typical combinations of R_* and $\dot{M}$ obtained from other studies, we obtain values of η_* that are either comparable in magnitude, or smaller (up to an order of magnitude) than those inferred using the adopted parameters.

Do these results rule out dipolar fields altogether? Cranmer and Owocki [1996] simply introduce bright spots on the surface of the star, with no particular attention to the mechanism creating these. While wind confinement is possibly the most obvious effect of a magnetic field on the ouflowing material driven from the surface of a massive star, there might also be more subtle interactions. For instance, the magnetic pressure at the poles of a weak large-scale dipolar field could lower the local gas pressure, thus reducing the gas density and leading to a lower optical depth. Hence, light coming from the pole would actually probe hotter regions within the star. This could cause bright spots like those in the Cranmer and Owocki [1996] model. Making a few assumptions (closely modeled on the calculations of Sundqvist et al. 2013), we can derive a simplified formula for the magnetic field (B) required to produce a given brightness enhancement. Indeed, if we consider a flux tube at the photosphere, we can compare a zone outside of the tube ($B = 0$) to a zone inside the tube ($B = B_{\rm T}$). Furthermore, we assume a grey atmosphere:

$$T(\tau) = T_{\rm eff} \left(\frac{3}{4}\tau + \frac{1}{2} \right)^{\frac{1}{4}} \tag{4.2}$$

where T is the temperature and $T_{\rm eff}$ is the effective temperature (corresponding to an

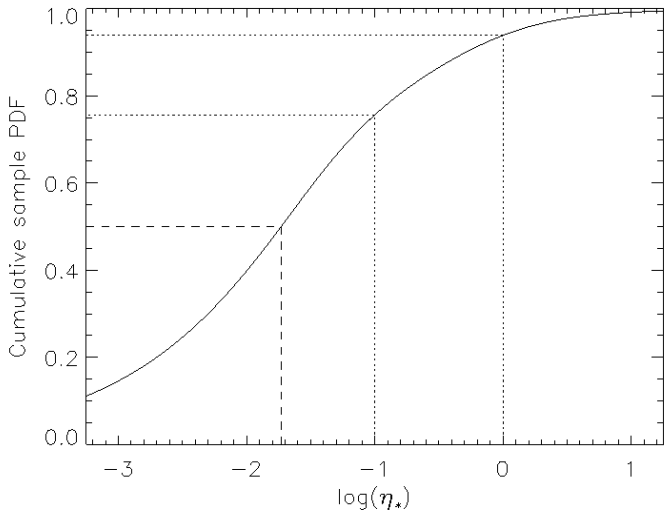

(a) η_* cumulative PDF.

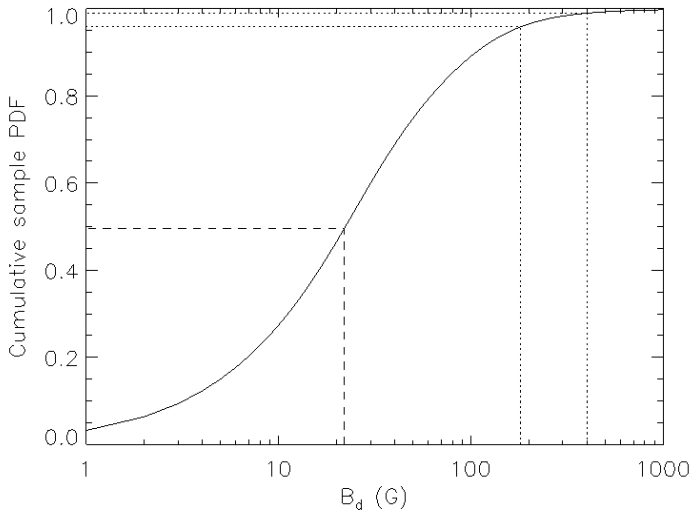

(b) B_d cumulative PDF.

Figure 4.6: Cumulative PDFs of the total sample for η_* (top) and B_d (bottom). In both cases, the dashed line shows the 50% confidence interval upper limit. For the top panel the dotted lines represent, from left to right, $\eta_* = 0.1$ and $\eta_* = 1$. For the bottom panel the dotted lines represent, from left to right, the field strength required to produce a 10% and a 50% brightness enhancement (resp. about 180 G and 400 G).

optical depth, τ, of 2/3). At equilibrium, the gas pressures ($P_{\rm g}$) inside and outside the tube only differ by the value of the magnetic pressure ($P_{\rm B} = \frac{B^2}{8\pi}$):

$$P_{\rm g}(r) = P'_{\rm g}(r) + P_{\rm B} \tag{4.3}$$

where primed variables refer to values inside the flux tube, by opposition to unprimed variables which refer to values outside the flux tube. The optical depth can be written as a function of gas pressure:

$$\tau = \frac{\kappa P_{\rm g}}{g} \tag{4.4}$$

where κ is the mean Rosseland opacity, and g is the surface gravity. To determine the brightness enhancement, we need to find the temperature corresponding to an optical depth of 2/3 inside the flux tube (assuming magneto-hydrostatic and temperature equilibrium at a given vertical depth):

$$T(\tau' = 2/3) = T_{\rm eff}\left(1 + \frac{3\kappa B^2}{32\pi g}\right)^{\frac{1}{4}} \tag{4.5}$$

Finally, since the flux is proportional to the fourth power of the temperature, the brightness enhancement can be expressed as:

$$\frac{F'}{F} = 1 + \frac{3\kappa B^2}{32\pi g} \tag{4.6}$$

Now, using typical values for O dwarfs ($\kappa \sim 1$ and $\log g = 4.0$), it is very simple to perform sample calculations. For instance, the main model used by Cranmer and Owocki [1996] uses a 50% enhancement. The field required to produce such an enhancement is of the order of 400 G, assuming a magnetic region surrounded by

an adjacent non-magnetic region. On the other hand, the same paper shows that DAC-like behaviour can arise with an enhancement as small as 10%. The associated field would be of the order of 180 G[2]. The dipolar field upper limits shown in Table 4.2 are almost all (9/13) under that value. While models with smaller brightness enhancements are not tested in their study, this mechanism associated with dipolar magnetic fields does not provide a viable way of producing DACs given the observational constraints obtained in this study.

Once again, in very much the same way as we did for η_*, we can compile a global cumulative PDF for B_d (bottom panel of Fig. 4.6). The results are quite telling: 50% of the sample should have $B_d < 23$ G, and 95.8% (99.0%) of the sample should have a smaller dipolar field strength value than that required to produce a 10% (50%) local brightness enhancement.

Even if dipolar fields seem to be an unlikely cause for DACs, the general case for magnetism is not settled. Indeed, structured small-scale magnetic fields could arise as a consequence of the subsurface convection zone caused by the iron opacity bump at $T \simeq 150$kK [Cantiello and Braithwaite, 2011]. Then, magnetic spots at the surface of the star could possibly give rise to CIRs (e.g. Henrichs and Sudnik 2014), even though they are expected to be relatively weak (to have a surface field of at least 160 G, we need a 40+ $M_\odot$ star). While the detection of such fields is an arduous task [Kochukhov and Sudnik, 2013], proving their existence and understanding their structure might hold the key to this old problem, as well as other similar problems (e.g. in BA supergiants, see Shultz et al. 2014). Good candidates for follow-up deep magnetometry might be ϵ Ori and 10 Lac. The former has the advantage of being

[2]It is likely, given that dipole fields correspond to a continuous distribution of magnetic field (rather than isolated flux tubes as assumed in this calculation), that even stronger polar fields would actually be necessary to achieve a given brightness enhancement.

very bright and having a relatively low value of $v \sin i$, while the latter has very low projected rotational velocity (for an O star). 10 Lac already has decent time coverage, but could benefit from obtaining more observations per night.

In parallel to observational efforts, theoretical investigations are required in order to probe the parameter space of magnetic field strengths and configurations to find out which types of fields can give rise to DAC-like phenomena. Numerical simulations can also be used to investigate mechanisms other than magnetism, as well as constrain the required brightness enhancement in a Cranmer and Owocki [1996] model analog to create CIRs in the first place.

The next paper of this series will explore the magnetic spot hypothesis and hopefully place constraints on how likely such a mechanism is to cause DACs.

4.9 Acknowledgments

This research has made use of the SIMBAD database operated at CDS, Strasbourg, France and NASA's Astrophysics Data System (ADS) Bibliographic Services.

ADU gratefully acknowledges the support of the *Fonds québécois de la recherche sur la nature et les technologies*. GAW is supported by an NSERC Discovery Grant. AuD acknowledges support from the NASA Chandra theory grant to Penn State Worthington Scranton and NASA ATP Grant NNX11AC40G.

Finally, the authors thank the anonymous referee for his insightful comments which have no doubt contributed to making this paper better.

Chapter 5

Hydrodynamic models and radiative transfer

5.1 Hydrodynamic modelling of hot star winds using the VH-1 code

The winds of massive stars consist of outflowing plasmas, and as such their motions can be understood using the laws of hydrodynamics. Therefore, if we want to model numerically the behaviour of a stellar wind under certain circumstances, we must take these laws into account.

The *Virginia Hydrodynamics* code (VH-1) is a publicly available multi-dimensional hydrodynamics platform which runs on FORTRAN. It implements the "piecewise parabolic method" developed by Colella and Woodward [1984] (and refined by Blondin and Lufkin 1993) to solve Euler's equations:

$$\frac{\partial \rho}{\partial t} + \mathbf{u} \cdot \nabla \rho + \rho \nabla \cdot \mathbf{u} = 0 \tag{5.1}$$

$$\frac{\partial \mathbf{u}}{\partial t} + \mathbf{u} \cdot \nabla \mathbf{u} + \frac{\nabla p}{\rho} = \mathbf{g} \tag{5.2}$$

$$\frac{\partial e}{\partial t} + \mathbf{u} \cdot \nabla e + \frac{p \nabla \cdot \mathbf{u}}{\rho} = 0 \tag{5.3}$$

where ρ is the density, t is time, $\mathbf{u}$ is the flow velocity vector, p is the pressure, g is acceleration and e is the internal energy density. It should be noted that these equations correspond to a special case of the Navier-Stokes equations applied to adiabatic flows in the absence of viscosity.

However, to model the winds of hot stars, it is also necessary to compute the radiation force. This force is computed in a way similar to that described in Chapter 2, except rather than taking into account a point star, it must take into account a finite disk. This is particularly important to model CIRs since as the enhanced material leaves the star, the spot which launched it appears smaller with time, and the force must take into account the intensity from each point on the stellar disk. To do so, a number of integration rays are defined. That number cannot be too large, because each integration along a ray is computationally expensive, but it must be sufficient to resolve any surface brightness inhomogeneities. Further discussion about ray selection is included in Chapter 6.

5.2 Radiative transfer

In its differential form, the (unpolarized) radiative transfer equation (RTE) can be written as:

$$\frac{dI_\lambda}{d\tau_\lambda} = -I_\lambda + S_\lambda \tag{5.4}$$

with

$$d\tau_\lambda = \kappa_\lambda \rho ds \tag{5.5}$$

where I_λ is the wavelength-dependent intensity, τ_λ is the optical depth, κ_λ is the opacity, ρ is density, ds is a line element and S_λ is the *source function*, which determines the contribution of emission. Assuming an exponential form for the intensity, we obtain the following *formal* solution (e.g., Gray 2005):

$$I_\lambda(\tau_\lambda) = \int_0^{\tau_\lambda} S_\lambda(\tau_\lambda) \mathrm{e}^{-(\tau_\lambda - t_\lambda)} dt_\lambda + I_{\lambda,0} \mathrm{e}^{-\tau_\lambda} \tag{5.6}$$

where $I_{\lambda,0} = I_\lambda(\tau_\lambda = 0)$.

In order to solve for the emergent intensity of a given ray, these quantities must be computed at every point along its path, unless certain simplifying assumptions are made. In particular, it is important to determine what the source function is. If there is local thermal equilibrium (LTE), the source function is simply given by Planck's law.

5.3 Photospheric line formation

There are a number of mechanisms at play in the formation of a spectral line. Some lines, such as wind lines, include effects such as scattering (this will be covered in the next section), but on the other hand, the most simple lines that can be studied are unsaturated[1], photospheric metallic lines. They are purely formed by absorption at the stellar surface, simplifying the solution of the RTE tremendously. In such a case, the profile can be constructed by taking into account different sources of

[1]This means that none of the local profiles (which will be covered in the following paragraph) exhibit absorption that is strong enough to decrease the intensity to zero at any wavelength.

broadening, which allow us to model the various velocity fields that exist at the stellar surface. Furthermore, the shapes of these lines are particularly simple when they are not affected by saturation, and since we consider metallic lines, they do not include some of the effects that can affect hydrogen and helium lines, such as Stark broadening. Nonetheless, they still exhibit various other sources of broadening which we will review summarily in this section (and will be particularly relevant to some of the results presented in Chapter 7).

5.3.1 Local profiles and thermal broadening

First, we can define *local* profiles for each point on the stellar disk. To do so, we must consider the effect of thermal broadening. While at a given point, the surface velocity due to rotation should be defined uniquely, the thermal velocity distribution of the various species is given by [Gray, 2005]:

$$\frac{\mathrm{d}N}{N} = \frac{1}{\pi^{1/2} v_0} \mathrm{e}^{-(v_\mathrm{R}/v_0)^2} \mathrm{d}v_\mathrm{R} \tag{5.7}$$

where v_R is the radial velocity and v_0^2 is the variance and is given by:

$$v_0^2 = 2kT/m \tag{5.8}$$

with k being Boltzmann's constant and m is the mass of the atom which is considered. Therefore, if the disk element is at a line-of-sight rotational velocity is given by v_z, the local absorption profile as a function of velocity ($A_\mathrm{local}(v)$) can be calculated as:

$$A_\mathrm{local}(v) = k\mathrm{e}^{-(v-v_z)^2/v_0^2} \tag{5.9}$$

where k is a constant related to the line strength.

5.3.2 Microturbulence and macroturbulence

In massive stars, thermal broadening is not sufficient to explain the line shapes. In fact, there seems to be evidence for the presence of turbulent motions at the surface of these stars (e.g., Rosseland 1928). This additional velocity field occurs at various scales, and is typically defined with respect to two extreme regimes: *microturbulence*, which refers to motions occurring on scales much smaller than unit optical depth, and *macroturbulence*, which refers to the case where they occur on scales much larger than unit optical depth. In the first case, the turbulent contribution acts in a similar way to the thermal broadening and can be treated almost identically introducing the microturbulent parameter ξ; we rewrite the local absorption profile[2] as:

$$A_{\rm local}(v) = \kappa {\rm e}^{-(v-v_z)^2/(v_0^2+\xi^2)} \tag{5.10}$$

In the case of macroturbulence, it cannot be treated locally and, instead, is often treated by convolving the disk-integrated profile with the (generally assumed Gaussian) velocity distribution. It should be noted that macroturbulence is particularly prevalent in OB supergiants.

As to the origin of these velocity fields, there is no consensus, but there are leading hypotheses. Microturbulence is thought to arise from convective motions due to the iron opacity bump [Cantiello et al., 2009]. That scenario might also explain macroturbulence, especially since it appears to be inhibited in the presence of an

[2]Here, we calculate the absorption profile such that the continuum-normalized local intensity profile, $I_{\rm local}(v)/I_c$ is equal to $1 - A_{\rm local}(v)$ to avoid having to calculate the actual flux at the central wavelength. This approximation is sufficient to reproduce well-behaved unsaturated photospheric lines.

extreme magnetic field which can stabilize the atmosphere all the way down to the FeCZ (as is the case for NGC 1624-2, Sundqvist et al. 2013), but there are also some indications that pulsations might have a role[3] [Simón-Díaz et al., 2011].

5.3.3 Disk integration and rotational broadening

Finally, to obtain the total absorption profile, we must integrate all the local profiles over the entire disk. Each profile is weighted by the projected area of the surface element from which it emanates as well as the local limb darkening factor (these details are discussed in further detail in Sect. 7.3). If there are any brightness variations across the surface, they must also be taken into account in the weighting. This is where rotational broadening becomes apparent: the change in the central velocity v_z of the local profiles across the disk is typically significantly larger than v_0, ξ and the macroturbulent velocity, making rotation the most important source of broadening for most massive stars.

The normalized total intensity profile is then computed by subtracting the total absorption profile from unity. Once again, this only holds for cases where the line is "well-behaved", meaning that it is not saturated, and there are no other contributions such as emission or scattering.

5.4 Scattering and wind-sensitive lines

Another case to consider is that of UV resonance lines which inform us about the stellar wind. Indeed, they are formed essentially purely by line scattering, the very same process that drives the stellar wind in the first place in the case of massive

[3]These two scenarios are not mutually exclusive since the FeCZ might excite pulsational modes in massive stars.

stars (as seen in Chapter 2). Then, if we consider the simplest case of a non-rotating, spherically symmetric wind, two important assumptions can be made. Firstly, the source function can be evaluated by considering that the "absorption" (i.e., the incoming intensity that is being scattered) is equal to the isotropic "emission" (i.e., the outgoing scattered light), therefore:

$$S_\lambda = \frac{1}{4\pi} \oint I_\lambda d\omega \tag{5.11}$$

where $d\omega$ is an element of solid angle. The other simplifying assumption that can be made has already been mentioned previously: the Sobolev approximation. Since the velocities to which the wind is accelerated are much greater than the thermal velocity, photons at a specific wavelength will be scattered in a specific region of the wind. Then, calculating the intensity at that wavelength for a given ray becomes much simpler, since only that region must be considered. This is illustrated in Fig. 5.1.

Qualitatively, this leads to a specific type of line profile known as a *P Cygni profile*, named after the prototypical LBV P Cygni, which was the first star to have some of its spectral lines interpreted as resulting from an expending envelope [McCrea, 1929, Beals, 1929, 1932]. It can be understood as the combination of an absorption profile, due to scattering of photons *out of* the line of sight in front of the star (from the point of view of the observer), and an emission profile, due to scattering of photons *into* the line of sight in the entire wind. This is illustrated in Fig. 5.2.

In order to compute P Cygni profiles numerically to model observed lines, and to include additional effects (e.g., structure in the wind), Sobolev Exact Integration (SEI; Lamers et al. 1987) can be used. It uses the Sobolev approximation formalism to compute the source function, but performs the full radiative transfer integration.

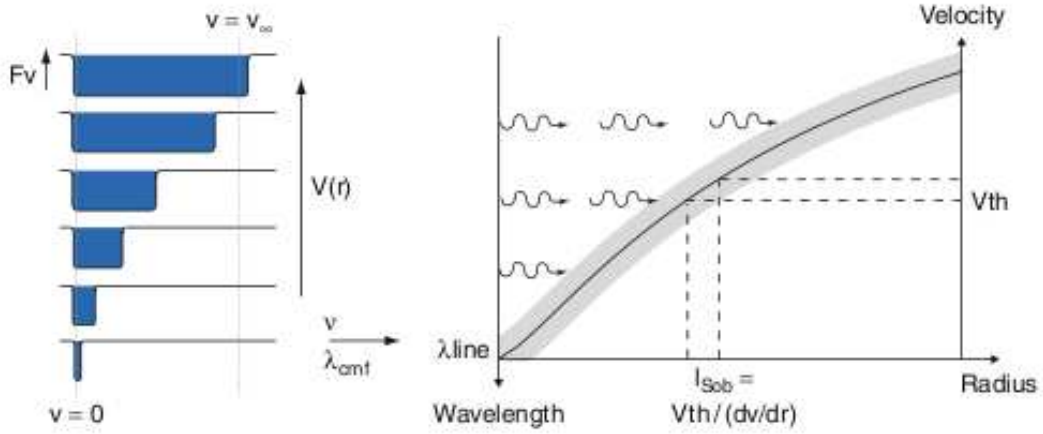

Figure 5.1: Cartoon showing how photons with a specific wavelength are scattered in a specific region of the wind in the Sobolev approximation; taken from Owocki [2013]. As the wind is accelerated monotonically outwards, photons originating from the stellar surface seem increasingly redshifted in its reference frame, therefore it absorbs increasingly bluer photons. Reproduced with permission of Springer.

This method is used to perform calculations in Chapter 6.

5.5 Optical photometry

While the previous sections focussed on line formation, some phenomena, such as pulsations and temperature or brightness variations across the stellar surface, can also affect the continuum flux of a star. They can be investigated using broadband photometry and information is obtained by analysis in the time domain.

The Microvariability and Oscillations of STars (*MOST*) telescope is a Canadian high-precision optical broadband photometer in space [Walker et al., 2003]. While rather modest (150mm aperture; roughly 6 times smaller than Kepler's), its photometric precision per 101-minute orbit can be comparable to that of Kepler (sub-mmag precision), albeit in a different magnitude range. Its custom broadband filter has a

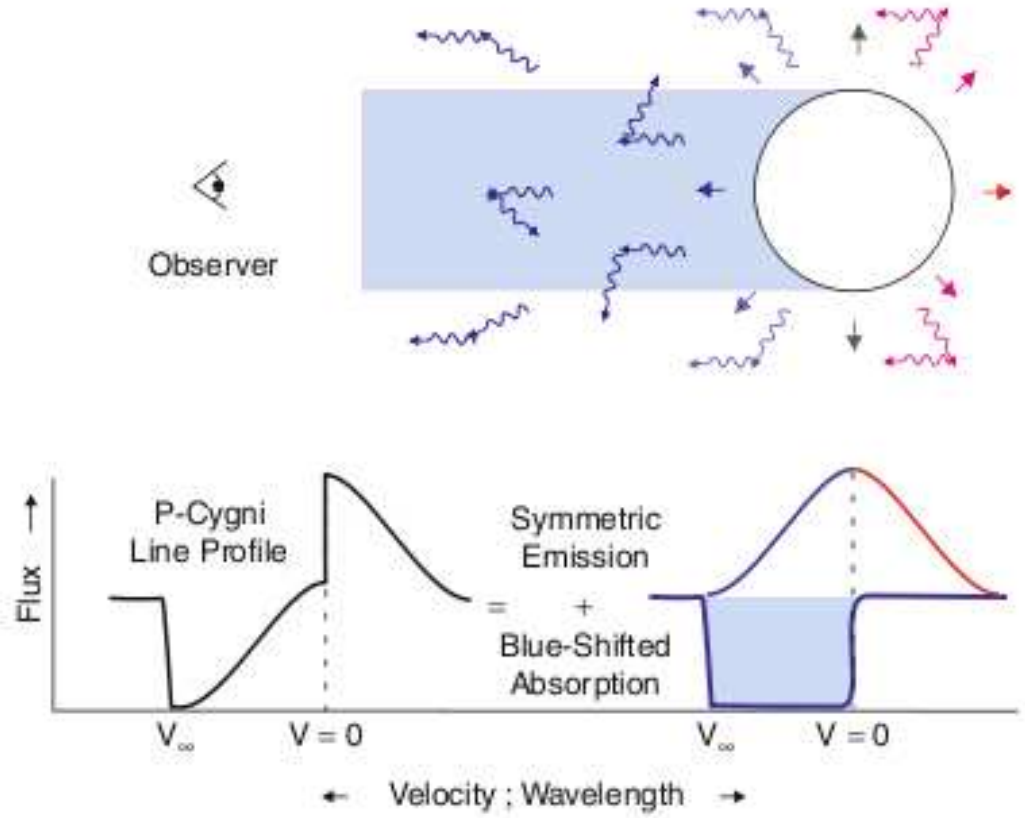

Figure 5.2: Cartoon from Owocki [2013] showing how a P Cygni profile is formed: photons scattered out of the line of sight in front of the star lead to blue-shifted absorption, while photons scattered into the line of sight in the entire wind lead to symmetric emission; together, these two contributions make up the characteristic shape of the P Cygni profile. Reproduced with permission of Springer.

bandpass of about 3000 Å which is centered at 5250 Å. Since it is on a polar, Sun-synchronous orbit, one of the main advantages of *MOST* is that it can be used to observe a star over a long period of time, up to a few months. This has allowed the investigation of variability on a large range of timescales, since the typical observing cadence is of order a minute. It has been used for a variety of science cases, from asteroseismology to exoplanet detection, and on a variety of stars across the H-R

diagram[4].

The Bright Target Explorer (*BRITE-Constellation*; Weiss et al. 2014) is an international collaboration involving Austria, Poland and Canada, and currently consists of a "constellation" of 5 functioning nanosatellites (20cm × 20cm × 20cm). The aperture size is 30mm, which means that to obtain precise photometry, it must observe very bright stars (hence its name). As such, it focuses on stars with V magnitudes smaller than 4; within this range, it can achieve millimagnitude precision for each observed datapoint. This sample also happens to be biased towards earlier spectral types as bright stars tend to be inherently massive (nearly one half of the sample consists of OBA stars; Neiner and Lèbre 2014). Some of the main new features which constitute improvements on what MOST can achieve are the observing timeframe (*BRITE* can observe a target for nearly six continuous months since it operates 5 satellites) and the blue and red filters (3 of the functioning telescopes have a red filter, and 2 have a blue filter).

[4]A few science highlights of the *MOST* mission include the non-detection of pulsations in Procyon (F5 IV-V; Matthews et al. 2004), the discovery of g-modes in HD 163899 (B2 Ib/II; Saio et al. 2006) and the confirmation of the existence of 55 Cancri e (which orbits a G8 V star; Winn et al. 2011).

Chapter 6

Paper II: Modelling Co-rotating Interaction Regions using realistic spots

Paper Title[1]: "Investigating the origin of cyclical wind variability in hot, massive stars - II. Hydrodynamical simulations of co-rotating interaction regions using realistic spot parameters for the O giant ξ Persei"

[1]This chapter contains a version of a paper currently in preparation and shortly to be submitted to Monthly Notices of the Royal Astronomical Society as: A. David-Uraz, S.P. Owocki, G.A. Wade and J.O. Sundqvist.

6.1 Abstract

OB stars exhibit various types of spectral variability historically associated with wind structures, including the apparently ubiquitous discrete absorption components (DACs). These features are thought to be caused either by magnetic fields or non-radial pulsations. In the second paper of this series, we revisit the canonical phenomenological model [Cranmer and Owocki, 1996] used to explain the formation of DACs by taking into account modern observations and more realistic theoretical predictions.

Using constraints on putative bright spots located on the surface of the massive O giant ξ Persei derived from high-precision space-based broadband optical photometry obtained with the Microvariability and Oscillations of STars (*MOST*) space telescope, we generate two-dimensional hydrodynamical simulations of co-rotating interaction regions in its wind. We then compute synthetic ultraviolet (UV) resonance line profiles using Sobolev Exact Integration and compare them with historical timeseries obtained by the International Ultraviolet Explorer (*IUE*) to evaluate if the behaviour of ξ Persei's DACs is reproduced. Testing three different models of spot size and strength, we find that the classical pattern of variability can be successfully reproduced for all three models, with quantitative differences arising between each model. Furthermore, we test the effect of the radial dependence of ionization levels on line driving. While including the effect of ionization helps enhance the absorption closer to the stellar surface, the nearly saturated absorption of UV resonance lines at low velocity does not allow us to conclusively assess the importance of this factor.

6.2 Introduction

OB stars are known to host various types of wind variability. Most notably, "discrete absorption components" (DACs), thought to be ubiquitous [Howarth and Prinja, 1989] and observed to migrate through the velocity space of UV resonance lines, are believed to stem from the presence of large-scale azimuthal density structures in the wind (called "co-rotating interaction regions", or CIRs; Mullan 1986). The physical origin of these structures is unknown, although the two main hypotheses involve magnetic fields and non-radial pulsations (NRPs). However, both scenarios encounter a number of difficulties. Indeed, less than 10% of massive stars harbour detectable magnetic fields [Wade et al., 2014] and those that do usually exhibit large-scale dipolar fields, which can not be responsible for DACs in general [David-Uraz et al., 2014]. On the other hand, the timescales related to DACs are hard to reconcile with typical NRP periods [de Jong et al., 1999].

Some understanding of the formation of CIRs and DACs can be gained from the phenomenological model developed by Cranmer and Owocki 1996 (henceforth referred to as the "CO96 model"). Making no physical assumptions about their origin or formation, it uses *ad hoc* bright spots on the photosphere to drive a locally enhanced outflow, which then leads to rotationally modulated wind structures. While this model has been generally accepted for the past 20 years, it has not since been revisited to include newly-derived observational constraints[2].

[2]Some more sophisticated hydrodynamical simulations have been performed since the original CO96 paper, including a third dimension as well as slightly more detailed physics (e.g., Dessart 2004, which notably concluded that the CO96 2D approach was valid to derive the effect of the wind structures on the UV line profiles). However, these studies still used unrealistic spot parameters with respect to the constraints described in the following subsection.

6.2.1 Observational constraints

While most of this work has stemmed from the observation of variability in the UV spectra of hot massive stars, there are various observational diagnostics which are increasingly believed to be related to the presence of co-rotating bright spots on their surfaces, as well as the extended wind structures which result from their presence. For instance, DACs have been shown to correlate with variability in Hα [Kaper et al., 1997] as well as variability in excited state lines [Massa and Prinja, 2015]. However, in this paper we will focus mostly on the classical DACs seen in UV resonance lines, as well as broadband optical photometry.

UV spectroscopic timeseries

The most important observational constraint in understanding CIRs comes from time-series of UV resonance lines obtained by the International Ultraviolet Explorer (*IUE*; e.g., Prinja and Howarth 1986, Kaper et al. 1996, 1997). In particular, a number of deductions can be made which support the CO96 model. Perhaps the key point in that regard is the fact that the DAC recurrence timescales seem to correlate with the projected rotational velocity ($v \sin i$), suggesting that they are rotationally modulated [Prinja, 1988]. Furthermore, there are a number of DAC properties that can help constrain the conditions in the wind: their maximum depth, the range of velocities that they span, as well as their overall morphology. A successful model should allow us to reproduce all of these properties.

Various observations concur that DACs must be formed at low velocities, and therefore that the related structures must form on, or very near the stellar surface, suggesting that the surface perturbations causing them must occupy a significant

portion of the stellar disk (e.g., Fullerton et al. 1997, Massa and Prinja 2015).

Photometric signatures of co-rotating bright spots

Photometric signatures related to CIRs have been claimed to be found in a number of WR stars, e.g., WR110 [Chené et al., 2011] and WR113 [David-Uraz et al., 2012]. Typically, they involve light curves with seemingly stochastic variations, but time-frequency analysis reveals the presence of multiples of the inferred rotational frequency, appearing and disappearing depending on the number of structures in the wind at any given time.

Ramiaramanantsoa et al. [2014] claim to have made the first detection of photometric variations due to co-rotating bright spots on the surface of an OB star using broadband optical photometry from the *MOST* space telescope. The star in question, ξ Persei, is an O7.5III(n)((f)) star which was observed by *IUE* for 5 runs between 1987 and 1994 and shown to have well-defined DACs. The most important constraint derived in the study of ξ Persei's light curve is that the maximum amplitude of the variations produced by the bright spots is about 10 mmag, or about 1% of the apparent brightness. This sets important limits on both the size and brightness of the spots. The main CO96 model involved spots with a 20° angular radius and a gaussian brightness enhancement which peaked at a 50% central brightness contrast. Such spots would generate light curve variations with an amplitude roughly 6 times larger than observed.

The goal of this paper is to couple the recent (optical) photometric and (UV) spectroscopic observational diagnostics using a CO96-type phenomenological model.

Specifically, using the constraints derived photometrically to choose our input parameters, we aim to determine whether it is possible to reproduce, at least qualitatively, the behaviour exhibited by the UV resonance lines of ξ Persei. The numerical methods used to generate both the hydrodynamical wind simulations and to compute synthetic line profiles are detailed in Sect. 7.3. In Sect. 6.4, we then describe the obtained results and compare them to the observational diagnostics. Finally, in Sect. 7.6 we draw conclusions and indicate the next steps toward a better understanding of this phenomenon.

6.3 Numerical methods

This section provides a detailed account of the numerical methods used in this study.

6.3.1 Hydrodynamical wind modelling

The wind is modelled in 2D in the equatorial plane using VH-1, a multidimensional ideal compressible hydrodynamics code written in FORTRAN which uses the piecewise parabolic method (PPM) algorithm developed by Colella and Woodward [1984]. However, the key factor in forming CIRs is the variation in the line-driving force due to inhomogeneities on the surface of the star. Cranmer and Owocki [1995] have shown how to compute the vector line force for such a flux distribution (specifically in the context of an oblate finite disk; OFD). Therefore, using a FORTRAN subroutine (*gcak3d*) implementing this method together with VH-1, we can perform a full radiation hydrodynamics calculation of the wind (at this time we only compute the radial component of the line driving force). However, rather than implementing an

OFD, we implement Gaussian bright spots on the equator. Their "amplitude" corresponds to the maximum enhancement at the peak of the distribution (the central flux divided by the unperturbed flux) and their "angular radius" corresponds to the standard deviation of the Gaussian distribution multiplied by a factor of $\sqrt{2}$. Using both the size and amplitude of the spots, we can infer the amplitude of the variation a single spot would cause in the integrated light profile.

Using θ as the angle between the surface normal and the line of sight at a given point on the stellar surface and considering the maximum flux due to the addition of a gaussian spot in the center of the disk, we can calculate the ratio of the fluxes as a function of the amplitude and radius of the spot using the following constraint:

$$\frac{\int_0^{\pi/2} A\mathrm{e}^{-\theta^2/r^2} \sin\theta\cos\theta d\theta}{\int_0^{\pi/2} \sin\theta\cos\theta d\theta} = A_{\mathrm{var}} \approx A\sin^2 r \tag{6.1}$$

where A_{var} corresponds to the fractional amplitude of the variations in the light curve. For small values of r, this simply reduces to:

$$A_{\mathrm{var}} \approx Ar^2 \tag{6.2}$$

The behaviour of A_{var} as a function of A and r is shown in Fig. 6.1. Using this formula, we can choose sets of values of spot sizes and strengths which correspond to the 10 mmag amplitude found by Ramiaramanantsoa et al. [2014] (or in other words for $A_{\mathrm{var}} = 0.01$); in our case we select three models respecting these constraints, as shown in Table 6.1. We let the spot radius vary between 5° and 20°, which seem like reasonable values since on the one hand, the spots must not be too small since they must cover a significant fraction of the stellar disk, as mentioned previously, but they

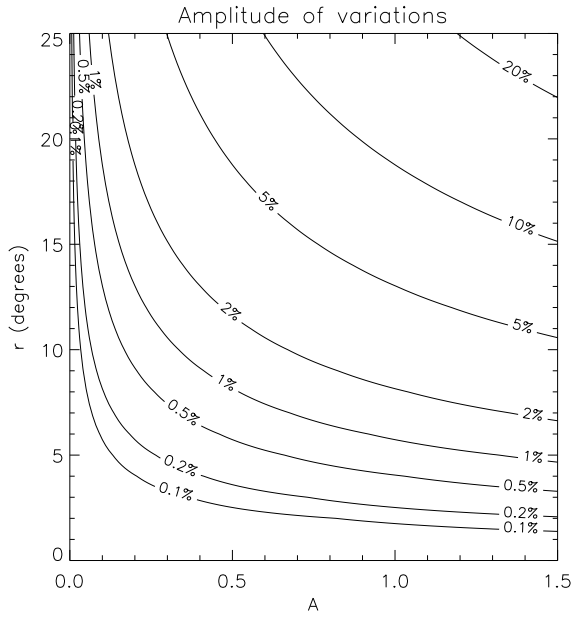

Figure 6.1: Contour plot showing $A_{\rm var}$ as a function of the spot parameters A and r.

also cannot be too large, otherwise the corresponding brightness contrast might be too low to produce noticeable perturbations in the wind (this point will be further discussed in Sect. 7.6).

Another important change in this study, as compared to the CO96 model, is the implementation of the ionization parameter δ, as derived by Abbott [1982]. This allows us to take into account the radial dependence of the ionization levels, which in turn influence the local electron density and therefore the line driving. A higher value of δ leads to a greater driving force, ultimately ejecting too much material from the surface for the radiation to be able to continuously accelerate it outwards, or in other words "overloading" the wind for very high values. Abbott [1982] finds a typical value of $\delta \approx 0.1$ for massive stars. Including this factor helps compensate for the weaker spots and possibly allows to form the CIRs nearer to the stellar surface. Therefore

Table 6.1: List of models used in this study; r corresponds to the angular radius of the spot, A is the central amplitude of the spot flux enhancement and δ is the ionization factor of the wind.

Model	r (°)	A	δ
1A	5	1.32	0
1B	5	1.32	0.1
2A	10	0.33	0
2B	10	0.33	0.1
3A	20	0.08	0
3B	20	0.08	0.1

each of the 3 spot models described above is also divided into a sub-model which does not take the ionization factor into account, and one which does (see Table 6.1 for a short summary of the 6 models).

We model a 90 degree sector of the equatorial plane, using 90 azimuthal zones and 250 radial zones. The radial zones are spaced geometrically, each zone being 2% larger than the previous one, and they span a region extending from the stellar surface ($R = \mathrm{R}_*$) to 10 stellar radii ($R = 10\ \mathrm{R}_*$). The azimuthal boundary conditions are periodic, such that we are actually modelling 4 identical and equally spaced equatorial bright spots[3]. In order to properly resolve the surface and to account for the additional driving provided by even the smallest spots, we set up a numerical quadrature, with rays intersecting the star at various values of p (impact parameter) and ϕ' (azimuathal angles). These points on the star are distributed using a Gauss-Legendre quadrature in p^2 and ϕ', and using a rotation factor between different values of p (as explored in [Kee, 2015]). To start, we run a 1D simulation for 600 ks to obtain

[3]Of course, such a distribution would lead to smaller photometric variations than those caused by a single spot, since there would always be at least one spot visible on the stellar surface, and in general the constraints we are using correspond to lower limits.

Table 6.2: List of parameters used to generate the hydrodynamical models.

Model parameter	Value
Stellar mass M_*	$26M_\odot$
Stellar luminosity L_*	$2.6 \times 10^5 L_\odot$
Stellar radius R_*	$14R_\odot$
Effective temperature $T_{\rm eff}$	35.0 kK
Surface azimuthal velocity $v_{\phi,0}$	2.2×10^7 cm/s
Surface density ρ_0	3.0×10^{-11} g/cm^3
CAK power-law index α	0.6
Collective line force $\bar{Q}$	10^3
Quadrature points in p and ϕ'	9×9
p rotation factor	0.33

a relaxed, spherically-symmetric wind which behaves like a typical line-driven wind, as described by Castor et al. 1975 (henceforth referred to as "CAK theory"). We then use this as input for a 2D simulation, but once again with a uniform surface flux distribution, and relax it for 700 ks. Then, we "turn on" the spots and let the simulation relax for 800 ks. Finally, we compute 7 snapshots which are 10 ks apart (they span a quarter of the rotational period) to trace the temporal variation of the wind. All models use the same input surface parameters, detailed in Table 6.2.

The stellar parameters for ξ Persei are obtained from Repolust et al. [2004] (M_*, L_*) and Krtička and Kubát [2010] (R_* and $T_{\rm eff}$). The surface azimuthal velocity is chosen to be equal to the value of the projected rotational velocity ($v \sin i$) reported by David-Uraz et al. [2014]. On the other hand, the surface density is adjusted to ensure that the wind outflow is initially subsonic as it leaves the stellar surface (otherwise, that would lead to significant instabilities in the simulation). We chose a standard value for the CAK power-law index (e.g., Puls et al. 2000). The line force, $\bar{Q}$, is an important input parameter as it determines the global behaviour of the wind by

calibrating the force of the line-driving mechanism [Gayley, 1995]. A typical value for OB stars was chosen for this parameter, although its exact value does not actually matter, since for this study we are more interested in the structures that form in the wind than in its overall properties.

Finally, the code outputs a 2D grid of density, radial velocity and azimuthal velocity describing the wind in the equatorial plane.

6.3.2 Line profile synthesis

Once the wind models are generated, they must first be extrapolated into a three-dimensional grid in order to perform the line synthesis. We use the same prescription as Cranmer and Owocki 1996 (as described in their Eq. 21), generating 181 latitudinal zones to ensure that grid cells near the equator have comparable sizes in the latitudinal and azimuthal directions. The value of σ used to perform that extrapolation for a given model corresponds to the angular radius of the spot used in that model. We then use Sobolev Exact Integration (SEI, Lamers et al. 1987) to compute the line profile. Our calculation is based on the "3D-SEI" method [Cranmer and Owocki, 1996] and uses the same code as Marcolino et al. [2013].

A few important input parameters are used. First, the resolution depends on the number of velocity bins computed across the entire line profile. We use 161 points for all models, which leads roughly to a 45 km/s resolution for the models without the ionization factor, and a 30 km/s resolution for the models which include the ionization factor. The latter case corresponds to a spectral resolution of $R = c/\Delta v$ of around 10^4, which corresponds to the resolution obtained using the Short Wavelength Prime (SWP) camera on *IUE* [Kaper et al., 1996], therefore facilitating the direct

comparison of our synthetic line profiles to the observed behaviours. We also use a fairly high number of rays (318 radial and 401 azimuthal rays) to perform the integration so as to probe our grid as finely as possible and yield the most precise results. As for the line strength, we use the κ_0 parameter as defined by [Hamann, 1981]. This parameter determines the optical depth and is proportional to the mass-loss rate and the fractional abundance of the absorbing ion for a given line. We chose a value of 1.0, which corresponds to a line of intermediate strength, analogous to the resonance lines used in typical DAC studies (the Si IV doublet). Finally, the non-monotonic velocities induced by phenomena such as Line-Deshadowing Instability [Owocki et al., 1988] can be modelled as a turbulent velocity parameter $v_{\rm turb}$ which is implemented like microturbulence and made to vary between the base of the wind and its outer regions (e.g., Haser et al. 1995). The inclusion of such a parameter was tested, but lead to features which were qualitatively different from the observed DACs, so $v_{\rm turb}$ is set to 0[4]. An example of the resulting profile, including the individual absorption and emission contributions, is calculated in the case of an unperturbed, spherically symmetric wind and shown in Fig. 6.2.

6.4 Results

Each stage of this project allows us to make a number of conclusions about the surface spots and their effect on the wind. Therefore we present the hydrodynamical simulations and the associated computed resonance line profiles separately in the

[4]Such a treatment is reasonable since it has already been shown that CIR-like density structures can inhibit the growth of instabilities, thus greatly decreasing this velocity dispersion [Owocki, 1999]. Presumably, to reproduce the shape of the line's blue edge, instability should be taken into account in the "unperturbed" wind regions between the CIRs, but since it does not constitute the focus of this study, this was not implemented in the line transfer code.

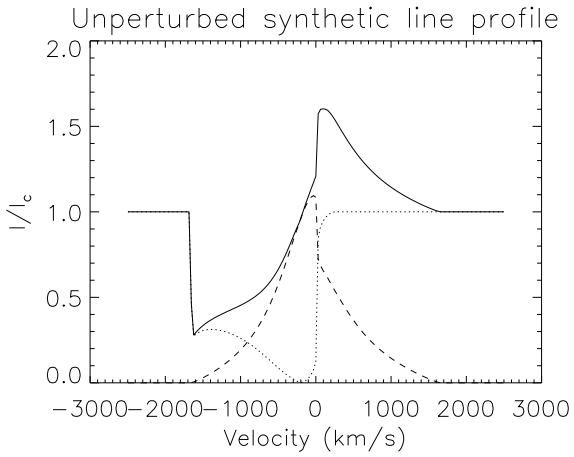

Figure 6.2: Computed P Cygni line profile for a line strength of $\kappa_0 = 1.0$ using an unperturbed wind model (with $\delta = 0.1$). The dotted line shows the absorption component, while the dashed line shows the emission component; the full line corresponds to the total profile. We can see that the absorption is already very strong at around $v/v_\infty = 0.3$.

following subsections.

6.4.1 Wind properties

The first interesting result to investigate is how the global parameters of the wind vary from one model to another. The global mass-loss rate can be calculated by taking:

$$\dot{M} = 4\pi r^2 \rho v \tag{6.3}$$

at a given radius. For an unperturbed wind, ρ and v should be independent of the azimuthal angle ϕ, but that is not the case once the spots are introduced. We can therefore compute for each model an unperturbed mass-loss rate, as well as the mass-loss rate including the effect of the spots to see how much extra material is ejected

Table 6.3: List of properties observed for each of our models. The first four variables refer to wind properties, specifically: $\dot{M}_0$ is the unperturbed mass-loss rate, $\dot{M}_{\rm s}$ is the "spotty" mass-loss rate, $v_{\rm max,0}$ is the unperturbed terminal velocity and $v_{\rm max,\ s}$ is the "spotty" terminal velocity. The last two variables are related to the synthetic line profiles: $v_{\rm start}/v_\infty$ corresponds to the approximate fraction of the terminal velocity at which the DACs appear, and $F_{\rm min}/F_{\rm c}$ is the lowest value found in the quotient spectra (the maximum depth of the DACs).

Model	$\dot{M}_0$ ($10^{-7} M_\odot$/yr)	$\dot{M}_{\rm s}$ ($10^{-7} M_\odot$/yr)	$v_{\rm max,0}$ (10^8 cm/s)	$v_{\rm max,\ s}$ (10^8 cm/s)	$v_{\rm start}/v_\infty$	$F_{\rm min}/F_{\rm c}$
1A	6.41	7.76	2.33	2.85	0.50	0.313
1B	8.56	10.70	1.66	1.94	0.41	0.296
2A	6.41	7.15	2.33	2.32	0.44	0.164
2B	8.56	9.75	1.66	1.61	0.41	0.203
3A	6.41	6.74	2.33	2.31	0.50	0.142
3B	8.56	9.11	1.66	1.62	0.46	0.202

by the spots. In the latter case, we average ρ and v azimuthally. Similarly, we can approximate the terminal velocity v_∞ by taking the maximum radial velocity $v_{\rm max}$ within the simulation zone, and see how it varies between the unperturbed winds and the spotty models. Table 6.3 summarizes these wind properties, as well as other results from the next subsection.

First, we notice that the mass-loss rates are of the same order of magnitude, although slightly larger, than some of the observationally-determined values in the literature (or than that predicted by the empirical relation derived by Lamers and Leitherer 1993). While it is known that theoretically-computed mass-loss rates often differ from empirical values by a factor of a few, part of the discrepancy might also come from the choice of the $\bar{Q}$ parameter (e.g., Gayley 1995).

Furthermore, we notice that the unperturbed terminal velocity for $\delta = 0$ corresponds exactly to the empirical value reported by Kaper et al. [1996]. However, when

the effect of the ionization parameter is included, the terminal velocity decreases significantly. Ultimately, the global structure of the wind scales accordingly, which is why in Sect. 6.4.2 we treat the terminal velocity as a scaling parameter and plot our dynamic spectra in terms of v/v_∞.

While these results inform us about the global wind properties, we require a better insight into the structures which are formed by our simulations. The two main variables of interest for us are the density and radial velocity of the wind throughout the equatorial plane. Following Fig. 6 of Cranmer and Owocki [1996], we show the radial dependence of density for various azimuthal sectors in Fig. 6.3 and that of radial velocity in Fig. 6.4.

We immediately notice a few important properties from these figures.

An obvious effect that can be seen is that the structures are weaker when the spots are larger. This is due to the fact that the spot size, under our set of constraints, is anticorrelated with the brightness contrast. Therefore, for a given photometric variation amplitude, larger spots will generate more subtle structures. Especially in the case of model 3, these structures produce barely noticeable density perturbations.

Another useful interpretation of these results would be to visualize the regions in the wind where most of the absorption takes place. In the Sobolev approximation [Sobolev, 1960], the radial optical depth can be written as:

$$\tau_{\rm Sob} = \frac{\rho q \kappa_{\rm e} c}{dv/dr} \tag{6.4}$$

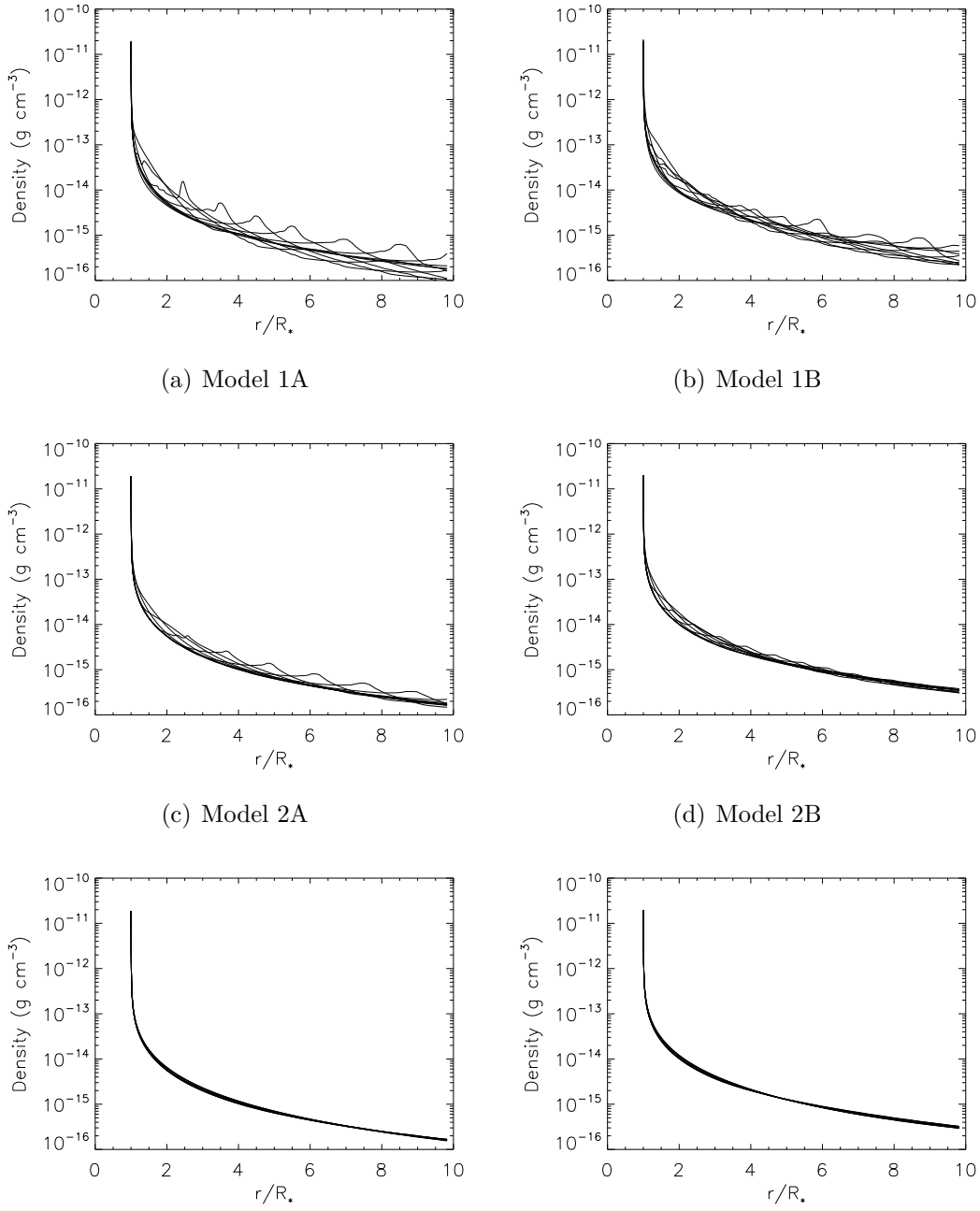

(a) Model 1A

(b) Model 1B

(c) Model 2A

(d) Model 2B

(e) Model 3A

(f) Model 3B

Figure 6.3: Radial dependence of the density for each of our 6 models, shown for azimuthal sectors which are 10° apart.

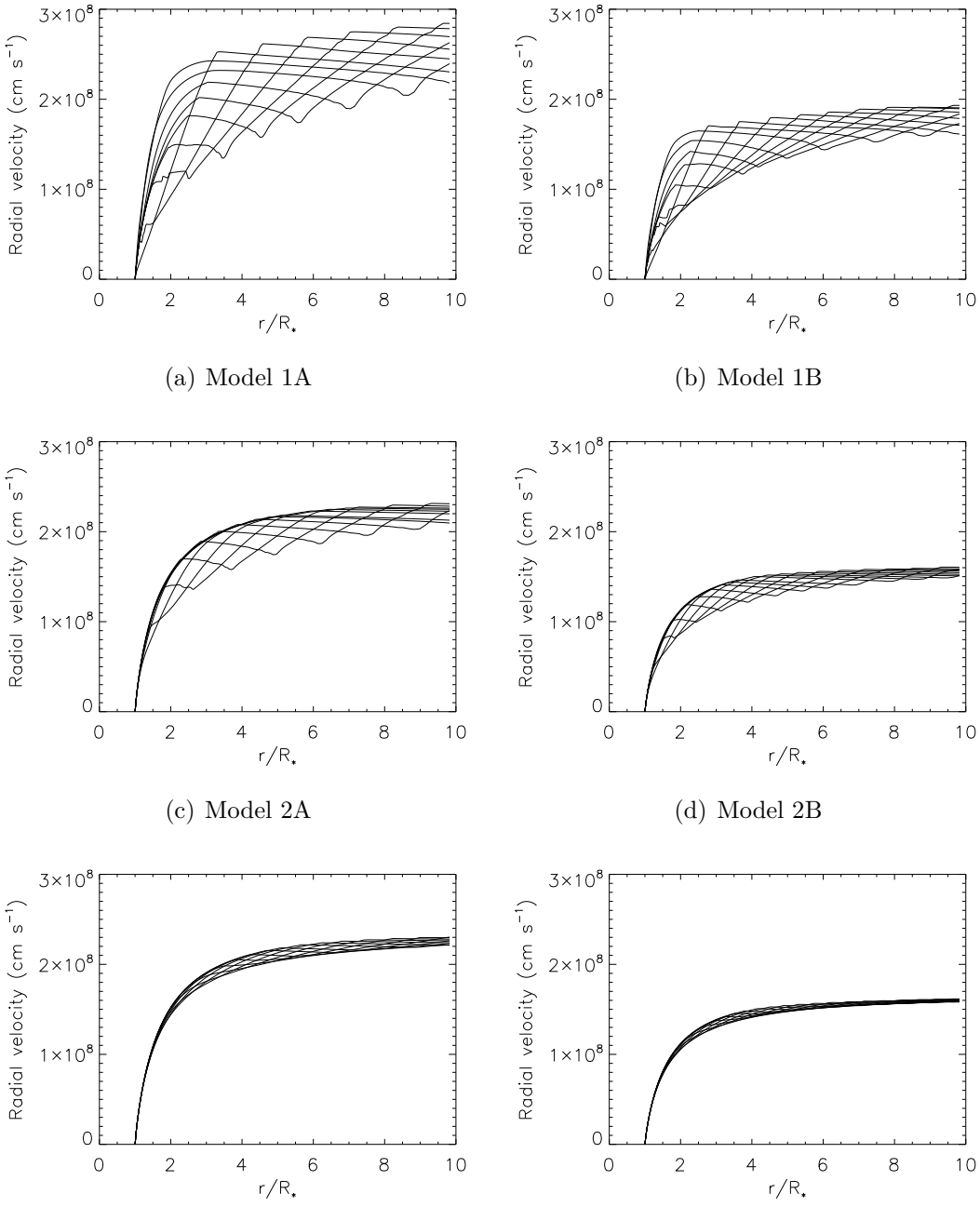

(a) Model 1A

(b) Model 1B

(c) Model 2A

(d) Model 2B

(e) Model 3A

(f) Model 3B

Figure 6.4: Same as Fig. 6.3, but for radial velocity.

where q is the frequency-integrated line strength[5], κ_e is the Thomson scattering opacity, c is the speed of light and dv/dr is the radial velocity gradient. In other words, the optical depth is proportional to the density divided by the radial velocity gradient. We compute this quantity throughout the wind and plot it for each model in Fig. 6.5.

Models 1A and 1B lead to particularly interesting structures: the curvature of the inner edge of the CIRs is very pronounced in the inner wind. This suggests that the extremely overluminous spots overload the wind so strongly that material would perhaps fall back onto the star if it were not for the "boost" provided by the next spot as the star rotates. This might therefore be an artefact of the chosen number of spots and the associated boundary conditions; however, an investigation of the effect of different spot distributions on this phenomenon is not within the scope of this study. We also notice that the larger, weaker spots produce absorption further from the stellar surface. Therefore, in reproducing the inferred properties of CIRs, there is a trade-off between having spots that are large enough to produce wind structures that cover a significant fraction of the stellar disk near the surface, thus accounting for the absorption at low velocities, and brightness contrasts that are strong enough to overload the wind in such a way that the velocity kinks (or breaks in the radial velocity profile when the acceleration becomes null or negative which are responsible for the DACs, Cranmer and Owocki 1996) are close enough to the surface so that this absorption is noticeable.

[5]The line strength q is related κ_0 as follows:

$$q = \frac{\kappa_0}{\kappa_e}\frac{v_{th}}{c} \tag{6.5}$$

where v_{th} is the ion thermal velocity.

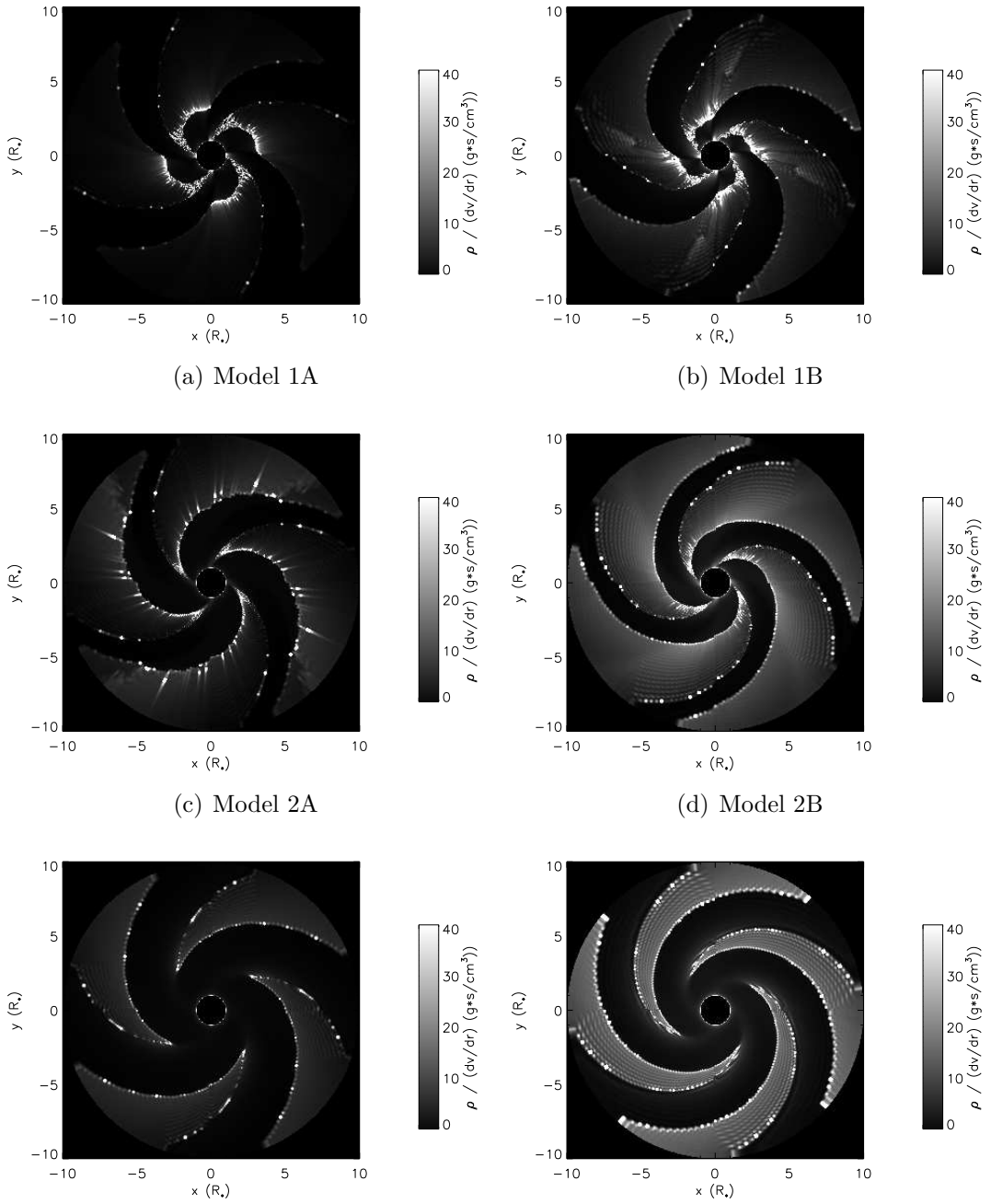

(a) Model 1A

(b) Model 1B

(c) Model 2A

(d) Model 2B

(e) Model 3A

(f) Model 3B

Figure 6.5: Equatorial plane greyscale visualizations of $\frac{\rho}{dv/dr}$, corresponding roughly to the Sobolev radial optical depth, to show where in the wind the absorption occurs in each model.

6.4.2 Synthetic line profiles

Finally, we compute synthetic resonance line profiles for each of our 6 models. To reduce calculation time, we only computed 7 different phases over a quarter of a rotation period, and then repeated them to show two structures evolving in the dynamic spectra. Then, we approximate a "least-absorption" template spectrum, which corresponds roughly to what the profile should be without the extra absorption caused by the CIRs [Prinja et al., 1987], by using the maximum value among the 7 phases for each velocity bin. This constitutes our reference spectrum, by which we divide each spectrum to obtain a quotient spectrum, which will then be plotted against phase to create our dynamic spectra, following the well-known prescription used to visualize DACs in observational data.

Once the dynamic quotient spectra are computed, we compare their characteristics with those of observed UV resonance line profiles from ξ Persei. In particular, we base our comparison on the quantitative analysis performed by Kaper et al. [1999]. Their Fig. 6 shows that the DACs' maximum depth (or the minimum quotient flux) is about 20-30%, and their Figs. 7 and 8 show that the DACs typically first appear in the profiles at about half the terminal velocity. A variety of DAC morphologies are shown in the 4 timeseries which are analyzed in that study.

The results of our SEI calculations are shown in Figs. 6.6 to 6.8. The terminal velocity that is shown on these figures and that is used as a scaling parameter to express the velocity range is estimated from the least-absorption template. Since this template was constructed using the maximum value of flux for each velocity bin, some structures extend beyond the inferred terminal velocity. However, this does not particularly affect the scaling of the wind since the underestimation of the terminal

velocities is small compared to the values themselves.

A first immediate conclusion is that all models do produce the type of variation that is observed. Indeed, we produce signatures which are morphologically similar to those seen in observations. This is quite remarkable, especially for models 3A and 3B since, as mentioned earlier, the structures found in the wind are rather subtle, which illustrates very well the conclusion of Cranmer and Owocki [1996] that DACs are formed by velocity kinks, not by overdense regions in the wind.

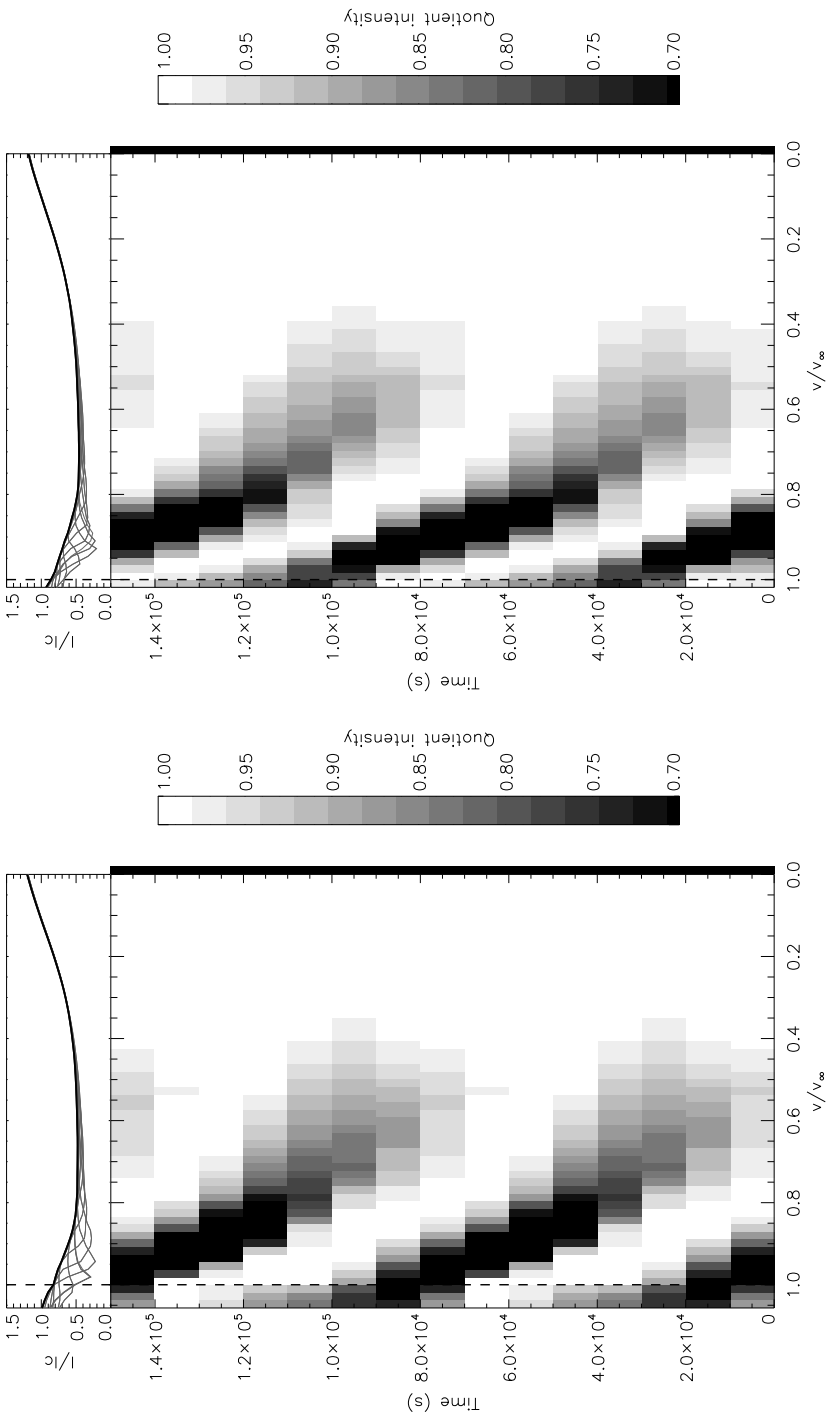

(a) Model 1A synthetic line profile.

(b) Model 1B synthetic line profile.

Figure 6.6: *Left:* Dynamic spectrum (bottom panel) generated using synthetic line profiles generated from model 1A (shown in the top panel in grey) divided by a "least-absorption" template spectrum (shown in the top panel in black). The dashed black line represents v_∞. *Right:* Same, but for model 1B.

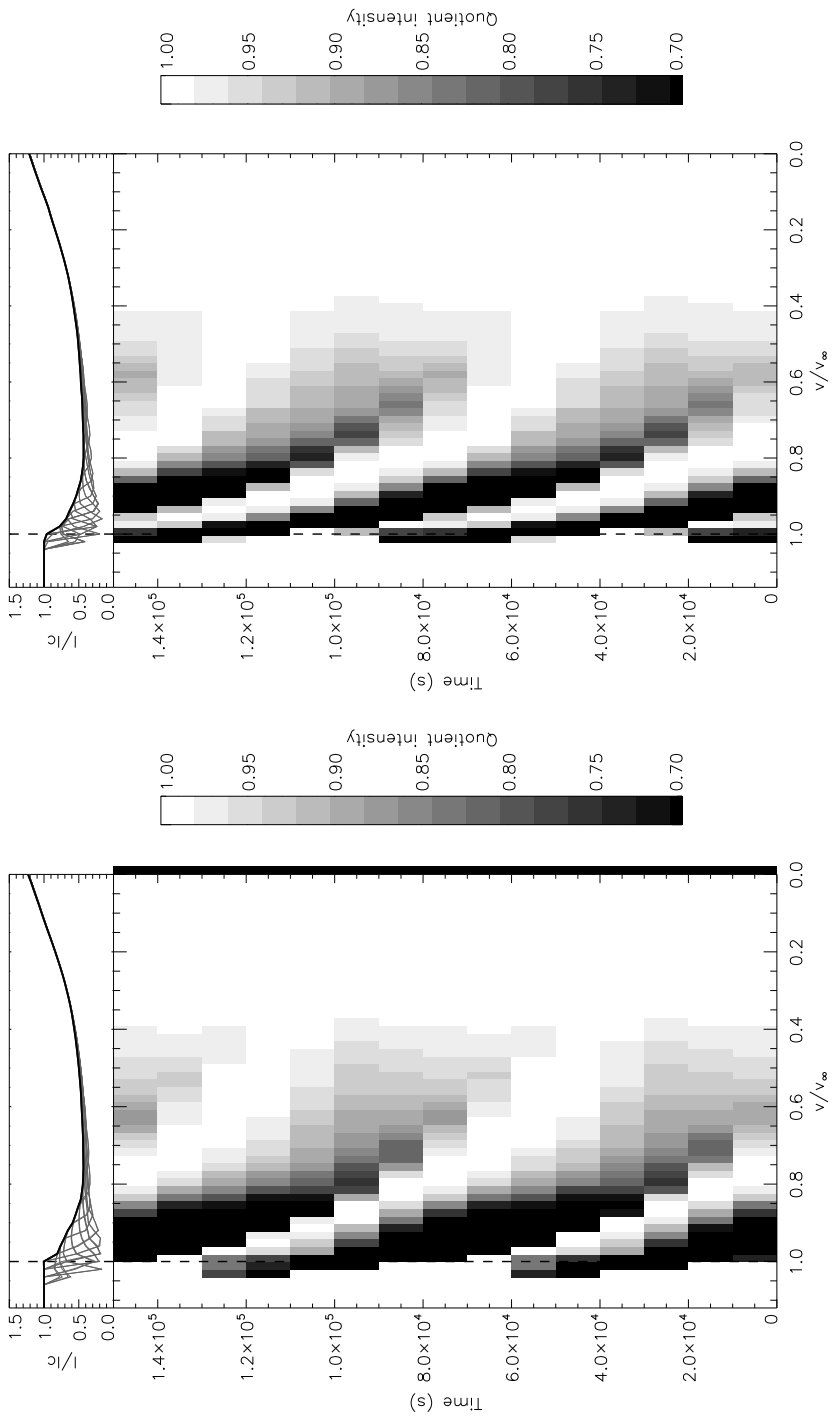

(a) Model 2A synthetic line profile.

(b) Model 2B synthetic line profile.

Figure 6.7: Same as Fig. 6.6, but for models 2A and 2B.

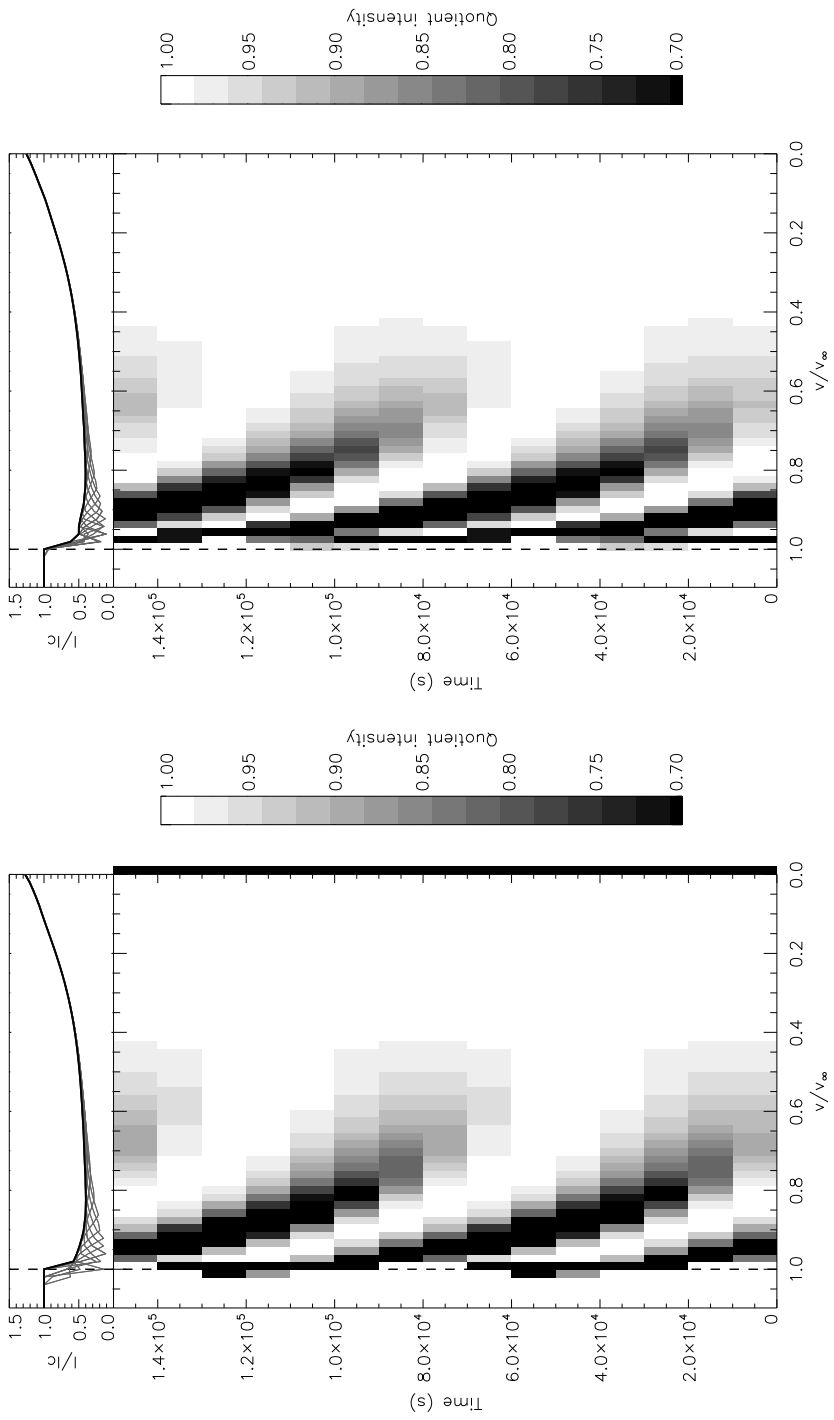

(a) Model 3A synthetic line profile.

(b) Model 3B synthetic line profile.

Figure 6.8: Same as Fig. 6.6, but for models 3A and 3B.

As to the quantitative behaviour of these DACs, we see that they first appear at about half the terminal velocity. However, to better situate their starting point, we can instead use the DAC-fitting method used by Henrichs et al. [1983] and Kaper et al. [1999] by fitting a Gaussian absorption profile to each absorption feature in the quotient spectra:

$$I(v) = \exp\left(-\tau_c \exp\left[-\left(\frac{v - v_c}{v_t}\right)^2\right]\right) \tag{6.6}$$

where v_c corresponds to the central velocity of the feature, v_t corresponds to its width and τ_c is the central optical depth. We then find the feature for each model that appears at the lowest velocity and consider that velocity to be the starting velocity of the DACs (expressed as a fraction of the "terminal velocity" of the reference spectrum in Table 6.3). These values are compatible with those found for ξ Persei by Kaper et al. [1999]. Following their analysis, we can also trace the evolution of the 3 quantities appearing in Eq. 6.6 for a single DAC caused by a CIR wrapping around the star. Fig. 6.9 shows such an analysis performed for model 2B.

The fit parameters of our synthetic DACs show clear trends: the DACs become stronger and narrower as they evolve through the velocity space. These trends are slightly less clear at low and near-terminal velocity. When the DACs first form, there is significant asymmetry in their profile, leading to unsatisfactory fits using a purely Gaussian profile; furthermore, the low resolution makes it more difficult to fit weak features. On the other hand, when they are near terminal velocity, the departures from the trends could be due in part to the finite simulation range, which truncates the CIRs which cause them.

Finally, the maximum depth of the quotient dynamic spectrum for each model is

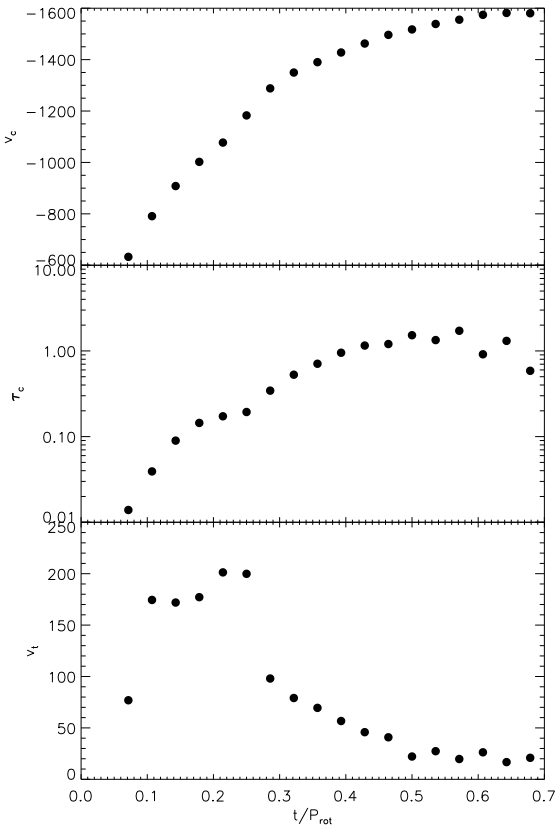

Figure 6.9: DAC characteristics for model 2B: the top panel shows the evolution of the central velocity of the DAC (v_c) with time, the middle panel traces the central optical depth of the absorption feature (τ_c) and the bottom panel traces its broadening parameter (v_t).

compiled in Table 6.3. Once again, these values are compatible with the observed values, which range between about 20 and 30%. However, it should be noted that given the way our reference spectrum was constructed, the depths might be slightly overestimated, compared to the observational ones. Nevertheless, they span the expected range, confirming that we successfully reproduce the properties of ξ Persei's DACs.

6.4.3 Effect of ionization

The most obvious effect observed when the ionization parameter δ is introduced is a global reduction of the wind velocity (as shown in Fig. 6.4), as well as an increase in the mass-loss rate (see Table 6.3). We also see from Fig. 6.5 that including a non-zero ionization parameter strengthens the optical depth of the CIRs and produces them closer to the stellar surface. However, the inclusion of this effect barely influences the computed line profiles. The main reason for this lies in the fact that for a strong UV resonance line, the absorption is nearly saturated at low velocities, making it difficult to distinguish variability. Indeed, looking at a typical unperturbed profile, we see that the absorption is already nearly saturated at about $v/v_\infty = 0.3$ (as shown in Fig. 6.2). This means that resonance lines are not optimally suited to study the wind structure near the stellar surface, which is already well known (e.g., Massa and Prinja 2015). To fully account for that region of the wind, we would need to study synthetic excited state lines[6], which our code cannot generate in its present version. Therefore, based solely on the direct comparison of our models with the observables at our disposal, little can be said of the importance of including the ionization parameter

[6]It is also possible to investigate weaker lines, but this study specifically focussed on the type of lines in which DACs were observed.

in our simulations.

6.5 Conclusions and future work

In this study, we have carried out 2D radiation hydrodynamical simulations of ξ Persei's wind by inputting bright spots on its surface using constraints derived from the photometric limits found by Ramiaramanantsoa et al. [2014]. We then extrapolated these results to 3D using the same prescription as Cranmer and Owocki [1996] and used SEI to generate UV resonance line profiles. The whole process allowed us to test various spot and wind parameters and see what sort of structures they generated, and then what kind of spectroscopic signatures those structures caused. Based on these experiments, we conclude the following:

- All 6 spot models cause perturbations in the velocity and density profiles of the wind. Models with smaller and stronger spots cause stronger features, while large and weak spots generate very subtle structures. The hydrodynamical simulations also show evidence that the spots enhance the overall mass-loss rate and that the inclusion of the effect of ionization globally slows down the wind and increases mass loss, leading to stronger absorption in the CIRs.

- The synthetic line profiles show classical DAC behaviour for all models. The quantitative behaviour of the DACs also agrees with observations: they appear at a little less than half the terminal velocity, then get stronger and narrower as they evolve in the velocity space, reaching a maximum depth of around 20%.

- The fact that these models all reproduce the pattern of variability associated to DACs suggest that there can exist a variety of these structures in the wind

of ξ Persei at different times. If we accept the idea that these structures are generated by bright spots on the surface of the star, this would mean that this scenario is consistent with the idea that these spots are stochastic, appearing and disappearing over a characteristic timescale, with varying strengths and sizes. This would also explain the cyclical (rather than periodic) nature of DACs.

As to the nature of the physical phenomenon giving rise to these spots, the present work helps place lower limits on the strength that magnetic spots (e.g., Cantiello and Braithwaite 2011) would need to have to produce the appropriate brightness enhancements. Using Eq. 6 from David-Uraz et al. [2014], we approximate that the field strength required to generate the brightness contrast used in model 1 is 660 G, whereas model 2 requires a 330 G field and model 3 requires a 160 G field. Such fields could be detectable using very deep magnetometry, although that detection might be difficult to perform on a fast rotator like ξ Persei. Of course, the larger the spots, the harder it would be to detect them. However, as seen throughout Sect. 6.4, larger spots lead to weaker structures, and the extra absorption they cause occurs further away from the star, which might be at odds with various other observational diagnostics, including excited state lines [Massa and Prinja, 2015]; this means that the more likely progenitors of the structures which cause DACs are also more likely to be detectable.

The best way to probe the wind structures near the stellar surface would therefore be to generate line profiles corresponding to such diagnostics. Another important observable to investigate would also be the behaviour of Hα. Indeed, variations in Hα are known to be linked to DACs, but their patterns typically do not look as well

organized as that of their UV counterparts. Nevertheless, since high-resolution optical spectroscopy is much more accessible than UV spectroscopy these days, it would be very useful to make sense of these patterns and figure out whether they allow us to infer anything about the surface perturbations which cause them.

Finally, while the goal of this paper was to match observables for one particular star, future work should extend the parameter space to account for the great variety of DAC signatures found in all OB stars, not just ξ Persei, hopefully placing constraints on surface properties based on the characteristics of the wind variability.

Acknowledgments

This research has made use of the SIMBAD database operated at CDS, Strasbourg, France and NASA's Astrophysics Data System (ADS) Bibliographic Services.

ADU gratefully acknowledges the support of the *Fonds québécois de la recherche sur la nature et les technologies*. GAW is supported by an NSERC Discovery Grant.

ADU also warmly thanks Nathaniel Dylan Kee for his helpful comments and kind guidance.

Chapter 7

Paper III: Modelling bright spots on the surface of massive stars

Paper Title[1]: "Investigating the origin of cyclical wind variability in hot, massive stars - III. Empirical modelling of co-rotating bright spots on the surfaces of OB stars"

[1]This chapter contains a version of a paper currently in preparation and shortly to be submitted to Monthly Notices of the Royal Astronomical Society as: A. David-Uraz, G.A. Wade, V. Petit and D.A. Hanes.

7.1 Abstract

OB stars exhibit various types of spectral variability associated with wind structures, including the apparently ubiquitous discrete absorption components (DACs). They are thought to be caused by either magnetic fields or non-radial pulsations. In the third paper of this series, we present empirical numerical tools to interpret photometric and spectroscopic observations in light of the bright spot paradigm used to explain the large-scale azimuthal wind structures hypothesized to lead to DACs. In particular, we present simple models yielding synthetic optical light curves and dynamic spectra of photospheric lines. We show that they can be used to constrain the properties of bright spots, although certain degeneracies prevent the recovery of these properties using photometry alone. These degeneracies can be lifted using predicted variations in photospheric lines. We present a rudimentary spot evolution code which implements these tools to interpret the light curve of the O giant ξ Persei. Based on this modelling, we suggest that the spots might appear preferentially at certain longitudes, although the nature of the mechanism leading to this distribution is unknown.

7.2 Introduction

Timeseries of ultraviolet spectroscopic observations of hot, massive stars obtained by the International Ultraviolet Explorer (*IUE*) exhibit cyclical variations, notably in the wind-sensitive resonance lines. The most common pattern of variability involves the migration of narrow absorption features through the velocity space over a characteristic timescale, also known as "discrete absorption components" (DACs, e.g., Prinja et al. 1987, Prinja and Howarth 1988). These features have been interpreted as

resulting from large-scale azimuthal wind structures (co-rotating interaction regions or CIRs, Mullan 1986). While their underlying physical cause remains unknown, introducing *ad hoc* bright spots on the photosphere, which drive locally enhanced outflows, has led to successful modelling of these structures [Cranmer and Owocki, 1996, David-Uraz et al., in prep.].

Recently, space-based photometric observations of the O giant ξ Persei obtained with the Microvariability and Oscillations in STars telescope (*MOST*) were claimed [Ramiaramanantsoa et al., 2014] to support this "bright spot paradigm" (BSP) by providing the first detection of co-rotating bright spots on the surface of an O star. This conclusion was mostly supported by the fact that the light curve could not be reliably fitted using the 12 most significant frequencies in the Fourier power spectrum, as well as the fact that they did not follow any recognizable frequency pattern. However, the spot modelling performed by Ramiaramanantsoa et al. [2014] focused mostly on the photometric features and did not provide detailed insight about the physical properties of the spots themselves, relying on a number of assumptions derived from solar physics.

Nevertheless, there is significant motivation to recover specific spot properties and trace the evolution of these properties over time. On one hand, painting a precise picture of the spots which are inferred to cause the light curve variations would allow for predictions of various observational diagnostics. Given that the BSP is phenomenologically – rather than observationally or theoretically – motivated, confronting firm predictions with observations will prove essential in either confirming or refuting this model. On the other hand, it is necessary for the properties of spots to be well constrained in order to determine their physical cause, should they exist. In particular,

theoretical investigations of the sub-surface iron convection zone (FeCZ) believed to exist within the radiative envelopes of OB stars [Cantiello et al., 2009] predict that small-scale magnetic fields can be generated in the FeCZ and advect to the surface [Cantiello and Braithwaite, 2011], but the properties of these fields remain poorly constrained. It is not unreasonable to hypothesize that these magnetic spots are responsible for the surface brightness enhancements used in the model developed by Cranmer and Owocki [1996], although no such link has been demonstrated as of yet. Even so, based on this idea, it is possible to derive a relation between the field strength and the generated brightness contrast [David-Uraz et al., 2014]; thus by recovering the brightness contrast of a spot that is postulated to be responsible for a given light curve variation, the detectability of the small-scale field that generated said spot can be estimated.

Therefore, the goal of this study is to develop a consistent empirical modelling method for bright spots which yields meaningful information about their properties. To do so, we also aim to predict spectroscopic signatures in photospheric line profiles, as well as the secular evolution of these features. The details of the model used to generate these synthetic diagnostics are described in Sect. 7.3. The results of single spot modelling are shown in Sect. 7.4, while evolving multi-spot models are presented in Sect. 7.5. Finally, Sect. 7.6 contains the conclusions that we draw from this work and indicates ways in which this method can be used to better understand – and challenge – the BSP.

7.3 Numerical methods

In this section, we provide a detailed description of the model used to produce the synthetic light curves and photospheric profiles of interest in this study.

This model places bright spots at designated places on the surface of a star and then allows us to calculate their effect on the total integrated light as well as the line profiles. To do so, it generates a 50,000-point grid distributed on the surface of a sphere which represents the stellar surface. For simplicity, we have not included the effect of rotational oblateness. The grid is equally spaced in latitude (θ), and each latitudinal sector is divided into a certain number of longitudinal points (ϕ) such that each cell has roughly the same area:

$$d\phi(\theta) \propto 1/\sin\theta \tag{7.1}$$

where $d\phi(\theta)$ is the increment in longitude for a given latitude θ.

Surface spots are defined using four parameters: latitude ($\theta_{\rm s}$), longitude ($\phi_{\rm s}$), angular radius (r) and brightness enhancement (A). The first two parameters are defined in the stellar frame of reference. That is, at phase 0, the center of the line of sight intersects with the meridian located at $\phi = 0$. The angular radius corresponds to the angular distance between the center of a spot and a point on its edge as measured from the center of the star, meaning that any point on the grid with latitude θ and azimuth ϕ such that

$$\arccos\left(\cos\theta\cos\theta_{\rm s}\cos(\phi-\phi_{\rm s}) + \sin\theta\sin\theta_{\rm s}\right) \leq r \tag{7.2}$$

is considered to be within the spot. Finally, the spots have uniform brightness,

therefore points which observe the above relation have their flux multiplied by the brightness enhancement factor of the spot.

The grid is then transformed into Cartesian coordinates (x, y, z; normalized to the stellar radius):

$$x = \sin\theta\cos\phi \tag{7.3}$$

$$y = \sin\theta\sin\phi \tag{7.4}$$

$$z = \cos\theta \tag{7.5}$$

It is then rotated into the line-of-sight coordinates (x', y', z') given a certain phase (ψ) and inclination angle (i) using the following rotation matrix:

$$\begin{bmatrix} \cos\psi & -\cos i\sin\psi & \sin i\sin\psi \\ \sin\psi & \cos i\cos\psi & -\sin i\cos\psi \\ 0 & \sin i & \cos i \end{bmatrix}$$

The disk integration can then be performed on the visible side of the sphere (i.e., where $z' \geq 0$).

7.3.1 Synthetic light curves

To produce the light curve, we take into account first-order continuum processes. Therefore, the only factors that come into play are the projected area of each cell, the intrinsic flux of each cell and limb darkening. We do not account for possible changes in the continuum slope due to perturbations in the surface temperature (which, presumably, might be responsible for the brightness contrast of spots in the BSP); thus,

the inferred light curves are colour-independent.

We first perform a disk integration of a pristine star without any spots; we start by calculating a linear limb darkening factor for each cell [Schwarzschild, 1906]:

$$\frac{I_c}{I_{c,0}} = 1 - \epsilon + \epsilon \cos\theta' \tag{7.6}$$

where $I_{c,0}$ is the specific continuum intensity without taking into account limb darkening, I_c is the specific continuum intensity *including* the effect of limb darkening, ϵ is the limb darkening parameter and θ' corresponds to the angle from the center of the visible portion of the sphere to another point on the visible portion of the sphere, as measured from its center (or in other words the "limb angle"; this angle varies between 0 and $\pi/2$). To compute a total unperturbed brightness value ($I_{\mathrm{tot},0}$) which is normalized to the intensity of a single cell ($I_{c,0}$), we compute the projected area of each individual cell (proportional to $\sin\theta' \cos\theta'$) multiplied by its limb darkening factor, and sum the product for all visible cells ($z' \geq 0$).

To include the effect of the spots, we repeat a similar calculation, but instead taking into account:

$$\frac{I'_c}{I_{c,0}} = f_s \frac{I_c}{I_{c,0}} \tag{7.7}$$

where f_s is a factor which is equal to 1 for a cell which is not within a spot, and equal to A (the spot's brightness enhancement) for a cell which is within a spot. Summing this quantity over the visible portion of the sphere we obtain the total brightness for a given spot configuration at a given phase (I_{tot}). We then convert the result to obtain the differential magnitude:

$$\Delta m = -2.5 \log \left(\frac{I_{\rm tot}}{I_{\rm tot,0}} \right) \tag{7.8}$$

This calculation is repeated for various phases to obtain a light curve.

7.3.2 Synthetic photospheric line profiles

In order to generate photospheric lines, we require additional input parameters. In particular, the projected rotational velocity ($v \sin i$) must be defined, as well as the desired output spectral resolution. From these two parameters, we can generate an array of velocities which will span the line profile. Then, for each cell of the grid, we can compute a local absorption profile (assumed to be Gaussian):

$$I_{\rm local}(v) = I'_c \exp \left(\frac{-(v - v_z)^2}{\sigma^2} \right) k_{\rm lw} \tag{7.9}$$

where I'_c is the specific continuum intensity (as calculated for the light curve module, i.e., the projected area multiplied by the limb darkening factor and the brightness enhancement factor, in the case where the cell is part of a spot), v_z is the line-of-sight component of the rotational velocity of the cell (which can be computed by multiplying $v \sin i$ by the line-of-sight x' component of the cell, normalized to the stellar radius), σ is a broadening parameter which includes thermal broadening, defined as a function of the effective temperature of the star ($T_{\rm eff}$) and the mass of the species considered (m), and microturbulent broadening (ξ):

$$\sigma = \sqrt{\frac{2kT_{\rm eff}}{m} + \xi^2} \tag{7.10}$$

and finally, $k_{\rm lw}$ is the so-called "line weakening" factor[2] (e.g., Deutsch 1970). We compute that factor by using model line profiles generated for a given effective temperature and surface gravity using SYNTH3 [Kochukhov, 2007], and fitting the line depth for different values of θ' to a third-order polynomial. That fit can then be calculated for each grid cell and normalized to obtain $k_{\rm lw}$. SYNTH3 also provides various values of continuum as a function of limb angle, so we can also fit the continuum limb darkening parameter to better reproduce the line profile, rather than using a fixed value.

Once the local absorption profiles have been computed for each visible cell on the grid, they are added together (since they are already weighted by the specific intensity of the cell and are all generated for the same velocity array) to form the disk-integrated absorption profile ($I_{\rm abs}(v)$), renormalized to a specified depth and convolved with a Gaussian whose width corresponds to a given instrumental resolution. Finally, the code outputs the continuum-normalized line profile, which is $1 - I_{\rm abs}(v)$. It should be noted that Eq. 7.9 implies that bright spots lead to *enhanced* absorption which then manifests itself as small features of additional absorption which migrate through the line profile over the course of half the rotational period. While this may initially seem somewhat counterintuitive, it is actually expected since the brighter region contributes more continuum photons, thus locally deepening the line profile.

7.3.3 Sample results

In this section, we present a few test calculations to show typical outputs of both our photometric and spectroscopic models. Fig. 7.1 shows sample light curves for

[2]This is actually a bit of a misnomer since this effect relies on the varying ionization levels as a function of the limb angle, which can, depending on the species considered, either weaken or strengthen the line as the limb angle increases.

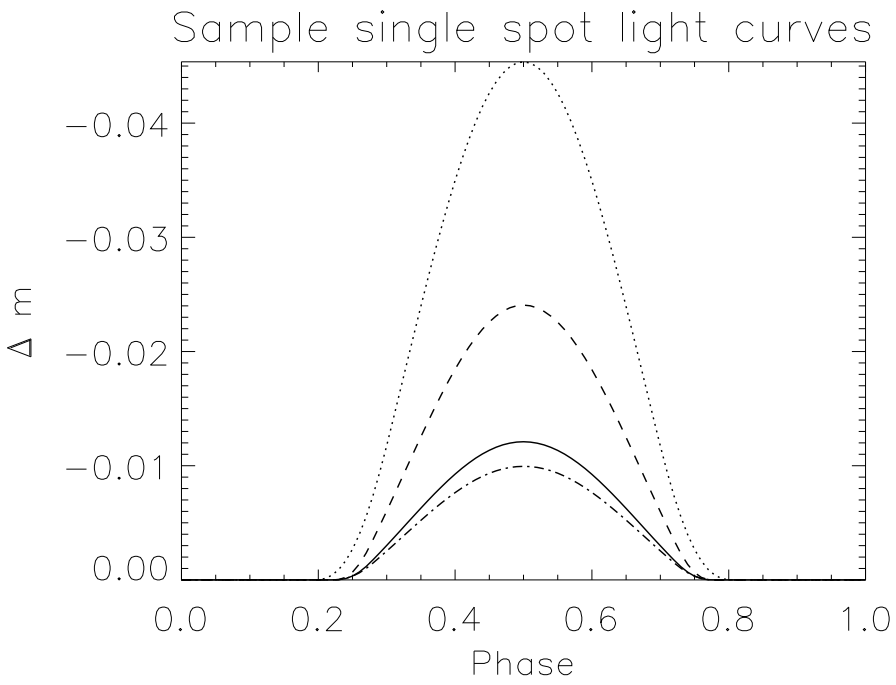

Figure 7.1: Sample synthetic light curves for different single spot models. *Plain:* $A = 1.33$, $r = 10°$, $\theta_s = 90°$; *Dashed:* $A = 1.66$, $r = 10°$, $\theta_s = 90°$; *Dotted:* $A = 1.33$, $r = 20°$, $\theta_s = 90°$; *Dashed-dotted:* $A = 1.33$, $r = 10°$, $\theta_s = 60°$.

four different single spot models, all computed for a star seen equator on ($i = 90°$): one model corresponds to the intermediate model used by David-Uraz et al. [in prep.] (their *model 2*), i.e., equatorial spots with a 10° radius and a 33% brightness enhancement; the other three models correspond to variations of this first model in which one parameter at a time is tweaked (either the radius or the brightness enhancement is doubled, or the latitude is set to 60°). Of course, each of these models produce light-curve variations with different amplitudes (this will be investigated in greater detail in Sect. 7.4.

We can also test the line weakening calibration described in Sect. 7.3.2 by computing a photospheric line in the absence of bright spots and comparing it to a profile

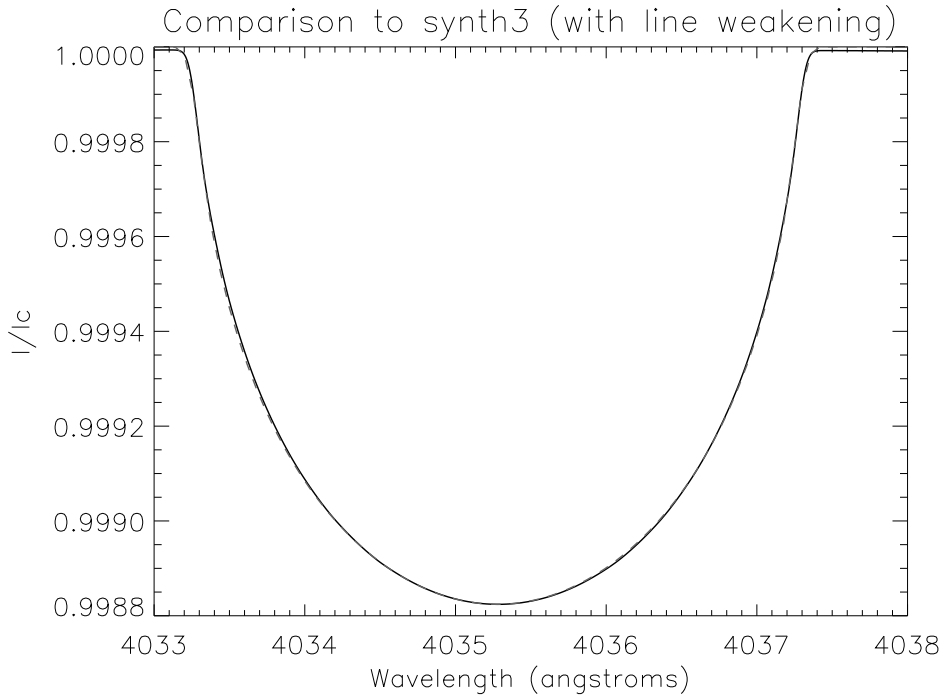

Figure 7.2: Computation of a photopheric line (SiII λ4035) without spots to show the successful calibration to the SYNTH3 model; the dashed line corresponds to the original SYNTH3 line profile and the full line corresponds to our model calculation, but they are essentially indistinguishable.

obtained using SYNTH3; the result is shown in Fig. 7.2 and conclusively proves that this calibration is successful. In this case, we used an effective temperature of 20 kK and a surface gravity of $\log g = 3.0$, as well as a projected rotational velocity of 150 km/s (and no microturbulent broadening).

Finally, we can also follow the effect of a spot within a photospheric line profile as the spot rotates across the stellar disk. Again, using a model with $A = 1.33$, $r = 10^\circ$ and $\theta_\mathrm{s} = 90^\circ$ (which reproduces the photometric amplitude observed in ξ Persei by Ramiaramanantsoa et al. 2014), we overplot the line profile (computed with $v \sin i = 150$ km/s) at phase intervals of 0.05; the result is shown in the top

panel of Fig. 7.3, while the bottom panel shows an equivalent way of presenting this result using a dynamic quotient spectrum, dividing out the profile at each phase by the unperturbed line profile. We see that the maximum relative variation within the line is of the order of 1.2%, meaning that a signal-to-noise ratio (SNR) per spectral bin at the line center of approximately 250 is required to make a 3σ detection of the "spotty" spectral feature.

7.3.4 Spot generation model

While our model can produce synthetic light curves and dynamic spectra for static spots, it also includes a module to produce these observational diagnostics in the context of evolving stochastic spots. This capability was included specifically to try to reproduce similar results to those obtained by Ramiaramanantsoa et al. [2014] for ξ Per, while recovering physically motivated spot properties. Given a set of five characteristic spot parameters (average timescale between the appearance of two spots, average lifetime, latitude, angular radius and maximum brightness enhancement of a spot) as well as their standard deviation (we assume these properties to be normally distributed), we randomly generate spots over the specified duration of the simulation (the longitude of a spot is picked at random). Following the modelling of Ramiaramanantsoa et al. [2014], we let the spots rise and decay linearly, although we use a simpler model in which the rise and decay both occur during half the lifetime of the spot, such that for a spot appearing at time $t_{\rm start}$ with a given lifetime τ and a maximum brightness enhancement of $A_{\rm max}$, the brightness enhancement A as a function of time is given by:

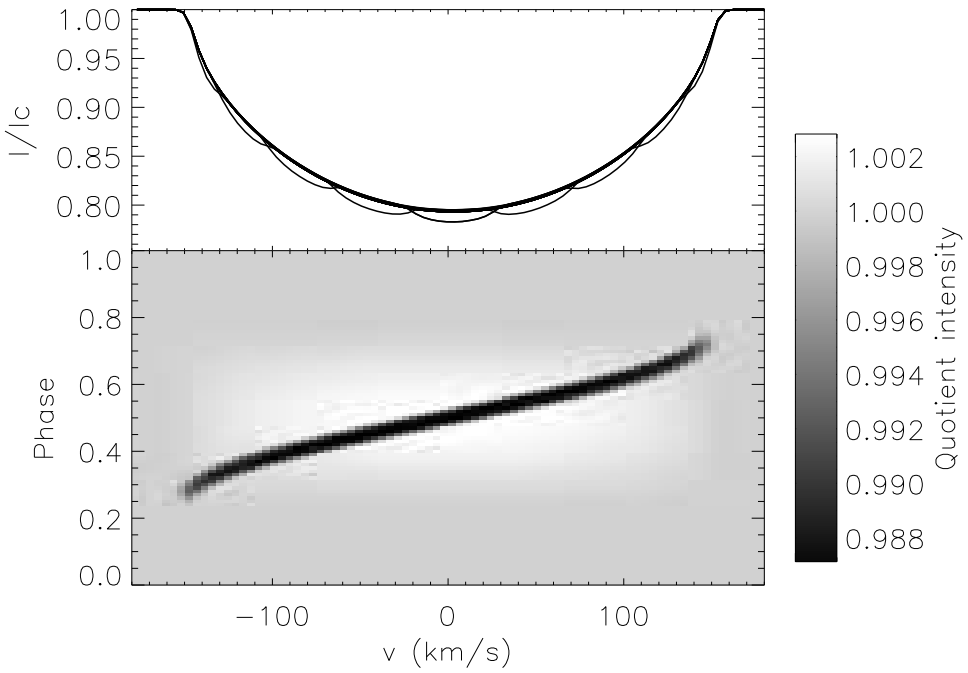

Figure 7.3: Computation of a generic photopheric line including the effect of an equatorial spot with a radius of 10° and a brightness enhancement of 33%. For simplicity, we used a stripped down version of the spectroscopic module for this calculation, neglecting line weakening and assuming a fixed limb darkening parameter. The top panel shows profiles calculated at intervals of 0.05 in phase and overplotted, while the bottom panel shows the associated dynamic quotient spectrum, a stacked 2D greyscale plot with velocity on the x-axis and phase on the y-axis; the greyscale represents the normalized intensity of the line profile divided by that of the unperturbed line profile (i.e., in the absence of a spot).

$$A(t) = \min\left\{A_{\max}\left(1 - \frac{2}{\tau}\left|t - (t_{\rm start} + \tau/2)\right|\right), 1\right\}. \quad (7.11)$$

Multiple spots can co-exist at any given time; therefore for each timestep we compute the spots which are present and use them as input to our photometric and spectroscopic modules. This allows us to simulate light curves and dynamic spectra of photospheric lines for evolving stochastic spots. Of course, this *ad hoc* model of spot evolution might not perfectly correspond to the actual behaviour of spots, should they exist, but it allows a comparison between our results and those of Ramiaramanantsoa et al. [2014], and can be refined by using the results which will be discussed in the following section.

7.4 Inferring single spot properties

A first test to determine the predictive power of this model is conducted by studying single spot configurations and determining whether it is possible to recover the spot properties and how well they can be constrained. First, we generate a grid of models with fixed constant spots for different values of the spot parameters A, r and $\theta_{\rm s}$, assuming an equator-on inclination angle $i = 90°$, and let them evolve over one full rotational period (separated in 101 equally-spaced phases), producing a light curve for each model by using the photometric module (similar to that shown previously in Fig. 7.1)[3]. The characteristics of the peak caused by a bright spot in the light curve can inform us about the spot properties. For each light curve, given the set of differential magnitudes (Δm_i) and phases (ψ_i), we set the minimum brightness as

[3]To produce these light curves, we use a fixed limb darkening parameter ($\epsilon = 0.3$), typical of massive star atmospheres in the optical range (e.g., Al-Naimiy 1978).

the zero-point and compute the amplitude of the variability ($A_{\rm var}$; in magnitudes), the mean (μ), standard deviation ($\sigma_{\rm p}$) and excess kurtosis (g_2) of the peak (in phase units), defined as follows:

$$A_{\rm var} = -\min(\Delta m_i) \tag{7.12}$$

$$\mu = \frac{\sum\limits_i \Delta m_i \psi_i}{\sum\limits_i \Delta m_i} \tag{7.13}$$

$$\sigma_{\rm p} = \sqrt{\frac{\sum\limits_i \Delta m_i (\psi_i - \mu)^2}{\sum\limits_i \Delta m_i}} \tag{7.14}$$

and

$$g_2 = \frac{\sum\limits_i \Delta m_i (\psi_i - \mu)^4}{\sigma_{\rm p}^4 \sum\limits_i \Delta m_i} - 3 \tag{7.15}$$

It should be noted that we skip the third moment (skewness) since we are working here with fixed, constant spots. Therefore, the peak should be symmetric and the skewness uniformly null. Similarly, the mean (in phase units) is uniformly 0.5 since we place our spot at a longitude of $\phi_{\rm s} = 180°$, but is defined here because it appears in the following expressions.

The results are shown in Figs. 7.4, 7.5 and 7.6. To isolate the effect of each individual spot property, the variables are averaged over the other parameters. We can clearly see that all three parameters influence $A_{\rm var}$. On the other hand, $\sigma_{\rm p}$ is essentially unaffected by A, while g_2 depends mostly on r. However, since the dominating effect resides in the change of the variation amplitude, resolving degeneracies might not be

straightforward, especially when accounting for noise (this will be addressed in more detail shortly).

Of course, this is a slightly simplistic model since not all stars are viewed equator-on. However, given the geometry of the system, $\theta_{\rm s}$ and i have degenerate effects on the light curve, meaning that they are essentially interchangeable. This can be readily understood by considering the variation of the limb angle (θ') as a function of phase; it remains identical even if we permutate $\theta_{\rm s}$ and i. Nevertheless, when we consider both variables simultaneously, a slightly more complex picture arises; for instance, the monotonic behaviour of $A_{\rm var}$ as a function of $\theta_{\rm s}$ shown in Fig. 7.4 can become non-monotonic depending on the inclination. Specifically, when the inclination is closer to pole-on, equatorial spots might cause fainter brightness variations than spots which are a few degrees of latitude off the equator because they remain at very high limb angles during the entire portion of the rotational period during which they are visible. Issues can also arise from spots near the pole, since they could be visible at all phases.

While the light curves are not very useful to distinguish between spot latitude and inclination, spectroscopy can help place better constraints on these parameters. In particular, measuring the rotational line broadening yields the projected rotational velocity, $v \sin i$. This can, in turn, be used to constrain i. If it is possible to measure accurately the rotational period from the light curve (by tracing the periodic behaviour of individual spots) and if the stellar radius is known, then i can be calculated precisely, decisively lifting the degeneracy.

It is also possible to model spots with a variable brightness enhancement. We consider a linear variation of the form:

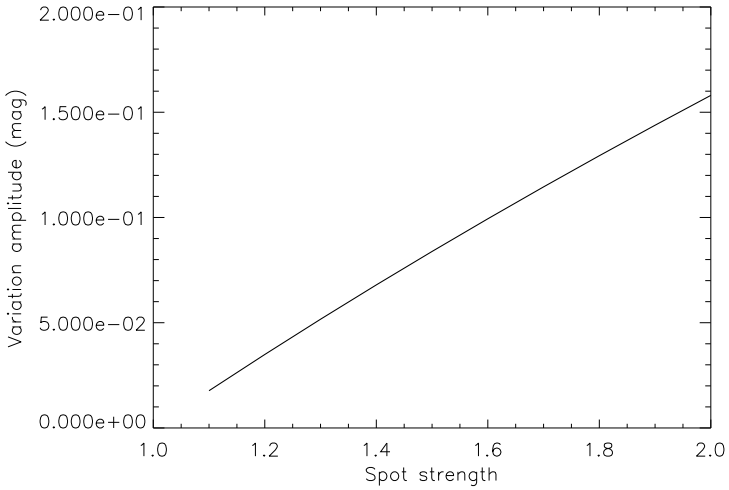

(a) $A_{\rm var}$ vs. A

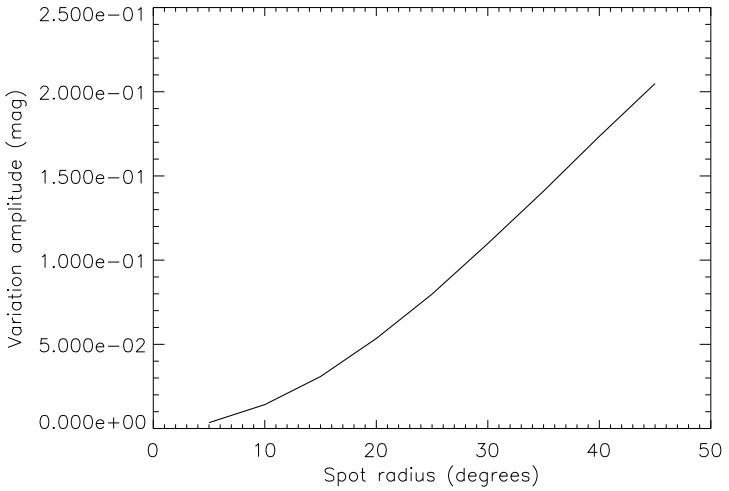

(b) $A_{\rm var}$ vs. r

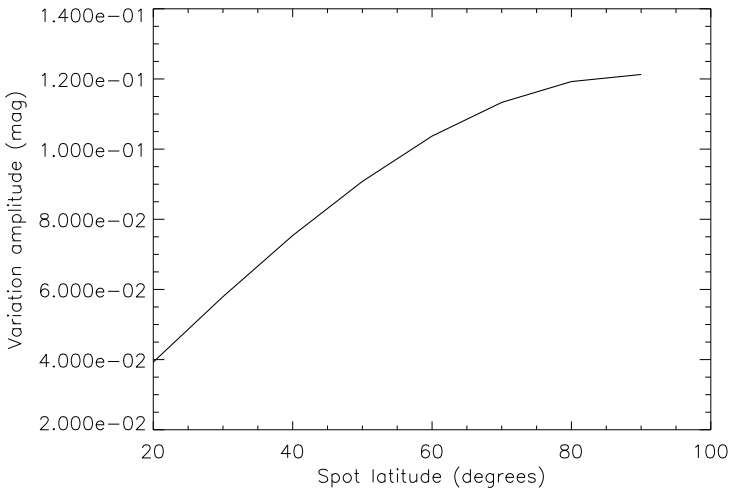

(c) $A_{\rm var}$ vs. $\theta_{\rm s}$

Figure 7.4: Correlation (or lack thereof) between the amplitude of the peak and the various spot properties. Notice that the y-axis values are not constant for all three plots.

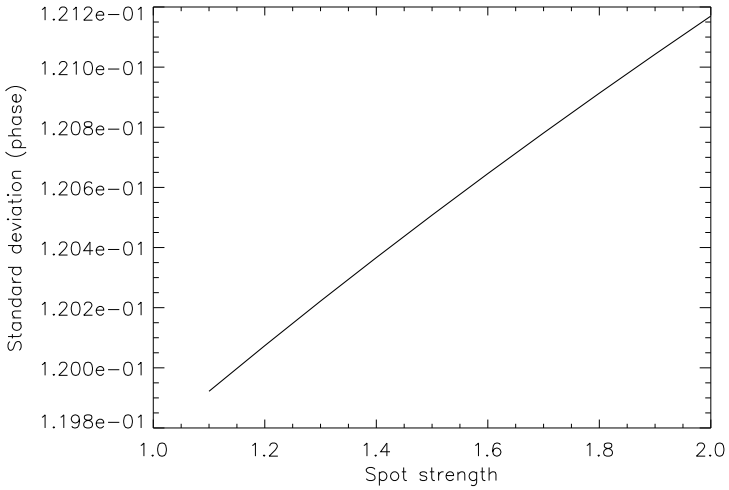

(a) $\sigma_{\rm p}$ vs. A

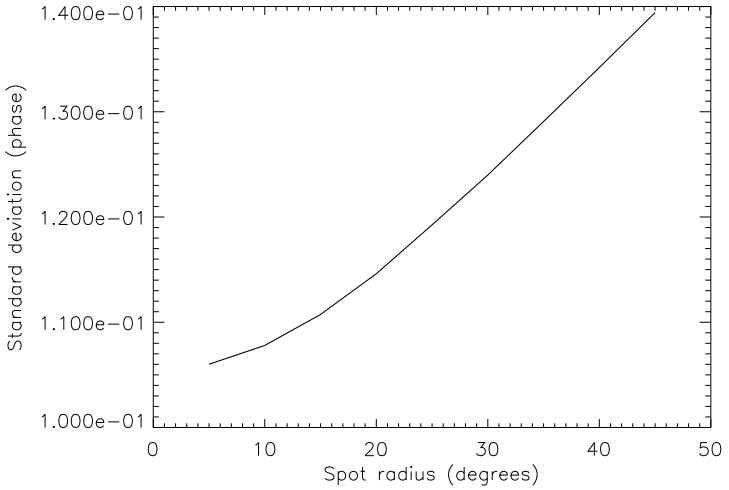

(b) $\sigma_{\rm p}$ vs. r

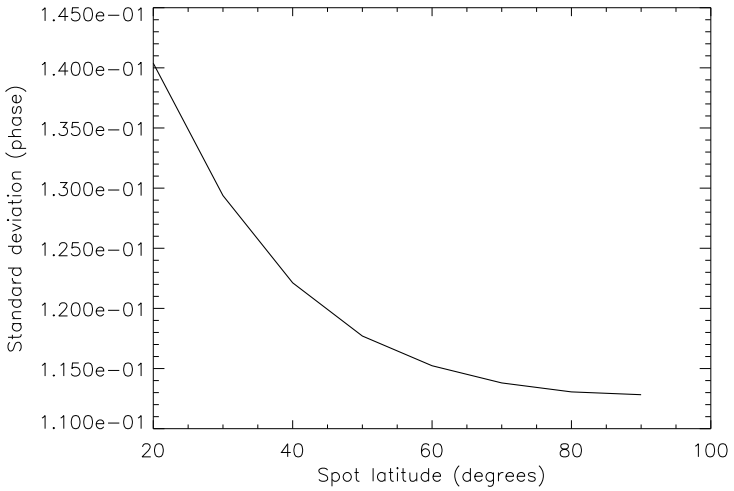

(c) $\sigma_{\rm p}$ vs. $\theta_{\rm s}$

Figure 7.5: Same as Fig. 7.4, but for the standard deviation.

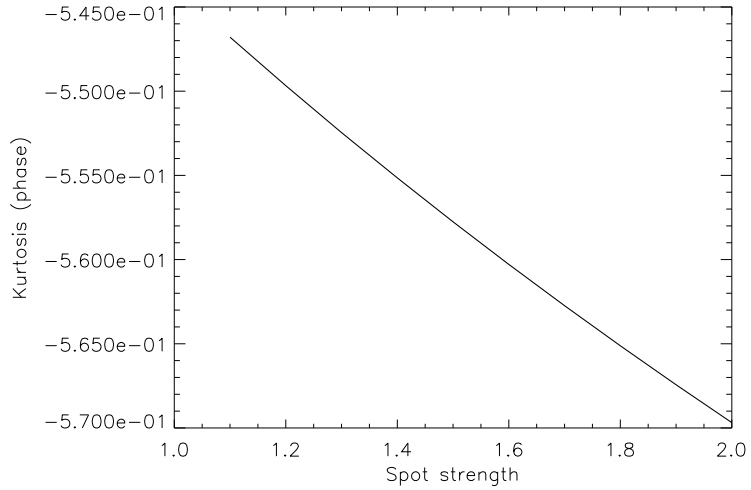

(a) g_2 vs. A

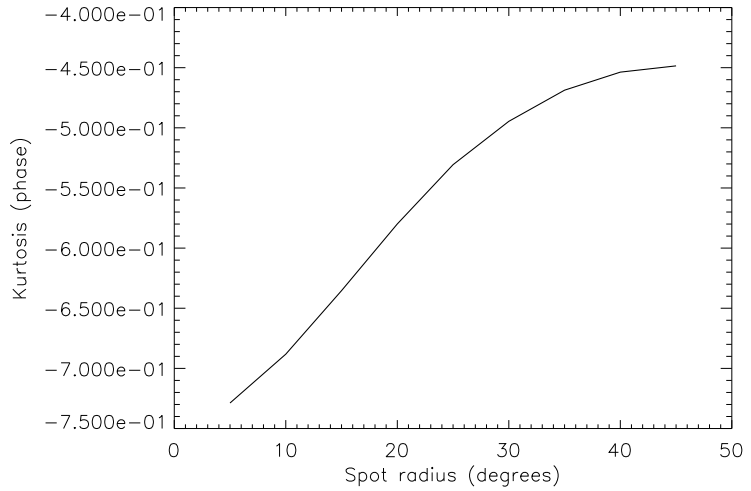

(b) g_2 vs. r

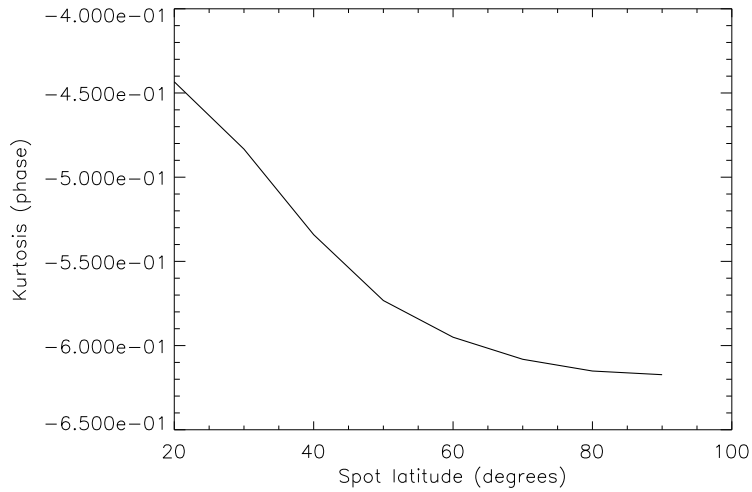

(c) g_2 vs. θ_s

Figure 7.6: Same as Fig. 7.4, but for the excess kurtosis.

$$A(t) = A_0 + bt \tag{7.16}$$

where A_0 corresponds to some initial brightness enhancement, and b is the slope. In the context of the spot generation model and Eq. 7.11, this slope would correspond to:

$$b = \pm\frac{2A_{\max}}{\tau} \tag{7.17}$$

and would be positive when the spot is rising and negative when it is decaying. To illustrate the effect of this linear variation, we generate spot models by fixing all the other spot parameters (we use $A = 1.5$ at phase 0.5, $r = 20°$, $\theta_s = 90°$ and $i = 90°$) and letting the slope vary between -0.2 and 0.2 (in reciprocal phase units). The light curve properties studied earlier ($A_{\rm var}$, $\sigma_{\rm p}$ and g_2) are unaffected by the value of the slope, but this time we also compute the skewness:

$$\gamma_1 = \frac{\sum\limits_i \Delta m_i(\psi_i - \mu)^3}{\sigma_{\rm p}^3 \sum\limits_i \Delta m_i} \tag{7.18}$$

As we can see in Fig. 7.7, the skewness depends directly on the value of the slope. Even though this effect is subtle, it could play an important role in assessing the validity of the assumption made in the spot generation model and help paint a clearer picture of the evolution of bright spots over the course of their lifetime, thus perhaps allowing us to refine that assumption.

Finally, we wish to try to recover spot parameters from a realistic light curve. To do so, we use the Metropolis-Hastings implementation of Markov Chain Monte Carlo (MCMC) Bayesian inference [Metropolis et al., 1953, Hastings, 1980]. We

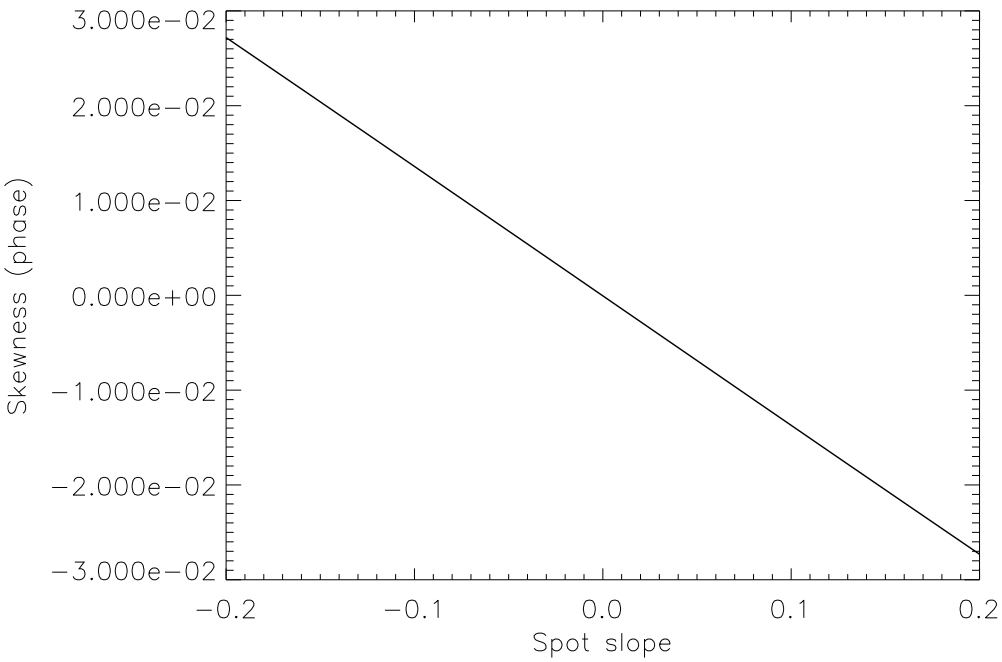

Figure 7.7: Skewness as a function of the brightness enhancement slope.

investigate a three-dimensional parameter space comprising of spot radius, brightness enhancement and spot latitude. First, we generate a synthetic light curve (with 50 different datapoints over a rotational period) using a set of input spot parameters and we add Gaussian noise to it (in this case, we use 0.1 mmag, a typical error bar for a *MOST* light curve of a bright star which was binned per 101-minute orbit, which means that if we considered each phase point of the light curve as being spaced by 101 minutes, the rotational period of the star in question would be about 3.5 days). Then, using MCMC, we try to recover those initial parameters by starting with slightly different parameters. For each step of the algorithm, we use a Gaussian proposal distribution for each parameter (with respective standard deviations of 2°, 10% and 5° for the spot radius, brightness enhancement and spot latitude). As

for the priors, we use a flat prior for the spot radius (which we let vary between 0° and 45°), a Jeffreys' prior for the "excess brightness" (which corresponds to $A-1$, where we subtract unity from the brightness enhancement factor to express the spot's relative excess compared to the rest of the stellar surface), and a Gaussian prior for the latitude which is centered around the equator with a 30° standard variation. Finally, we let the code evolve for 5000 iterations.

Unfortunately, it does not seem like it is possible to recover all three parameters solely using the light curve. In particular, it seems like the code cannot resolve the degeneracies that link all three parameters and cannot settle on a single region of higher likelihood, even though the mean parameters yielded are somewhat close to the input parameters. A sample run is shown in Fig. 7.8, and similar behaviour is observed for various input spot parameters. It should also be noted that the priors chosen for this investigation seem to be of little consequence since other attempts using different priors similarly struggle to converge to a single solution. Therefore, we conclude that within the framework of this simple model, while it allows us to constrain single spot properties, photometry alone cannot yield a unique solution.

This does not however constitute a failure of our model. Even though they have yet to be detected, the spectroscopic signatures that we predict could help lift this degeneracy. We illustrate this by using three sets of spot parameters that lead to roughly the same amplitude of photometric variations (as shown in Fig. 7.9 and then compare the effect of these different spot parameters on the line profile variations in Fig. 7.10. These figures show very convincingly that the degeneracy that exist in the photometric signal can be lifted using the spectroscopic signatures of these spots.

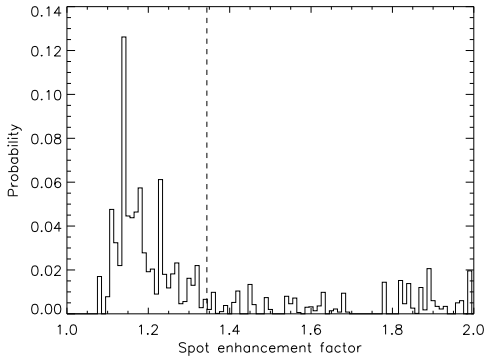

(a) Histogram of A values

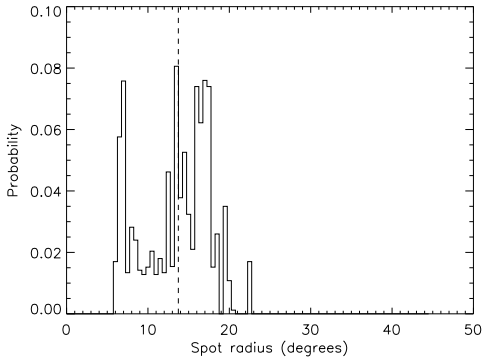

(b) Histogram of r values

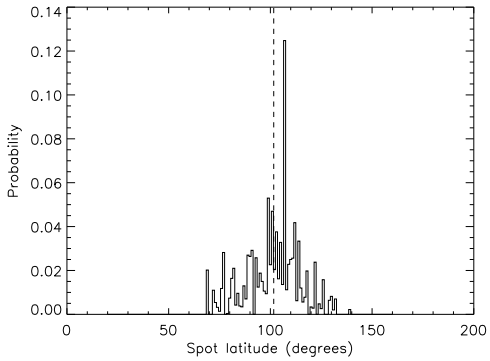

(c) Histogram of θ_s values

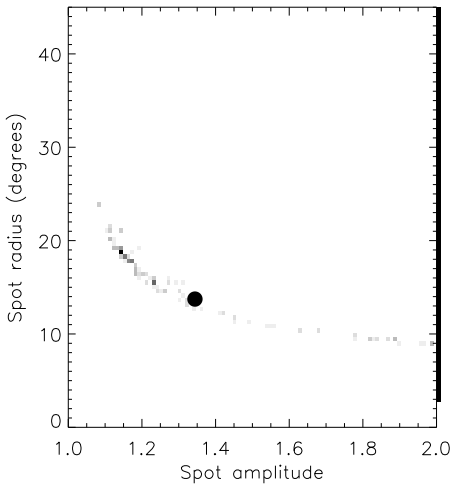

(d) 2D histogram in the A vs. r plane

Figure 7.8: Sample results of the MCMC method described above, using the following input parameters for a single spot model: $A = 1.2$, $r = 15°$ and $\theta_s = 70°$. The first three panels show a histogram of the recovered values for A, r and θ_s, respectively. The dashed lines represent the average value in each case. If the method had yielded better results, we would see probability density functions with a clear, single peak. The last panel shows a 2D histogram in the A vs. r plane, with a large black dot showing the average values; we can clearly see the strong degeneracy between these two parameters as they are not independent.

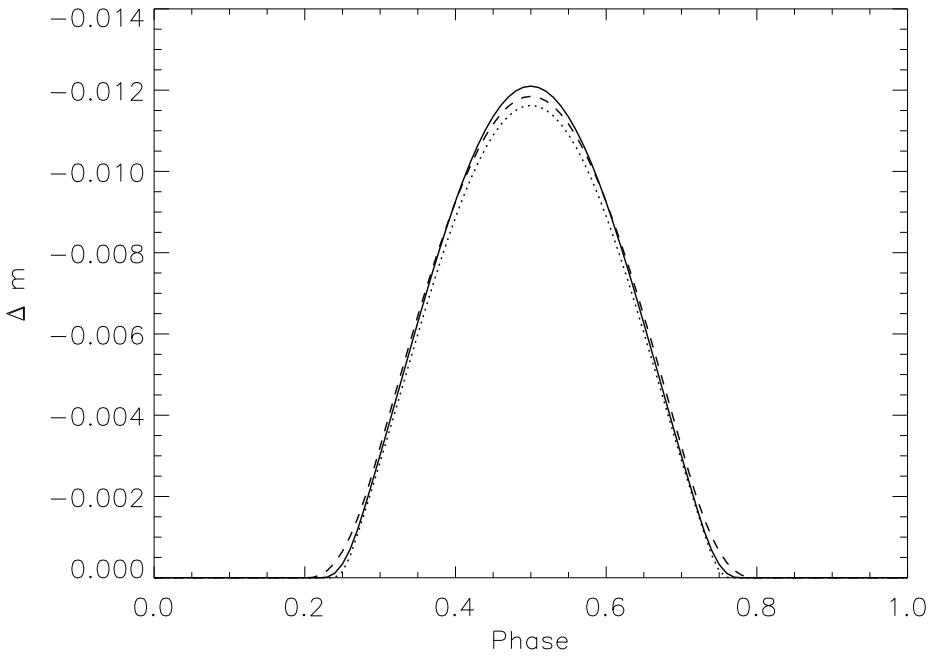

Figure 7.9: Light curves of three different single spot models (using $i = 90°$), all very similar in amplitude and shape. *Plain:* $A = 1.33$, $r = 10°$ and $\theta_s = 90°$; *Dotted:* $A = 2.32$, $r = 5°$ and $\theta_s = 90°$; *Dashed:* $A = 1.66$, $r = 10°$ and $\theta_s = 35°$.

7.5 Modelling evolving spots on ξ Persei

To reproduce the qualitative behaviour of ξ Persei's periodogram as shown by Ramiaramanantsoa et al. [2014], we finally use our spot generation model. Using the individual values of the parameters derived in their study (in the 12-spot model, their *model 1*), we estimate reasonable average parameters and their standard deviations for our model. However, challenges arise from using the reported 4.18-d period. In particular, we cannot manage to obtain the right relative power between the peaks around 0.25 c/d and the peaks around 0.5 c/d; we always seem to recover stronger periods around the rotational frequency instead of the DAC recurrence frequency (the

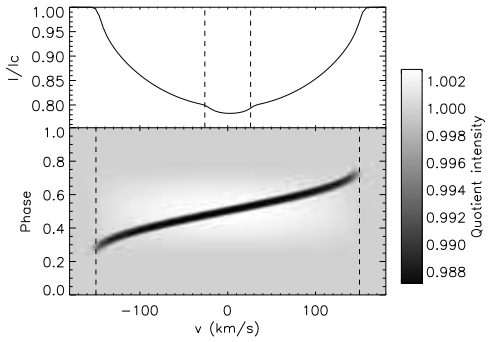

(a) Spectroscopic variations in "plain" model

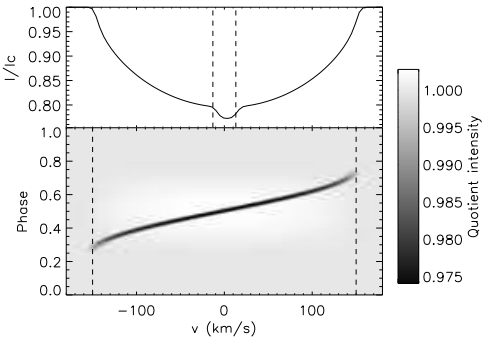

(b) Spectroscopic variations in "dotted" model

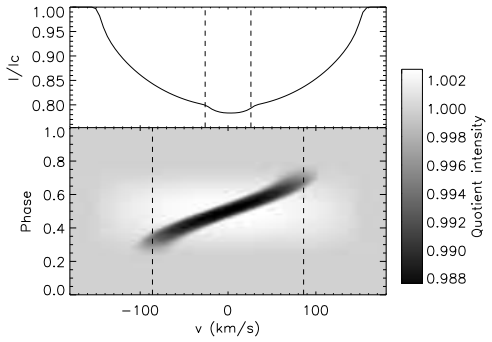

(c) Spectroscopic variations in "dashed" model

Figure 7.10: Similarly to Fig. 7.3, we produce simplified spectroscopic timeseries but this time using the same three single spot models as in Fig. 7.9. In the top panel, we now only plot the feature at phase 0.5, corresponding to when the spot is in the center of the line of sight. Furthermore, we have added dashed lines in the top panel corresponding to $\pm v \sin i \sin r$ as well as dashed lines in the bottom panel at $\pm v \sin i \sin \theta$. These show quite convincingly that the radius and latitude of the spot can be recovered directly using spectroscopy; the amplitude of the variation relative to the unperturbed profile also changes as a function of A and $\theta_{\rm s}$.

Table 7.1: List of input parameters for our spot evolution code; we show both the average value and its assumed standard deviation. The parameters are A, the spots' brightness enhancement, r, their angular radius, $\theta_{\rm s}$, their latitude, τ, their lifetime and finally $t_{\rm gen}$, the timescale between the appearance of two consecutive spots.

Parameter (X)	Average value ($\langle X \rangle$)	Assumed standard deviation (σ_X)
A	1.24	0.06
r (°)	10.0	2.0
$\theta_{\rm s}$ (°)	90.0	20.0
τ (d)	9.39	6.24
$t_{\rm gen}$ (d)	2.16	1.56

prevalent frequency in the data). However, the light curve that we generate does seem to reproduce the general qualitative features of ξ Persei's. The results are shown in Fig. 7.11 (synthetic light curve) and Fig. 7.12 (corresponding periodogram, computed using PERIOD04, Lenz and Breger 2005), with the list of parameters the we use shown in Table 7.1.

Finally, we use a "biased" spot model to attempt to resolve this issue. Instead of randomly assigning a longitude to each spot, we force the spots to be essentially diametrically opposed by introducing a Gaussian longitude bias centered around 180°. We compute the periodogram of the synthetic light curve of this model, the result of which is shown in Fig. 7.13; while the peak near the rotational frequency still dominates, the one around 0.5 c/d is now much stronger, and more in line with what is seen in the observed light curve of ξ Persei. Note that we are not looking to produce a detailed fit of the observational periodogram, but rather reproduce its qualitative features. In that regard, the biased spot model can be considered as being much more successful.

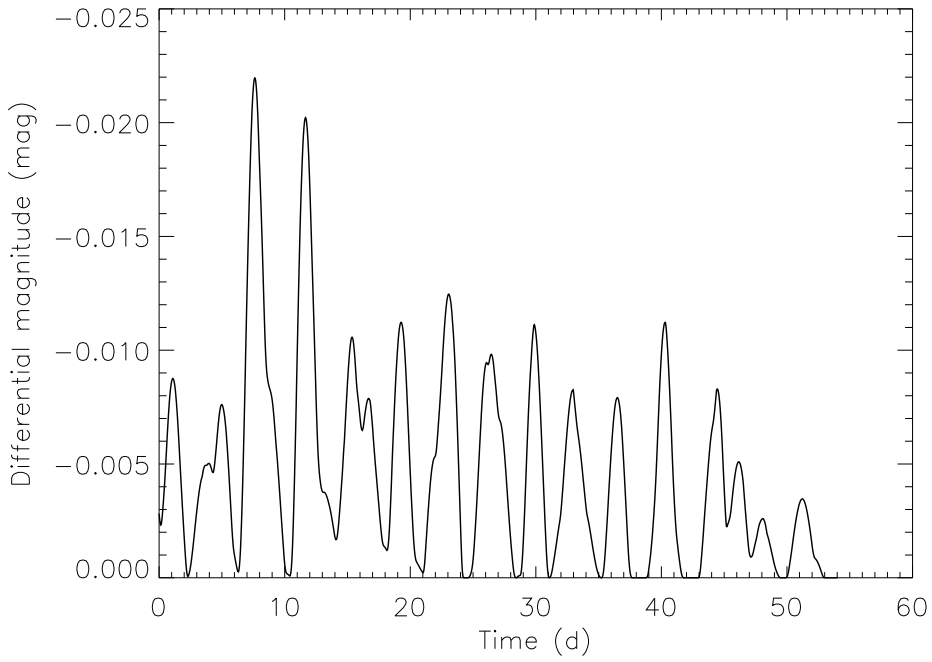

Figure 7.11: Synthetic light curve generated using our spot generation model to try to reproduce the qualitative features of ξ Persei's light curve.

7.6 Conclusions and future work

In conclusion, we have presented a new model which allows us to generate both synthetic light curves and photospheric dynamic spectra using co-rotating bright spots on the surface of a star. We have shown that while our model does not allow us to reliably recover spot properties using solely photometry due to degeneracy, spectroscopic signatures of bright spots in photospheric lines should allow us to lift that degeneracy; however, the effect of multiple spots on line profile variations should be further investigated. It might also be possible to take advantage of high-precision multi-colour photometry (in a similar way to, e.g., Eker 1996) such as is available using BRITE-Constellation [Weiss et al., 2014]; in that case we would derive different

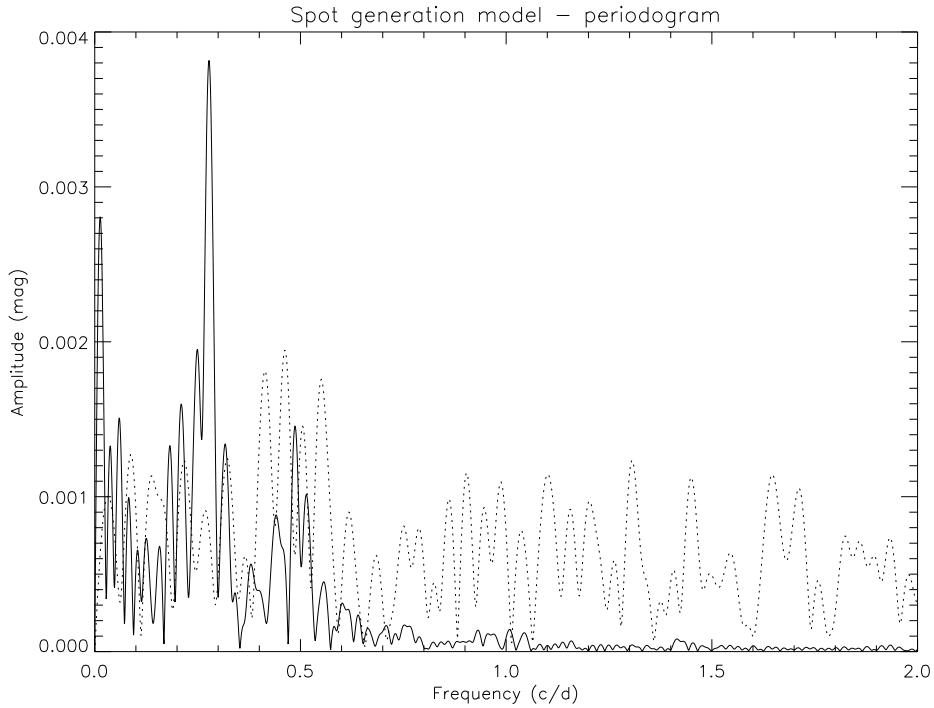

Figure 7.12: Periodogram of the light curve shown in Fig. 7.11. The dotted line represents the periodogram of the 2011 MOST observations of ξ Persei (it should be noted that frequencies beyond about 0.8 c/d are not significant in that data according to Ramiaramanantsoa et al. [2014]).

values of A for each bandpass based on the temperature of the spots relative to the temperature of the unperturbed surface.

Of course, more sophisticated methods can be used to image the stellar surface (e.g., light-curve inversion using photometry, Harmon and Crews 2000; or Doppler imaging using high-cadence high-resolution spectroscopy, Vogt and Penrod 1983) and present the advantage of being model-independent, but in our case, this simple parametrized model allows us to explore the consequences of the BSP within a larger framework including ultraviolet line profile variations [David-Uraz et al., in prep.] and to trace the evolution of these features.

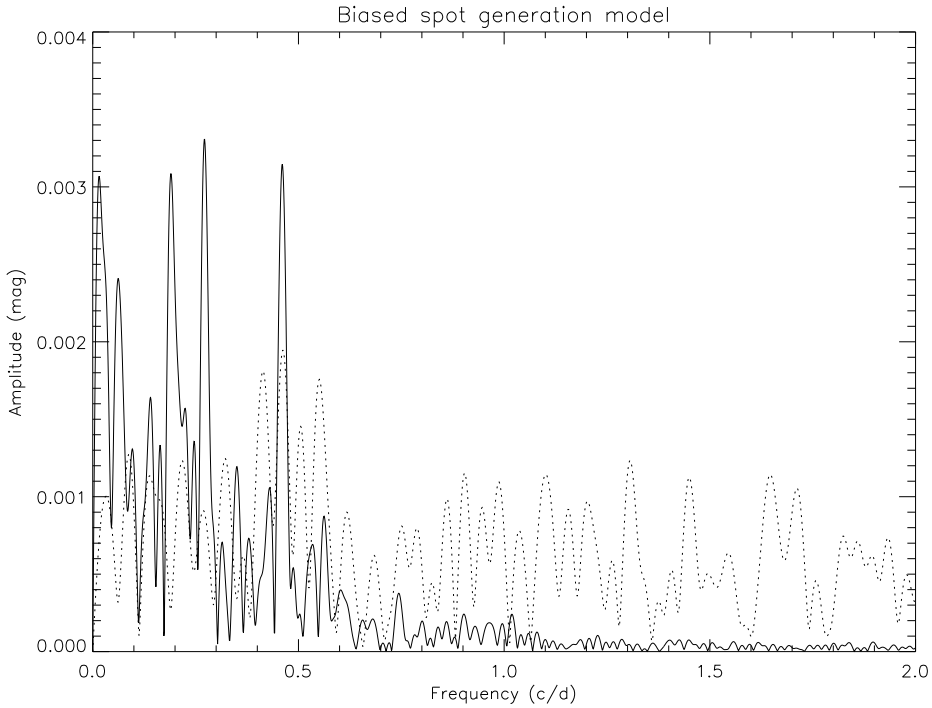

Figure 7.13: Same as Fig. 7.12, but using the biased spot model; the peak at about 0.5 c/d is now much more prominent, which is more in line with what is seen in the observational periodogram (dotted).

Another valuable result yielded by this model is the spectroscopic pattern of variability. However, it should be noted that non-radial pulsations can perhaps produce similar variations (e.g., Schrijvers et al. 1997).

Finally, our spot generation model can be used to calculate a large number of synthetic light curves given a variety of spot evolution parameters in a reasonable amount of time; this would be invaluable in building a statistically significant sample to study the possible cross-talk between pulsational and "spotty" models. Its assumptions can be easily tweaked based on future observational constraints. The comparison of synthetic light curves produced using this model and the light curve of ξ Persei also leads to intriguing results. Assuming the validity of our model, either the

rotational period adopted by Ramiaramanantsoa et al. [2014] is wrong (which would be surprising, especially since it would prove difficult to explain longer periods), or our results suggest that while we are investigating the behaviour of small-scale photometric perturbations, some heretofore unknown phenomenon causes these structures to follow a large scale distribution, appearing preferentially at specific positions on the stellar surface with respect to each other. This is reminiscent of the existence of "active longitudes" in the Sun: regions within which most sunspots appear (e.g., Usoskin et al. 2005). Further work will be necessary to understand what could cause such a distribution.

Acknowledgments

This research has made use of NASA's Astrophysics Data System (ADS) Bibliographic Services.

ADU gratefully acknowledges the support of the *Fonds québécois de la recherche sur la nature et les technologies*, as well as the useful guidance of Matthew Shultz.

GAW is supported by an NSERC Discovery Grant.

The authors thank Tahina Ramiaramanantsoa for sharing the MOST 2011 observations of ξ Persei.

Chapter 8

Conclusions and future work

Discrete absorption components, believed to be ubiquitous in hot, massive stars, might hold the key to gaining a better understanding of the photospheric and wind physics of these stars. They are believed to be indicative of large-scale azimuthal structures (CIRs) in the stellar wind, and the best models currently available indicate that these structures must originate from perturbations at the surface of the star. This thesis has focussed on constraining the physical phenomena that might be responsible for these perturbations using observations and numerical simulations.

8.1 Summary

Three separate studies constraining the origin of DACs have been presented in the context of this thesis.

The first study aimed to evaluate the possible role of dipolar, large-scale magnetic fields in creating DACs. To do so, high quality spectropolarimetric observations (obtained with ESPaDOnS@CHFT and NARVAL@TBL) of 13 stars with well-studied,

ultraviolet spectroscopic timeseries which unambiguously exhibit DACs, were analyzed to yield tight magnetic constraints. Longitudinal field measurements were constitent with a null magnetic fields for all 13 stars. Furthermore, assuming the would-be fields to be dipolar, Bayesian inference allowed the calculation of firm upper limits on their strength. These limits were then evaluated in light of two different scenarios which might explain how magnetic fields are linked to DACs: wind confinement and surface brightness enhancements. In the first scenario, the wind is dynamically influenced by the field, which can lead to density structures. In the second scenario, the field changes the structure of the atmosphere, which leads to local perturbations in the wind driving and therefore, indirectly to dynamical effects on the wind outflow as well. The limits on the strength of the dipolar field derived for the sample indicate that statistically, the observations are inconsistent with either of these scenarios.

The second and third studies focussed rather on the phenomenology of the problem. The ad hoc bright spots used in models (e.g., Cranmer and Owocki 1996) to generate CIRs should, in principle, produce measurable effects in a range of observational diagnostics. A first detection of such spots has been claimed by Ramiaramanantsoa et al. [2014] in broadband optical photometric observations of the O giant ξ Persei. However, the amplitude of the associated photometric variations is much smaller than what would have been expected from the bright spots used to model DACs. Therefore, the second study presented in this thesis consisted to update these CIR models using "realistic" bright spots, i.e., spots that would generate variations of similar amplitude to those found in the ξ Persei light curve. The goal was to determine if the spots that were claimed to be detected could also be responsible for the DACs seen in the UV spectra of ξ Persei, or in other words, whether it is possible for

more modest spots to lead to density structures in the wind which in turn produce DACs. Using three different sets of spot sizes and brightness enhancements, models were computed with the VH-1 hydrodynamics code (and the *gcak3d* routine to compute radiative forces) which not only proved that modest spots could lead to DACs, but that using the constraints obtained from photometry, we could model CIRs which produce DACs that are quantitatively similar to those observed in ξ Persei.

Finally, the third study presented numerical tools to predict observational signatures that are consistent with the bright spot paradigm in both broadband optical photometry and optical spectroscopy (more specifically, the profiles of photospheric lines). This provides not only a test of the existence of such bright spots on the surfaces of massive stars, but also the means to characterize the spots if they are detected. An iteration on the spot modelling performed by Ramiaramanantsoa et al. [2014] allows spots to appear and disappear arbitrarily over the course of a few stellar rotation periods and produces associated synthetic light curves and dynamic spectra. Preliminary results reveal that a bias in the longitude at which the spots appear leads to a better agreement between the periodograms of the synthetic and observed light curves of ξ Persei.

8.2 Conclusions

The first main conclusion of this work is that large-scale dipolar magnetic fields are not responsible for DACs. Indeed, since the constraints obtained on the field strength indicate that neither wind confinement nor brightness enhancements can be invoked as a mechanism for dipoles to dynamically influence the wind, therefore dipoles do not constitute a viable option. In Chapter 1, we have presented three leading hypotheses

regarding the physical cause of DACs: large-scale dipolar magnetic fields, small-scale magnetic fields and non-radial pulsations. Therefore, only the last two remain.

This thesis established the first direct link between constraints derived from optical photometry and signatures observed in UV line profiles. The fact that the synthetic spectra not only show evidence of DACs, but specifically show DACs that are quantitatively very similar to those observed in the UV spectra of ξ Persei supports the idea that the BSP can be used to consistently model variations in both of these observational diagnostics, which is significant.

Finally, it presents tools which have been developed to further investigate the observational consequences of the BSP. These tools allow us to make quantitative predictions about the signatures of bright spots in broadband optical photometry and photospheric line profiles. The possible bias in longitude which is reported to explain the periodogram of the ξ Persei light curve is of particular interest since it is reminiscent of the discovery of "active longitudes" in the Sun and other active low-mass stars. If co-rotating bright spots really exist on the surfaces of OB stars, then this bias could be telling us something fundamental about the mechanism which creates these spots.

In conclusion, this thesis has helped constrain the magnetic hypothesis significantly and contains tools to interpret and analyze various observational diagnostics in light of the BSP. This analysis provides additional constraints on the physical cause for these surface brightness perturbations, e.g., putative magnetic spots. If magnetic spots exist, then this work should help link them to the current observations; if they do not, then this work contains the basis with which they can be ruled out. Therefore, in one case or another, this thesis will have brought us much closer to understanding

the origin of discrete absorption components.

8.3 Future work

Since large-scale dipolar magnetic fields are ruled out as a possible origin for DACs, observational efforts should focus on the other scenario involved in the magnetic hypothesis: small-scale fields. As mentioned in Chapter 2, such fields are postulated as arising from the subsurface convection zone due to the iron opacity bump (FeCZ). Dynamo action in the FeCZ could create small magnetic loops which would then advect to the surface, creating magnetic spots, not unlike those found on the solar surface. However, since the atmosphere of a massive star is radiative, the spots would be overluminous since the magnetic pressure within the flux tubes would decrease the gas pressure, to conserve hydrostatic equilibrium, and therefore allow us to "see" deeper into the star, probing higher temperature regions (which of course, appear brighter). Therefore, such spots could act as drivers for CIRs, leading to DACs in the UV spectra.

8.3.1 Placing constraints on randomly-distributed spots

Using simulated spectropolarimetric data and typical SNR from MiMeS data, Kochukhov and Sudnik [2013] have placed constraints on the detectability of randomly-distributed magnetic spots given a set of parameters: projected rotational velocity, spot size and strength, and filling factor. However, such constraints have yet to be derived for actual data. A preliminary test using data for 10 Lacertae has yielded some constraints, which are summarized in Fig. 8.1. The highlight of this analysis is that for 10° spots with a filling factor of 48%, the best case scenario would allow us to rule out fields of

over 200 G.

This analysis can then be performed for the entire MiMeS OB star sample, to obtain a statistical basis for these constraints within that class of stars. Regularization[1] can also be applied when the LSD is performed to improve the SNR and obtain tighter limits. This is one of the follow-up projects which will be considered as an extension to this thesis.

8.3.2 Ultra-deep magnetometry of the early-B supergiant ϵ Orionis

Another project of interest involves acquiring ultra-high SNR spectropolarimetric observations of ϵ Ori. This target is of particular interest since it has a fairly low projected rotational velocity and it is very bright. Since the paradigm within which spots might be able to create CIRs involves isolated spots rather than randomly-distributed spots, as seen in Chapters 6 and 7, they might be somewhat easier to detect than what is predicted by Kochukhov and Sudnik [2013]. An integrated approach involving photometric, spectroscopic and polarimetric monitoring of the star over a period comparable to the rotational period would yield the best chance at a detection, should magnetic spots exist. While 3 unsuccessful proposals have been submitted to CFHT to perform these observations (and rejected for reasons outside of our control, e.g., the MOST space telescope decommissioning announced during TAC deliberations in 2014, when part of our proposal relied on simultaneous observations with MOST), there still is hope that we could obtain observations deep enough to reach the parameter space of interest.

[1] This corresponds roughly to a smoothing of the profile that can yield gains in SNR but must be used carefully to avoid introducing spurious signatures in Stokes V [Kochukhov et al., 2010].

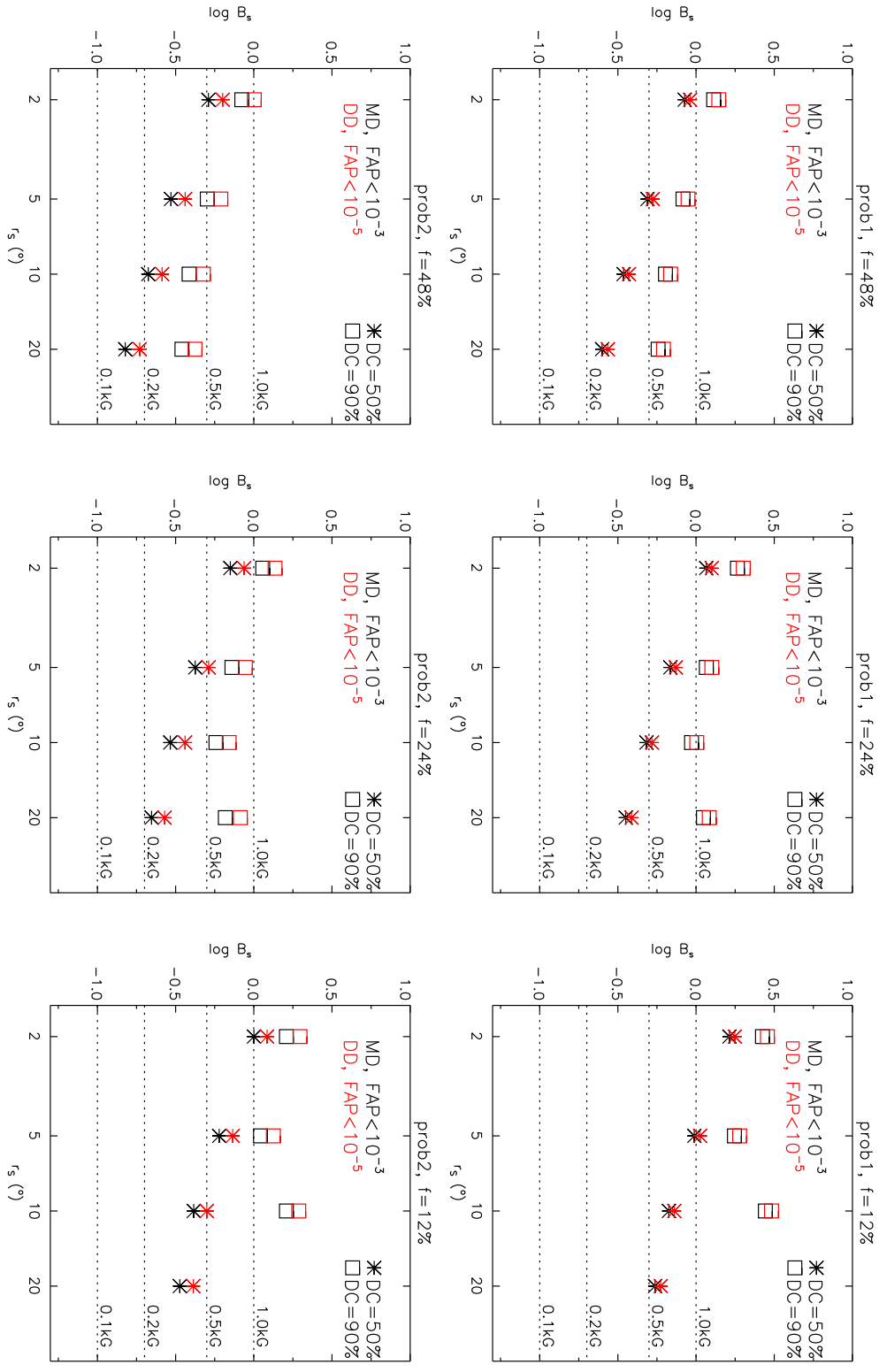

Figure 8.1: Constraints for 6 different models. "prob1" models use the Stokes V signal, while "prob2" models also add the diagnostic null. The filling factors used are $f = \{12\%, 24\%, 48\%\}$. For each model, constraints are derived for a "detection chance" (DC) of 50% or 90%, and for marginal detections (MD) as well as definite detections (DD).

Table 8.1: List of new models used in this study; the parameters are the same as in Table 6.1.

Model	r (°)	A	δ
4A	5	0.08	0
4B	5	0.08	0.1
5A	5	0.33	0
5B	5	0.33	0.1
6A	10	0.08	0
6B	10	0.08	0.1
7A	10	1.32	0
7B	10	1.32	0.1
8A	20	0.33	0
8B	20	0.33	0.1
9A	20	1.32	0
9B	20	1.32	0.1

8.3.3 Further hydrodynamic modelling and more accessible observational diagnostics

As a follow-up to the study presented in Chapter 6, a first natural extension that can be made is to the parameter space of interest. While this study was specifically designed to reproduce the variability in ξ Persei, there is no reason not to try to reproduce a larger range of phenomena. As a first effort, we use the same values of brightness enhancement and spot radius, but no longer require spots to respect the 10 mmag photometric variability amplitude. Thus, we now probe a 3x3 grid of parameters. The parameters of the new models are shown in Table 8.1. Sample results for models 9A and 9B are shown in Fig. 8.2 and Fig. 8.3.

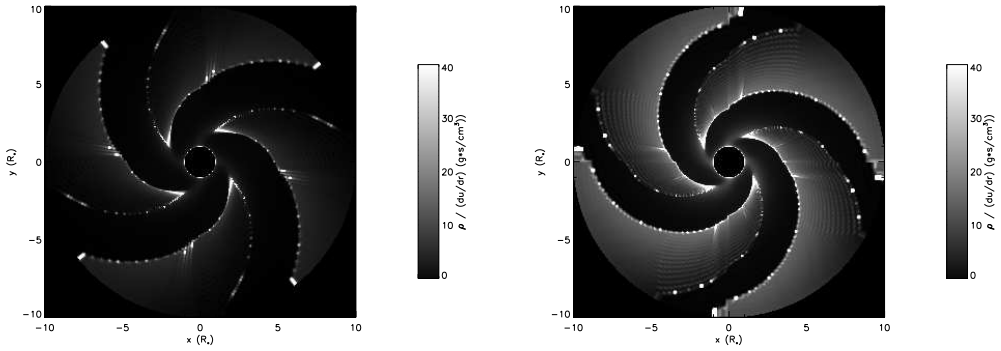

(a) Model 9A (b) Model 9B

Figure 8.2: Same as Fig. 6.5, but for models 9A and 9B.

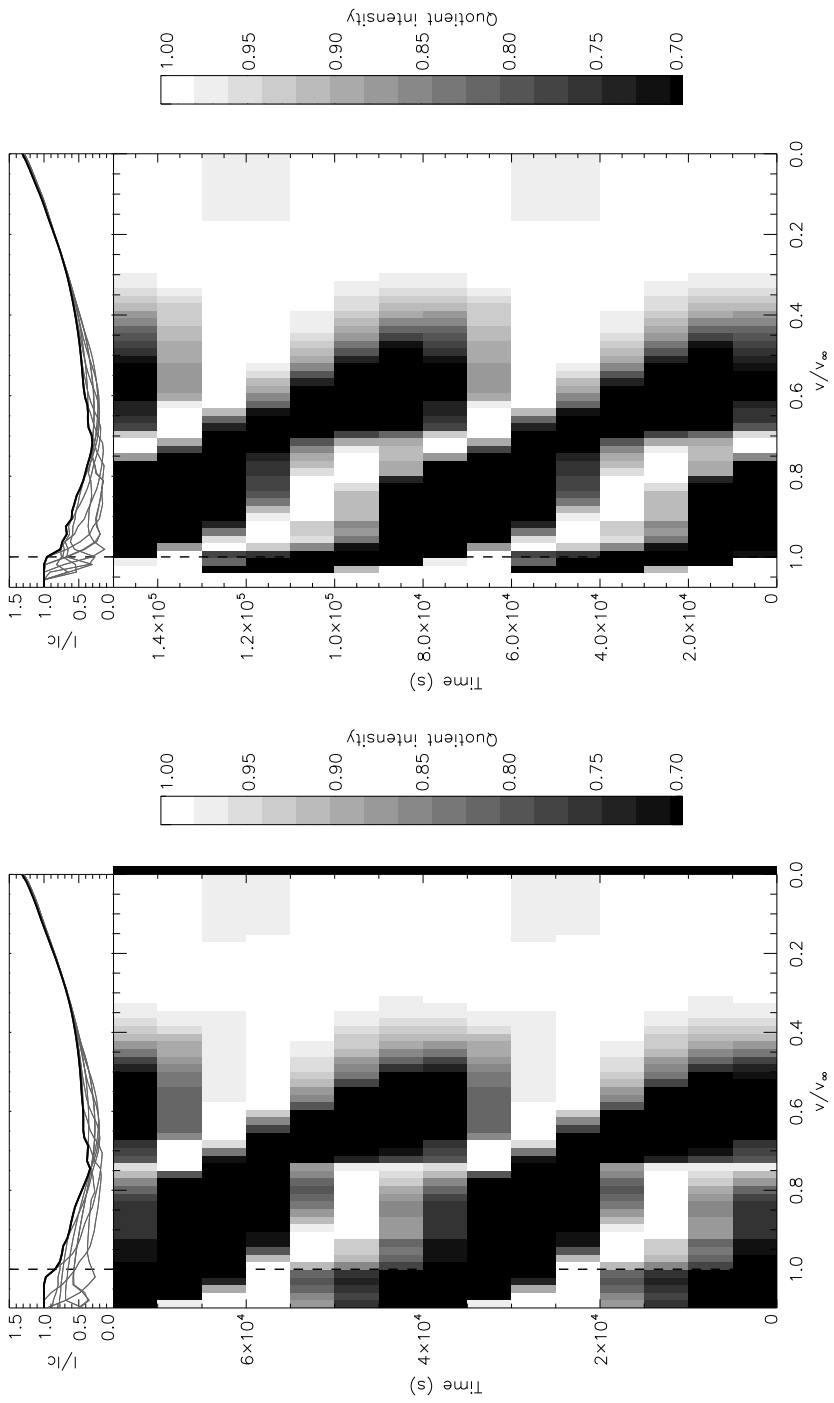

(b) Model 9B synthetic line profile.

(a) Model 9A synthetic line profile.

Figure 8.3: Same as Fig. 6.6, but for models 9A and 9B.

The optical depth figures show that the wind is not as locally overloaded as the wind in models 1A and 1B, because even though the spots have the same brightness contrast, 20° spots can sustain the additional driving over a longer distance. However, we can also see that the DACs are much deeper then usual, and have an unexpected shape (although that might be due to insufficient time resolution, leading to a bad evaluation of the least-absorption profile). Further analysis is required to better interpret this extreme case.

The distribution of the spots on the stellar surface could also be investigated, as well as the effect of brightness evolution in spots with finite lifetimes on the stability of the wind structures that they generate.

Another important improvement would be the synthesis of lines that can be more easily observed and for which timeseries can be readily obtained, in this case, the Hα line. Kaper et al. [1997] have shown that DAC behaviour is correlated with variations in Hα. Using a method developed by [Puls et al., 1996] and refined by [Sundqvist et al., 2012], initial tests performed on model 2B seem to show some weak variability. The resulting quotient spectra are shown in Fig. 8.4. Further investigation is needed, but this diagnostic might provide a much needed additional insight into the types of spots that produce CIRs.

8.3.4 Spots versus pulsations

As outlined in the conclusion of Chapter 7, some important follow-up studies must be performed in order to assess the validity of this model. On one hand, the predictions involving photospheric lines should be verified using timeseries of spectroscopic observations. Such datasets have been acquired for 4 OB stars in Orion (ϵ Ori, κ Ori, λ

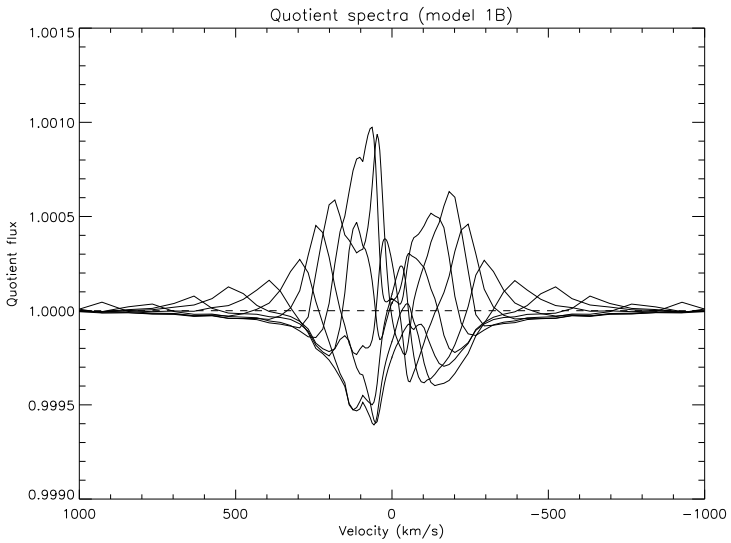

Figure 8.4: Hα profiles generated at 7 different rotational phases and divided out by a mean spectrum. The results shown were generated from the hydrodynamic simulations of model 2B.

Ori and ζ Ori A) and will be analyzed to that effect. However, one possible problem in recovering these signatures, should they exist, is not only their small amplitude, but mostly the fact that there exist a few sources of line profile variability (LPV) in massive stars, which might be difficult to disentangle from the effect of spots. However, if such a feat is possible, small absorption bumps evolving along the line profile would give us a lot of information about the spots from which they originate (in the best case scenario, Doppler imaging could be performed, leading to detailed surface brightness maps).

Another important problem that must be assessed is that of pulsational vs. "spotty" light curves. There currently exists a divide within the massive star community when it comes to interpreting complex and somewhat puzzling light curves and behaviours

in OB stars. While some would explain everything in terms of pulsations and asteroseismology, others are inclined to interpret departures from the pulsational models as a "clear" indication of the presence spots. A good way to evaluate that position would be to quantify, in a statistically significant way, what amount of cross-talk there might be between both families of models, or in other words, how well could a synthetic light curve, generated using a purely pulsational model, be understood in terms of spots, and vice versa. Thankfully, the spot generation model developed in Chapter 7, while perhaps not in its final form (it could always be tweaked to take into account any new information that would come to light regarding the evolution of bright spots), can generate a large number of synthetic light curves in a short amount of time, thereby greatly facilitating the latter.

8.3.5 Magnetohydrodynamic simulations

While the connection between magnetic spots and CIRs has focussed so far on the idea that the spots would be overluminous, further modelling must first determine whether or not these spots' field would have any important dynamical effect on the winds. One possibility would be that they would confine a small amount of material to form "prominences" at the stellar surface [Henrichs and Sudnik, 2014]. What effect, if any, that would have on the formation of CIRs is, at best, unclear at this point. It is thus paramount to conduct MHD simulations of magnetic spots on massive stars before any firm conclusion can be attained. Current modelling efforts encounter numerical challenges (ud-Doula, priv. comm.) but more concerted efforts should allow us to overcome these problems and gain a clearer picture of this phenomenon.

8.3.6 Non-radial pulsations

Finally, as mentioned previously, a pulsational origin for DACs has not been investigated in the context of this thesis, but should perhaps not be discarded altogether. Even though there are many reasons to be skeptical of this hypothesis (seemingly unreconcilable periods, cyclical vs. periodic behaviour, dark and bright patterns incompatible with observed variability, etc.), it is worth nonetheless investigating, especially if other avenues do not lead us to a better understanding. A first effort should be done to place statistically significant constraints on the pulsational behaviour of stars with well studied DACs, as was done for dipolar magnetic fields, followed by detailed modelling.

All these proposed follow-up studies will serve to answer one question: what photospheric phenomenon, common to all OB stars, is responsible for DACs? This remains a fundamental question which must be addressed if we hope to gain a better understanding of massive stars. This thesis has laid the foundations upon which this important work can be carried out.

Bibliography

D. C. Abbott. The theory of radiatively driven stellar winds. II - The line acceleration. ApJ, 259:282–301, August 1982.

H. M. Al-Naimiy. Linearized limb-darkening coefficients for use in analysis of eclipsing binary light curves. Ap&SS, 53:181–192, January 1978.

H. Alfvén. Existence of Electromagnetic-Hydrodynamic Waves. Nat, 150:405–406, October 1942.

T. Bayes and R. Price. An Essay towards Solving a Problem in the Doctrine of Chances. *Philosophical Transactions of the Royal Society of London*, 53:370–418, 1763.

C. S. Beals. On the nature of Wolf-Rayet emission. MNRAS, 90:202–212, December 1929.

C. S. Beals. On the temperatures of Wolf-Rayet stars and novae. MNRAS, 92: 677–688, April 1932.

A. Blaauw. Massive Runaway Stars. In J. P. Cassinelli and E. B. Churchwell, editors, *Massive Stars: Their Lives in the Interstellar Medium*, volume 35 of *Astronomical Society of the Pacific Conference Series*, page 207, January 1993.

J. M. Blondin and E. A. Lufkin. The piecewise-parabolic method in curvilinear coordinates. ApJS, 88:589–594, October 1993.

J.-C. Bouret, D. J. Hillier, T. Lanz, and A. W. Fullerton. Properties of Galactic early-type O-supergiants. A combined FUV-UV and optical analysis. A&A, 544: A67, August 2012.

J. Braithwaite and Å. Nordlund. Stable magnetic fields in stellar interiors. A&A, 450:1077–1095, May 2006.

A. S. Brun, M. K. Browning, and J. Toomre. Simulations of Core Convection in Rotating A-Type Stars: Magnetic Dynamo Action. ApJ, 629:461–481, August 2005.

M. Cantiello and J. Braithwaite. Magnetic spots on hot massive stars. A&A, 534: A140, October 2011.

M. Cantiello, N. Langer, I. Brott, A. de Koter, S. N. Shore, J. S. Vink, A. Voegler, D. J. Lennon, and S.-C. Yoon. Sub-surface convection zones in hot massive stars and their observable consequences. A&A, 499:279–290, May 2009.

J. I. Castor, D. C. Abbott, and R. I. Klein. Radiation-driven winds in Of stars. ApJ, 195:157–174, January 1975.

P. Charbonneau. *Solar and Stellar Dynamos*. 2010.

A.-N. Chené, A. F. J. Moffat, C. Cameron, R. Fahed, R. C. Gamen, L. Lefèvre, J. F. Rowe, N. St-louis, V. Muntean, A. De La Chevrotière, D. B. Guenther, R. Kuschnig, J. M. Matthews, S. M. Rucinski, D. Sasselov, and W. W. Weiss. WR 110: A Single

Wolf-Rayet Star with Corotating Interaction Regions in its Wind? ApJ, 735:34, July 2011.

Y.-H. Chu. Ring nebulae around massive stars throughout the Hertzsprung-Russell diagram. In K. van der Hucht, A. Herrero, and C. Esteban, editors, *A Massive Star Odyssey: From Main Sequence to Supernova*, volume 212 of *IAU Symposium*, page 585, 2003.

P. Colella and P. R. Woodward. The Piecewise Parabolic Method (PPM) for Gas-Dynamical Simulations. *Journal of Computational Physics*, 54:174–201, September 1984.

S. R. Cranmer and S. P. Owocki. The effect of oblateness and gravity darkening on the radiation driving in winds from rapidly rotating B stars. ApJ, 440:308–321, February 1995.

S. R. Cranmer and S. P. Owocki. Hydrodynamical Simulations of Corotating Interaction Regions and Discrete Absorption Components in Rotating O-Star Winds. ApJ, 462:469, May 1996.

P. A. Crowther, O. Schnurr, R. Hirschi, N. Yusof, R. J. Parker, S. P. Goodwin, and H. A. Kassim. The R136 star cluster hosts several stars whose individual masses greatly exceed the accepted 150M$_{solar}$ stellar mass limit. MNRAS, 408:731–751, October 2010.

M. Cuntz and R. E. Stencel. A stellar evolution paradigm based on specific mass loss and feedback modes. In M. S. Giampapa and J. A. Bookbinder, editors, *Cool*

Stars, Stellar Systems, and the Sun, volume 26 of *Astronomical Society of the Pacific Conference Series*, pages 451–453, 1992.

A. David-Uraz, A. F. J. Moffat, A.-N. Chené, J. F. Rowe, N. Lange, D. B. Guenther, R. Kuschnig, J. M. Matthews, S. M. Rucinski, D. Sasselov, and W. W. Weiss. Using MOST to reveal the secrets of the mischievous Wolf-Rayet binary CV Ser. MNRAS, 426:1720–1730, November 2012.

A. David-Uraz, S. P. Owocki, G. A. Wade, and J. O. Sundqvist. Investigating the origin of cyclical wind variability in hot, massive stars - II. Hydrodynamical simulations of co-rotating interaction regions using realistic spot parameters for the O giant ξ Persei. MNRAS, in prep.

A. David-Uraz, G. A. Wade, V. Petit, A. ud-Doula, J. O. Sundqvist, J. Grunhut, M. Shultz, C. Neiner, E. Alecian, H. F. Henrichs, J.-C. Bouret, and MiMeS Collaboration. Investigating the origin of cyclical wind variability in hot, massive stars - I. On the dipolar magnetic field hypothesis. MNRAS, 444:429–442, October 2014.

J. A. de Jong, H. F. Henrichs, L. Kaper, J. S. Nichols, K. Bjorkman, D. A. Bohlender, H. Cao, K. Gordon, G. Hill, Y. Jiang, I. Kolka, N. Morrison, J. Neff, D. O'Neal, B. Scheers, and J. H. Telting. A search for the cause of cyclical wind variability in O stars. Simultaneous UV and optical observations including magnetic field measurements of the O7.5III star xi Persei. A&A, 368:601–621, March 2001.

J. A. de Jong, H. F. Henrichs, C. Schrijvers, D. R. Gies, J. H. Telting, L. Kaper, and G. A. A. Zwarthoed. Non-radial pulsations in the O stars XI Persei and lambda Cephei. A&A, 345:172–180, May 1999.

J. C. del Toro Iniesta. *Introduction to Spectropolarimetry*. Cambridge University Press, Cambridge, UK, April 2003.

L. Dessart. 3D hydrodynamical simulations of corotating interaction regions in rotating line-driven stellar winds. A&A, 423:693–704, August 2004.

A. J. Deutsch. Harmonic Analysis of Rigidly Rotating AP Stars. ApJ, 159:985, March 1970.

J. F. Donati. Espadons: the new generation stellar spectropolarimeter, 2008. URL `\url{http://www.ast.obs-mip.fr/projets/espadons/espadons.html}`. [Online; accessed 8 March 2016].

J.-F. Donati, M. Semel, B. D. Carter, D. E. Rees, and A. Collier Cameron. Spectropolarimetric observations of active stars. MNRAS, 291:658, November 1997.

V. Duez and S. Mathis. Relaxed equilibrium configurations to model fossil fields . I. A first family. A&A, 517:A58, July 2010.

A. S. Eddington. *The Internal Constitution of the Stars*. 1926.

Z. Eker. Synthetic Light Curves of Spotted Stars: Unique or Not Unique? ApJ, 473: 388, December 1996.

A. Feldmeier. Time-dependent structure and energy transfer in hot star winds. A&A, 299:523, July 1995.

A. Feldmeier, J. Puls, and A. W. A. Pauldrach. A possible origin for X-rays from O stars. A&A, 322:878–895, June 1997.

A. W. Fullerton. Cyclical Wind Variability from O-Type Stars. In L. A. Balona, H. F. Henrichs, and R. Medupe, editors, *Magnetic Fields in O, B and A Stars: Origin and Connection to Pulsation, Rotation and Mass Loss*, volume 305 of *Astronomical Society of the Pacific Conference Series*, page 333, 2003.

A. W. Fullerton, D. R. Gies, and C. T. Bolton. Detection of small-amplitude pulsations in HD 34656 (O7 II). ApJ, 368:L35–L38, February 1991.

A. W. Fullerton, D. L. Massa, R. K. Prinja, S. P. Owocki, and S. R. Cranmer. Wind variability of B supergiants. III. Corotating spiral structures in the stellar wind of HD 64760. A&A, 327:699–720, November 1997.

K. G. Gayley. An Improved Line-Strength Parameterization in Hot-Star Winds. ApJ, 454:410, November 1995.

D. R. Gies and C. T. Bolton. The binary frequency and origin of the OB runaway stars. ApJS, 61:419–454, June 1986.

D. R. Gies, B. D. Mason, W. G. Bagnuolo, Jr., M. E. Hahula, W. I. Hartkopf, H. A. McAlister, M. L. Thaller, W. P. McKibben, and L. R. Penny. The O-Type Binary 15 Monocerotis Nears Periastron. ApJ, 475:L49–L52, January 1997.

D. F. Gray. *The Observation and Analysis of Stellar Photospheres*. Cambridge University Press, Cambridge, UK, September 2005.

J. H. Grunhut, G. A. Wade, J. O. Sundqvist, A. ud-Doula, C. Neiner, R. Ignace, W. L. F. Marcolino, T. Rivinius, A. Fullerton, L. Kaper, B. Mauclaire, C. Buil, T. Garrel, J. Ribeiro, and S. Ubaud. Investigating the spectroscopic, magnetic

and circumstellar variability of the O9 subgiant star HD 57682. MNRAS, 426: 2208–2227, November 2012.

M. Güdel. X-ray astronomy of stellar coronae. A&A Rev., 12:71–237, September 2004.

G. E. Hale. On the Probable Existence of a Magnetic Field in Sun-Spots. ApJ, 28: 315, November 1908.

W.-R. Hamann. Line formation in expanding atmospheres - On the validity of the Sobolev approximation. A&A, 93:353–361, January 1981.

R. O. Harmon and L. J. Crews. Imaging Stellar Surfaces via Matrix Light-Curve Inversion. AJ, 120:3274–3294, December 2000.

S. M. Haser, D. J. Lennon, R.-P. Kudritzki, J. Puls, A. W. A. Pauldrach, L. Bianchi, and J. B. Hutchings. The stellar wind of an O8.5 I(f) star in M 31. A&A, 295: 136–146, March 1995.

W. K. Hastings. Monte Carlo sampling methods using Markov chains and their applications. *Biometrika*, 57:97–109, July 1980.

A. Heger, C. L. Fryer, S. E. Woosley, N. Langer, and D. H. Hartmann. How Massive Single Stars End Their Life. ApJ, 591:288–300, July 2003.

H. F. Henrichs, G. Hammerschlag-Hensberge, I. D. Howarth, and P. Barr. Episodic mass loss and narrow lines in gamma Cassiopeiae and in other early-type stars. ApJ, 268:807–824, May 1983.

H. F. Henrichs, L. Kaper, and J. S. Nichols. The extent of variability in the stellar wind of the O7.5 giant ξ Persei. A&A, 285:565–572, May 1994.

H. F. Henrichs and N. P. Sudnik. "Stellar Prominences" on OB starsto explain wind-line variability. In P. Petit, M. Jardine, and H. C. Spruit, editors, *IAU Symposium*, volume 302 of *IAU Symposium*, pages 280–283, August 2014.

D. J. Hillier, R. P. Kudritzki, A. W. Pauldrach, D. Baade, J. P. Cassinelli, J. Puls, and J. H. M. M. Schmitt. The 0.1-2.5-KEV X-Ray Spectrum of the O4F-STAR Zeta-Puppis. A&A, 276:117, September 1993.

I. D. Howarth, C. T. Bolton, R. A. Crowe, D. C. Ebbets, M. S. Fieldus, A. W. Fullerton, D. R. Gies, D. McDavid, R. K. Prinja, A. H. N. Reid, S. N. Shore, and K. C. Smith. Time-Series Observations of O Stars. III. IUE and HST Spectroscopy of zeta Ophiuchi and Implications for the "Photospheric Connection". ApJ, 417: 338, November 1993.

I. D. Howarth and R. K. Prinja. The stellar winds of 203 Galactic O stars - A quantitative ultraviolet survey. ApJS, 69:527–592, March 1989.

I. D. Howarth, R. K. Prinja, and D. Massa. The IUE MEGA Campaign: The Rotationally Modulated Wind of zeta Puppis. ApJ, 452:L65, October 1995.

I. D. Howarth, K. W. Siebert, G. A. J. Hussain, and R. K. Prinja. Cross-correlation characteristics of OB stars from IUE spectroscopy. MNRAS, 284:265–285, January 1997.

S. Hubrig, M. Schöller, I. Ilyin, N. V. Kharchenko, L. M. Oskinova, N. Langer, J. F. González, A. F. Kholtygin, M. Briquet, and Magori Collaboration. Exploring the

origin of magnetic fields in massive stars. II. New magnetic field measurements in cluster and field stars. A&A, 551:A33, March 2013.

H. Jeffreys. *Theory of Probability*. Oxford University Press, Oxford, UK, 1998.

M.-B. Kallenrode. *Space physics : an introduction to plasmas and particles in the heliosphere and magnetospheres*. 2004.

L. Kaper, H. F. Henrichs, A. W. Fullerton, H. Ando, K. S. Bjorkman, D. R. Gies, R. Hirata, E. Kambe, D. McDavid, and J. S. Nichols. Coordinated ultraviolet and Hα spectroscopy of bright O-type stars. A&A, 327:281–298, November 1997.

L. Kaper, H. F. Henrichs, J. S. Nichols, L. C. Snoek, H. Volten, and G. A. A. Zwarthoed. Long- and short-term variability in O-star winds. I. Time series of UV spectra for 10 bright O stars. A&AS, 116:257–287, April 1996.

L. Kaper, H. F. Henrichs, J. S. Nichols, and J. H. Telting. Long- and short-term variability in O-star winds. II. Quantitative analysis of DAC behaviour. A&A, 344: 231–262, April 1999.

A. Kaufer, R. K. Prinja, and O. Stahl. Evidence for a connection between photospheric and wind structure in HD 64760. A&A, 382:1032–1041, February 2002.

N. D. Kee. Radiative Ablation of Disks Around Massive Stars. *ArXiv e-prints*, December 2015.

O. Kochukhov, V. Makaganiuk, and N. Piskunov. Least-squares deconvolution of the stellar intensity and polarization spectra. A&A, 524:A5, December 2010.

O. Kochukhov and N. Sudnik. Detectability of small-scale magnetic fields in early-type stars. A&A, 554:A93, June 2013.

O. P. Kochukhov. Spectrum synthesis for magnetic, chemically stratified stellar atmospheres. In I. I. Romanyuk, D. O. Kudryavtsev, O. M. Neizvestnaya, and V. M. Shapoval, editors, *Physics of Magnetic Stars*, pages 109–118, 2007.

M. Kopecký and P. Kotrč . Electric Conductivity in the Atmosphere of Early-Type Stars. *Bulletin of the Astronomical Institutes of Czechoslovakia*, 24:39, 1973.

P. Kroupa. On the variation of the initial mass function. MNRAS, 322:231–246, April 2001.

J. Krtička and J. Kubát. Comoving frame models of hot star winds. I. Test of the Sobolev approximation in the case of pure line transitions. A&A, 519:A50, September 2010.

F. G. Kupka, T. A. Ryabchikova, N. E. Piskunov, H. C. Stempels, and W. W. Weiss. VALD-2 – The New Vienna Atomic Line Database. *Baltic Astronomy*, 9:590–594, 2000.

H. J. G. L. M. Lamers, M. Cerruti-Sola, and M. Perinotto. The 'SEI' method for accurate and efficient calculations of line profiles in spherically symmetric stellar winds. ApJ, 314:726–738, March 1987.

H. J. G. L. M. Lamers and C. Leitherer. What are the mass-loss rates of O stars? ApJ, 412:771–791, August 1993.

L. D. Landau and E. M. Lifshitz. *Fluid mechanics*. 1959.

E. Landi Degl'Innocenti and M. Landolfi, editors. *Polarization in Spectral Lines*, volume 307 of *Astrophysics and Space Science Library*, August 2004.

J. D. Landstreet and E. F. Borra. The magnetic field of Sigma Orionis E. ApJ, 224: L5–L8, August 1978.

P. Lenz and M. Breger. Period04 User Guide. *Communications in Asteroseismology*, 146:53–136, June 2005.

S. Lépine and A. F. J. Moffat. Direct Spectroscopic Observations of Clumping in O-Star Winds. AJ, 136:548–553, August 2008.

A. Lobel. 3-D radiative transfer modeling of rotational modulations in the blue supergiant J Puppis. In *Massive Stars: From alpha to Omega*, page 43, June 2013.

S. Luehrs. A Colliding-Wind Model for the Wolf-Rayet System HD 152270. PASP, 109:504–513, May 1997.

K. B. MacGregor and J. P. Cassinelli. Magnetic Fields in Massive Stars. II. The Buoyant Rise of Magnetic Flux Tubes through the Radiative Interior. ApJ, 586: 480–494, March 2003.

W. L. F. Marcolino, J.-C. Bouret, J. O. Sundqvist, N. R. Walborn, A. W. Fullerton, I. D. Howarth, G. A. Wade, and A. ud-Doula. Phase-resolved ultraviolet spectroscopy of the magnetic Of?p star HD 191612. MNRAS, 431:2253–2260, May 2013.

N. Markova, J. Puls, T. Repolust, and H. Markov. Bright OB stars in the Galaxy. I. Mass-loss and wind-momentum rates of O-type stars: A pure Hα analysis accounting for line-blanketing. A&A, 413:693–709, January 2004.

B. D. Mason, D. R. Gies, W. I. Hartkopf, W. G. Bagnuolo, Jr., T. ten Brummelaar, and H. A. McAlister. ICCD speckle observations of binary stars. XIX - an astrometric/spectroscopic survey of O stars. AJ, 115:821, February 1998.

D. Massa, A. W. Fullerton, J. S. Nichols, S. P. Owocki, R. K. Prinja, N. St-Louis, A. J. Willis, B. Altner, C. T. Bolton, J. P. Cassinelli, D. Cohen, R. G. Cooper, A. Feldmeier, K. G. Gayley, T. Harries, S. R. Heap, R. N. Henriksen, I. D. Howarth, I. Hubeny, E. Kambe, L. Kaper, G. Koenigsberger, S. Marchenko, S. R. McCandliss, A. F. J. Moffat, T. Nugis, J. Puls, C. Robert, R. E. Schulte-Ladbeck, L. J. Smith, M. A. Smith, W. L. Waldron, and R. L. White. The IUE MEGA Campaign: Wind Variability and Rotation in Early-Type Stars. ApJ, 452:L53, October 1995.

D. Massa and R. K. Prinja. On the Origin of Wind Line Variability in O Stars. ApJ, 809:12, August 2015.

G. Mathys. The Observation of Magnetic Fields in Nondegenerate Stars. Fund. Cosm. Phys., 13:143–308, 1989.

J. M. Matthews, R. Kuschnig, D. B. Guenther, G. A. H. Walker, A. F. J. Moffat, S. M. Rucinski, D. Sasselov, and W. W. Weiss. No stellar p-mode oscillations in space-based photometry of Procyon. Nat, 430:51–53, July 2004.

A. C. Maury and E. C. Pickering. Spectra of bright stars photographed with the 11-inch Draper Telescope as part of the Henry Draper Memorial. *Annals of Harvard College Observatory*, 28:1–128, 1897.

W. H. McCrea. Emissionslinien als Begleiter von Absorptionslinien in Sternspektren. *Zeitschrift fur Physik*, 57:367–379, May 1929.

M. V. McSwain, W. Huang, D. R. Gies, E. D. Grundstrom, and R. H. D. Townsend. The B and Be Star Population of NGC 3766. ApJ, 672:590–603, January 2008.

L. Mestel and N. O. Weiss, editors. *Magnetohydrodynamics*, 1974.

N. Metropolis, A. W. Rosenbluth, M. N. Rosenbluth, A. H. Teller, and E. Teller. Equation of State Calculations by Fast Computing Machines. *J. Chem. Phys*, 21: 1087–1092, March 1953.

A. F. J. Moffat, S. Lepine, R. N. Henriksen, and C. Robert. First wavelet analysis of emission line variations in Wolf-Rayet stars. Ap&SS, 216:55–65, June 1994.

D. J. Mullan. Displaced narrow absorption components in the spectra of mass-losing OB stars - Indications of corotating interaction regions? A&A, 165:157–162, September 1986.

F. Najarro, M. M. Hanson, and J. Puls. L-band spectroscopy of Galactic OB-stars. A&A, 535:A32, November 2011.

C. Neiner and A. Lèbre. The BRITE spectropolarimetric survey. In J. Ballet, F. Martins, F. Bournaud, R. Monier, and C. Reylé, editors, *SF2A-2014: Proceedings of the Annual meeting of the French Society of Astronomy and Astrophysics*, pages 505–508, December 2014.

C. Neiner, S. Mathis, E. Alecian, C. Emeriau, J. Grunhut, BinaMIcS, and MiMeS Collaborations. The origin of magnetic fields in hot stars. In K. N. Nagendra, S. Bagnulo, R. Centeno, and M. Jesús Martínez González, editors, *Polarimetry*, volume 305 of *IAU Symposium*, pages 61–66, October 2015.

N. Netzer and M. Elitzur. The dynamics of stellar outflows dominated by interaction of dust and radiation. ApJ, 410:701–713, June 1993.

S. P. Owocki. Co-Rotating Interaction Regions in 2D Hot-Star Wind Models with Line-Driven Instability. In B. Wolf, O. Stahl, and A. W. Fullerton, editors, *IAU Colloq. 169: Variable and Non-spherical Stellar Winds in Luminous Hot Stars*, volume 523 of *Lecture Notes in Physics, Berlin Springer Verlag*, page 294, 1999.

S. P. Owocki. Stellar winds. In T. D. Oswalt and M. A. Barstow, editors, *Planets, Stars and Stellar Systems. Volume 4: Stellar Structure and Evolution*. 2013.

S. P. Owocki, J. I. Castor, and G. B. Rybicki. Time-dependent models of radiatively driven stellar winds. I - Nonlinear evolution of instabilities for a pure absorption model. ApJ, 335:914–930, December 1988.

S. P. Owocki and G. B. Rybicki. Instabilities in line-driven stellar winds. I - Dependence on perturbation wavelength. ApJ, 284:337–350, September 1984.

S. P. Owocki and G. B. Rybicki. Instabilities in line-driven stellar winds. II - Effect of scattering. ApJ, 299:265–276, December 1985.

E. N. Parker. Dynamics of the Interplanetary Gas and Magnetic Fields. ApJ, 128: 664, November 1958.

E. N. Parker. Dynamical Theory of the Solar Wind. Space Sci.Rev., 4:666–708, September 1965.

A. Pauldrach, J. Puls, and R. P. Kudritzki. Radiation-driven winds of hot luminous stars - Improvements of the theory and first results. A&A, 164:86–100, August 1986.

M. A. C. Perryman, L. Lindegren, J. Kovalevsky, E. Hoeg, U. Bastian, P. L. Bernacca, M. Crézé, F. Donati, M. Grenon, M. Grewing, F. van Leeuwen, H. van der Marel, F. Mignard, C. A. Murray, R. S. Le Poole, H. Schrijver, C. Turon, F. Arenou, M. Froeschlé, and C. S. Petersen. The HIPPARCOS Catalogue. A&A, 323:L49–L52, July 1997.

V. Petit, S. P. Owocki, G. A. Wade, D. H. Cohen, J. O. Sundqvist, M. Gagné, J. Maíz Apellániz, M. E. Oksala, D. A. Bohlender, T. Rivinius, H. F. Henrichs, E. Alecian, R. H. D. Townsend, A. ud-Doula, and MiMeS Collaboration. A magnetic confinement versus rotation classification of massive-star magnetospheres. MNRAS, 429: 398–422, February 2013.

V. Petit and G. A. Wade. Stellar magnetic field parameters from a Bayesian analysis of high-resolution spectropolarimetric observations. MNRAS, 420:773–791, February 2012.

R. K. Prinja. Evidence for rotationally modulated variability in O star winds. MNRAS, 231:21P–24P, March 1988.

R. K. Prinja and I. D. Howarth. Narrow absorption components and variability in ultraviolet P Cygni profiles of early-type stars. ApJS, 61:357–418, June 1986.

R. K. Prinja and I. D. Howarth. Opacity enhancements in the stellar wind of 68 Cygni - Not 'shells' or 'puffs'. MNRAS, 233:123–156, July 1988.

R. K. Prinja, I. D. Howarth, and H. F. Henrichs. Ultraviolet observations of extensive variability in the stellar wind of XI Persei. ApJ, 317:389–411, June 1987.

R. K. Prinja, D. Massa, and A. W. Fullerton. Wind variability of B supergiants. IV. A survey of IUE time-series data of 11 B0 to B3 stars. A&A, 388:587–608, June 2002.

R. K. Prinja, D. L. Massa, M. A. Urbaneja, and R.-P. Kudritzki. PN fast winds: temporal structure and stellar rotation. MNRAS, 422:3142–3150, June 2012.

R. K. Prinja, T. Rivinius, O. Stahl, A. Kaufer, B. H. Foing, J. Cami, and S. Orlando. Photospheric and stellar wind variability in ϵ Ori (B0 Ia). A&A, 418:727–736, May 2004.

J. Puls, R.-P. Kudritzki, A. Herrero, A. W. A. Pauldrach, S. M. Haser, D. J. Lennon, R. Gabler, S. A. Voels, J. M. Vilchez, S. Wachter, and A. Feldmeier. O-star mass-loss and wind momentum rates in the Galaxy and the Magellanic Clouds Observations and theoretical predictions. A&A, 305:171, January 1996.

J. Puls, U. Springmann, and M. Lennon. Radiation driven winds of hot luminous stars. XIV. Line statistics and radiative driving. A&AS, 141:23–64, January 2000.

D. N. Rachkovsky. A system of radiative transfer equations in the presence of a magnetic field. *Izvestiya Ordena Trudovogo Krasnogo Znameni Krymskoj Astrofizicheskoj Observatorii*, 26:63–73, 1961.

A. I. M. Rae. *Quantum Mechanics, Fourth edition*. IOP Publishing, 2002.

T. Ramiaramanantsoa, A. F. J. Moffat, A.-N. Chené, N. D. Richardson, H. F. Henrichs, S. Desforges, V. Antoci, J. F. Rowe, J. M. Matthews, R. Kuschnig, W. W. Weiss, D. Sasselov, S. M. Rucinski, and D. B. Guenther. MOST detects corotating bright spots on the mid-O-type giant ξ Persei. MNRAS, 441:910–917, June 2014.

B. C. Reed. Catalog of Galactic OB Stars. AJ, 125:2531–2533, May 2003.

A. H. N. Reid and I. D. Howarth. Optical time-series spectroscopy of the O4 supergiant ζ Puppis. A&A, 311:616–630, July 1996.

T. Repolust, J. Puls, and A. Herrero. Stellar and wind parameters of Galactic O-stars. The influence of line-blocking/blanketing. A&A, 415:349–376, February 2004.

H. B. Richer, J. Anderson, J. Brewer, S. Davis, G. G. Fahlman, B. M. S. Hansen, J. Hurley, J. S. Kalirai, I. R. King, D. Reitzel, R. M. Rich, M. M. Shara, and P. B. Stetson. Probing the Faintest Stars in a Globular Star Cluster. *Science*, 313: 936–940, August 2006.

S. Rosseland. Viscosity in the stars. MNRAS, 89:49–53, November 1928.

H. Saio, R. Kuschnig, A. Gautschy, C. Cameron, G. A. H. Walker, J. M. Matthews, D. B. Guenther, A. F. J. Moffat, S. M. Rucinski, D. Sasselov, and W. W. Weiss. MOST Detects g- and p-Modes in the B Supergiant HD 163899 (B2 Ib/II). ApJ, 650:1111–1118, October 2006.

M. Scardia. Micrometric measurements of binary stars (first list). A&AS, 53:433–440, September 1983.

R. S. Schnerr, H. F. Henrichs, C. Neiner, E. Verdugo, J. de Jong, V. C. Geers, K. Wiersema, B. van Dalen, A. Tijani, B. Plaggenborg, and K. L. J. Rygl. Magnetic field measurements and wind-line variability of OB-type stars. A&A, 483:857–867, June 2008.

C. Schrijvers, J. H. Telting, C. Aerts, E. Ruymaekers, and H. F. Henrichs. Line-profile

variations due to adiabatic non-radial pulsations in rotating stars. I. Observable characteristics of spheroidal modes. A&AS, 121, February 1997.

F. Schwabl. *Quantum Mechanics, Fourth Edition*. Springer-Verlag, 2007.

K. Schwarzschild. Ueber die totale Sonnenfinsternis vom 30. August 1905. *Astronomische Mitteilungen der Universitaets-Sternwarte zu Goettingen*, 13, 1906.

S. C. Searle, R. K. Prinja, D. Massa, and R. Ryans. Quantitative studies of the optical and UV spectra of Galactic early B supergiants. I. Fundamental parameters. A&A, 481:777–797, April 2008.

M. Shultz, G. A. Wade, V. Petit, J. Grunhut, C. Neiner, D. Hanes, and MiMeS Collaboration. An observational evaluation of magnetic confinement in the winds of BA supergiants. MNRAS, 438:1114–1126, February 2014.

J. Silvester, O. Kochukhov, and G. A. Wade. Stokes IQUV magnetic Doppler imaging of Ap stars - II. Next generation magnetic Doppler imaging of α^2 CVn. MNRAS, 440:182–192, May 2014.

S. Simón-Díaz, N. Castro, M. Garcia, A. Herrero, and N. Markova. The IACOB spectroscopic database of Northern Galactic OB stars. *Bulletin de la Societe Royale des Sciences de Liege*, 80:514–518, January 2011.

S. Simón-Díaz and A. Herrero. Fourier method of determining the rotational velocities in OB stars. A&A, 468:1063–1073, June 2007.

N. Smith and D. J. Frew. A revised historical light curve of Eta Carinae and the timing of close periastron encounters. MNRAS, 415:2009–2019, August 2011.

V. V. Sobolev. *Moving envelopes of stars*. 1960.

N. Spaldin. *Magnetic Materials : Fundamentals and Device Applications*. Cambridge University Press, 2003.

H. C. Spruit. Dynamo action by differential rotation in a stably stratified stellar interior. A&A, 381:923–932, January 2002.

O. Stahl, A. Kaufer, T. Rivinius, T. Szeifert, B. Wolf, T. Gaeng, C. A. Gummersbach, I. Jankovics, J. Kovacs, H. Mandel, M. W. Pakull, and J. Peitz. Phase-locked photospheric and stellar-wind variations of θ^1 Orionis C. A&A, 312:539–548, August 1996.

D. W. N. Stibbs. A study of the spectrum and magnetic variable star HD 125248. MNRAS, 110:395, 1950.

J. O. Sundqvist and S. P. Owocki. Clumping in the inner winds of hot, massive stars from hydrodynamical line-driven instability simulations. MNRAS, 428:1837–1844, January 2013.

J. O. Sundqvist, V. Petit, S. P. Owocki, G. A. Wade, J. Puls, and MiMeS Collaboration. On magnetic inhibition of photospheric macroturbulence generated in the iron-bump opacity zone of O-stars. MNRAS, 433:2497–2501, August 2013.

J. O. Sundqvist, A. ud-Doula, S. P. Owocki, R. H. D. Townsend, I. D. Howarth, and G. A. Wade. A dynamical magnetosphere model for periodic Hα emission from the slowly rotating magnetic O star HD 191612. MNRAS, 423:L21–L25, June 2012.

R. J. Tayler. The adiabatic stability of stars containing magnetic fields-I.Toroidal fields. MNRAS, 161:365, 1973.

A. ud-Doula and S. P. Owocki. Dynamical Simulations of Magnetically Channeled Line-driven Stellar Winds. I. Isothermal, Nonrotating, Radially Driven Flow. ApJ, 576:413–428, September 2002.

A. Ud-Doula, S. P. Owocki, and R. H. D. Townsend. Dynamical simulations of magnetically channelled line-driven stellar winds - III. Angular momentum loss and rotational spin-down. MNRAS, 392:1022–1033, January 2009.

W. Unno. Line Formation of a Normal Zeeman Triplet. PASJ, 8:108, 1956.

I. G. Usoskin, S. V. Berdyugina, and J. Poutanen. Preferred sunspot longitudes: non-axisymmetry and differential rotation. A&A, 441:347–352, October 2005.

J. S. Vink, A. de Koter, and H. J. G. L. M. Lamers. Mass-loss predictions for O and B stars as a function of metallicity. A&A, 369:574–588, April 2001.

S. S. Vogt and G. D. Penrod. Doppler Imaging of spotted stars - Application to the RS Canum Venaticorum star HR 1099. PASP, 95:565–576, September 1983.

G. A. Wade, J.-F. Donati, J. D. Landstreet, and S. L. S. Shorlin. High-precision magnetic field measurements of Ap and Bp stars. MNRAS, 313:851–867, April 2000.

G. A. Wade, J. Grunhut, E. Alecian, C. Neiner, M. Aurière, D. A. Bohlender, A. David-Uraz, C. Folsom, H. F. Henrichs, O. Kochukhov, S. Mathis, S. Owocki, V. Petit, and Petit. The magnetic characteristics of Galactic OB stars from the MiMeS survey of magnetism in massive stars. In P. Petit, M. Jardine, and H. C. Spruit, editors, *IAU Symposium*, volume 302 of *IAU Symposium*, pages 265–269, August 2014.

G. A. Wade, I. D. Howarth, R. H. D. Townsend, J. H. Grunhut, M. Shultz, J.-C. Bouret, A. Fullerton, W. Marcolino, F. Martins, Y. Nazé, A. Ud Doula, N. R. Walborn, and J.-F. Donati. Confirmation of the magnetic oblique rotator model for the Of?p star HD 191612. MNRAS, 416:3160–3169, October 2011.

G. A. Wade, J. Maíz Apellániz, F. Martins, V. Petit, J. Grunhut, N. R. Walborn, R. H. Barbá, M. Gagné, E. García-Melendo, J. Jose, A. F. J. Moffat, Y. Nazé, C. Neiner, A. Pellerin, M. Penadés Ordaz, M. Shultz, S. Simón-Díaz, and A. Sota. NGC 1624-2: a slowly rotating, X-ray luminous Of?cp star with an extraordinarily strong magnetic field. MNRAS, 425:1278–1293, September 2012.

G. A. Wade, C. Neiner, E. Alecian, J. H. Grunhut, V. Petit, B. d. Batz, D. A. Bohlender, D. H. Cohen, H. F. Henrichs, O. Kochukhov, J. D. Landstreet, N. Manset, F. Martins, S. Mathis, M. E. Oksala, S. P. Owocki, T. Rivinius, M. E. Shultz, J. O. Sundqvist, R. H. D. Townsend, A. ud-Doula, J.-C. Bouret, J. Braithwaite, M. Briquet, A. C. Carciofi, A. David-Uraz, C. P. Folsom, A. W. Fullerton, B. Leroy, W. L. F. Marcolino, A. F. J. Moffat, Y. Nazé, N. S. Louis, M. Aurière, S. Bagnulo, J. D. Bailey, R. H. Barbá, A. Blazère, T. Böhm, C. Catala, J.-F. Donati, L. Ferrario, D. Harrington, I. D. Howarth, R. Ignace, L. Kaper, T. Lüftinger, R. Prinja, J. S. Vink, W. W. Weiss, and I. Yakunin. The MiMeS survey of magnetism in massive stars: introduction and overview. MNRAS, 456:2–22, February 2016.

G. A. Wade and the MiMeS Collaboration. The MiMeS Project: Current status and recent results. *ArXiv e-prints*, December 2010.

G. Walker, J. Matthews, R. Kuschnig, R. Johnson, S. Rucinski, J. Pazder, G. Burley, A. Walker, K. Skaret, R. Zee, S. Grocott, K. Carroll, P. Sinclair, D. Sturgeon, and

J. Harron. The MOST Asteroseismology Mission: Ultraprecise Photometry from Space. PASP, 115:1023–1035, September 2003.

G. A. H. Walker, R. Kuschnig, J. M. Matthews, P. Reegen, T. Kallinger, E. Kambe, H. Saio, P. Harmanec, D. B. Guenther, A. F. J. Moffat, S. M. Rucinski, D. Sasselov, W. W. Weiss, D. A. Bohlender, H. Božić, O. Hashimoto, P. Koubský, R. Mann, D. Ruždjak, P. Škoda, M. Šlechta, D. Sudar, M. Wolf, and S. Yang. Pulsations of the Oe Star ζ Ophiuchi from MOST Satellite Photometry and Ground-based Spectroscopy. ApJ, 623:L145–L148, April 2005.

R. Weaver, R. McCray, J. Castor, P. Shapiro, and R. Moore. Interstellar bubbles. II - Structure and evolution. ApJ, 218:377–395, December 1977.

W. W. Weiss, S. M. Rucinski, A. F. J. Moffat, A. Schwarzenberg-Czerny, O. F. Koudelka, C. C. Grant, R. E. Zee, R. Kuschnig, S. Mochnacki, J. M. Matthews, P. Orleanski, A. Pamyatnykh, A. Pigulski, J. Alves, M. Guedel, G. Handler, G. A. Wade, and K. Zwintz. BRITE-Constellation: Nanosatellites for Precision Photometry of Bright Stars. PASP, 126:573–585, June 2014.

J. N. Winn, J. M. Matthews, R. I. Dawson, D. Fabrycky, M. J. Holman, T. Kallinger, R. Kuschnig, D. Sasselov, D. Dragomir, D. B. Guenther, A. F. J. Moffat, J. F. Rowe, S. Rucinski, and W. W. Weiss. A Super-Earth Transiting a Naked-eye Star. ApJ, 737:L18, August 2011.

P. Zeeman. On the Influence of Magnetism on the Nature of the Light Emitted by a Substance. ApJ, 5:332, May 1897.

Appendices

Appendix A

Additional observational data

This appendix contains a table of all the observations used in Chapter 4.

Table A.1: Full list of nightly observations for each star. The date is given in universal time (UT), B_z is the nightly measured longitudinal magnetic field value, σ_{B_z} is the nightly error bar on the longitudinal field, $N_{\rm obs}$ is the number of observations and the last column indicates whether they were obtained with ESPaDOnS (E) or NARVAL (N).

Name	Night	B_z (G)	σ_{B_z} (G)	$N_{\rm obs}$	E/N
ξ Per	10 Dec. 2006	19	41	3	N
ξ Per	13 Dec. 2006	-10	36	3	N
ξ Per	14 Dec. 2006	49	42	3	N
ξ Per	15 Dec. 2006	28	22	7	N
ξ Per	16 Dec. 2006	-25	138	1	N
ξ Per	06 Sep. 2007	5	25	7	N
ξ Per	07 Sep. 2007	-10	21	6	N
ξ Per	08 Sep. 2007	-20	26	4	N
ξ Per	09 Sep. 2007	32	48	2	N
ξ Per	10 Sep. 2007	59	55	1	N
ξ Per	11 Sep. 2007	46	61	1	N
ξ Per	12 Sep. 2007	41	70	1	N
ξ Per	01 Nov. 2011	-15	48	5	E
α Cam	13 Dec. 2006	64	35	1	N
α Cam	21 Dec. 2007	2	10	4	E

Continued on next page

Table A.1 – *Continued from previous page*

Name	Night	B_z (G)	σ_{B_z} (G)	$N_{\rm obs}$	E/N
α Cam	14 Nov. 2010	11	20	2	E
α Cam	31 Dec. 2012	6	24	1	E
α Cam	01 Jan. 2013	11	25	3	E
HD 34656	11 Nov. 2011	-35	38	1	E
λ Ori A	21 Dec. 2007	-15	23	2	E
λ Ori A	18 Jan. 2008	36	46	1	E
λ Ori A	22 Jan. 2008	-14	22	2	E
λ Ori A	14 Oct. 2008	31	33	2	N
λ Ori A	26 Oct. 2008	17	15	7	N
λ Ori A	15 Mar. 2009	17	30	1	N
λ Ori A	17 Mar. 2009	12	25	1	N
λ Ori A	16 Oct. 2010	-2	12	4	E
ϵ Ori	15 Oct. 2007	44	75	1	N
ϵ Ori	17 Oct. 2007	-34	29	6	N
ϵ Ori	18 Oct. 2007	-3	6	28	N
ϵ Ori	21 Oct. 2007	2	10	8	N
ϵ Ori	24 Oct. 2007	17	13	6	N
ϵ Ori	13 Oct. 2008	20	9	9	E
ϵ Ori	25 Oct. 2008	-2	13	10	N
ϵ Ori	15 Mar. 2009	26	35	1	N
ϵ Ori	16 Mar. 2009	4	25	1	N
15 Mon	10 Dec. 2006	-9	50	1	N
15 Mon	15 Dec. 2006	-3	27	1	N
15 Mon	09 Sep. 2007	-17	39	1	N
15 Mon	10 Sep. 2007	-1	30	1	N
15 Mon	11 Sep. 2007	-22	44	1	N
15 Mon	20 Oct. 2007	-2	26	4	N
15 Mon	23 Oct. 2007	16	24	4	N
15 Mon	03 Feb. 2012	0	20	3	E
HD 64760	21 Nov. 2010	51	37	6	E
HD 64760	31 Dec. 2012	15	59	3	E
ζ Pup	14 Feb. 2012	-12	21	30	E
ζ Oph	18 Mar. 2011	92	438	1	N
ζ Oph	21 Mar. 2011	-336	361	1	N
ζ Oph	05 Apr. 2011	-266	406	1	N
ζ Oph	08 Jun. 2011	-134	118	20	E

Continued on next page

Table A.1 – *Continued from previous page*

Name	Night	B_z (G)	σ_{B_z} (G)	$N_{\rm obs}$	E/N
ζ Oph	10 Jun. 2011	417	423	1	N
ζ Oph	13 Jun. 2011	-261	426	1	N
ζ Oph	14 Jun. 2011	34	310	1	N
ζ Oph	15 Jun. 2011	106	377	1	N
ζ Oph	04 Jul. 2011	-206	302	1	N
ζ Oph	07 Jul. 2011	127	411	1	N
ζ Oph	10 Jul. 2011	170	342	1	N
ζ Oph	11 Jul. 2011	-51	320	1	N
ζ Oph	10 Aug. 2011	-9	315	1	N
ζ Oph	11 Aug. 2011	120	345	1	N
ζ Oph	15 Aug. 2011	242	374	1	N
ζ Oph	16 Aug. 2011	174	335	1	N
ζ Oph	17 Aug. 2011	-85	349	1	N
ζ Oph	18 Aug. 2011	-77	579	1	N
ζ Oph	20 Aug. 2011	-82	418	1	N
ζ Oph	21 Aug. 2011	-91	297	1	N
ζ Oph	22 Aug. 2011	108	499	1	N
ζ Oph	23 Aug. 2011	14	295	1	N
ζ Oph	26 Aug. 2011	455	685	1	N
ζ Oph	27 Aug. 2011	-277	524	1	N
ζ Oph	28 Aug. 2011	769	840	1	N
ζ Oph	16 Jan. 2012	-476	446	1	N
ζ Oph	17 Jan. 2012	-444	383	1	N
ζ Oph	24 Jan. 2012	-52	317	1	N
ζ Oph	25 Jan. 2012	41	282	1	N
ζ Oph	27 Jan. 2012	-126	596	1	N
ζ Oph	21 Jun. 2012	39	351	1	N
ζ Oph	22 Jun. 2012	185	316	1	N
ζ Oph	23 Jun. 2012	380	298	1	N
ζ Oph	09 Jul. 2012	409	348	1	N
ζ Oph	12 Jul. 2012	152	369	1	N
ζ Oph	06 Aug. 2012	-132	321	1	N
ζ Oph	07 Aug. 2012	75	382	1	N
ζ Oph	08 Aug. 2012	-248	335	1	N
ζ Oph	09 Aug. 2012	171	413	1	N
ζ Oph	12 Aug. 2012	-171	491	1	N

Continued on next page

Table A.1 – *Continued from previous page*

Name	Night	B_z (G)	σ_{B_z} (G)	$N_{\rm obs}$	E/N
ζ Oph	14 Aug. 2012	462	361	1	N
ζ Oph	16 Aug. 2012	-161	474	1	N
ζ Oph	17 Aug. 2012	-143	413	1	N
ζ Oph	18 Aug. 2012	-572	448	1	N
ζ Oph	19 Aug. 2012	-178	403	1	N
ζ Oph	20 Aug. 2012	56	383	1	N
68 Cyg	16 Dec. 2006	131	479	1	N
68 Cyg	10 Sep. 2007	80	101	1	N
68 Cyg	12 Nov. 2007	-106	197	1	N
68 Cyg	29 Sep. 2012	-11	46	5	E
19 Cep	13 Dec. 2006	-20	44	1	N
19 Cep	09 Nov. 2007	9	59	1	N
19 Cep	13 Nov. 2007	-129	97	1	N
19 Cep	22 Dec. 2007	-8	22	3	E
19 Cep	21 Jun. 2008	-57	28	5	N
19 Cep	22 Jun. 2008	9	20	5	N
19 Cep	25 Jun. 2008	2	24	3	N
19 Cep	27 Jun. 2008	-18	17	5	N
19 Cep	28 Jun. 2008	-5	19	5	N
19 Cep	26 Jul. 2010	23	36	4	E
λ Cep	13 Dec. 2006	64	79	1	N
λ Cep	07 Jul. 2011	-100	63	1	N
λ Cep	08 Jul. 2011	36	60	1	N
λ Cep	10 Aug. 2011	-15	65	1	N
λ Cep	27 Aug. 2011	-56	83	1	N
λ Cep	28 Aug. 2011	-2	67	1	N
λ Cep	16 Jun. 2012	4	95	1	N
λ Cep	22 Jun. 2012	-64	68	1	N
λ Cep	24 Jun. 2012	31	92	1	N
λ Cep	09 Jul. 2012	-37	78	1	N
λ Cep	18 Jul. 2012	38	63	1	N
λ Cep	19 Jul. 2012	-9	66	1	N
λ Cep	22 Jul. 2012	-20	67	1	N
λ Cep	23 Jul. 2012	10	67	1	N
λ Cep	24 Jul. 2012	7	62	1	N
λ Cep	06 Aug. 2012	88	57	1	N

Continued on next page

Table A.1 – *Continued from previous page*

Name	Night	B_z (G)	σ_{B_z} (G)	$N_{\rm obs}$	E/N
λ Cep	07 Aug. 2012	-149	80	1	N
λ Cep	08 Aug. 2012	53	67	1	N
λ Cep	09 Aug. 2012	41	58	1	N
λ Cep	11 Aug. 2012	-12	126	1	N
λ Cep	12 Aug. 2012	85	103	1	N
λ Cep	13 Aug. 2012	-66	65	1	N
λ Cep	15 Aug. 2012	-11	97	1	N
λ Cep	16 Aug. 2012	62	86	1	N
λ Cep	17 Aug. 2012	-13	86	1	N
λ Cep	18 Aug. 2012	173	149	1	N
10 Lac	10 Dec. 2006	-6	7	1	N
10 Lac	11 Dec. 2006	-1	7	1	N
10 Lac	13 Dec. 2006	8	8	1	N
10 Lac	14 Dec. 2006	-6	7	1	N
10 Lac	15 Dec. 2006	8	6	1	N
10 Lac	16 Dec. 2006	11	9	1	N
10 Lac	07 Sep. 2007	-2	6	1	N
10 Lac	15 Oct. 2007	9	6	3	N
10 Lac	16 Oct. 2007	12	6	3	N
10 Lac	17 Oct. 2007	1	4	3	N
10 Lac	18 Oct. 2007	-6	8	3	N
10 Lac	19 Oct. 2007	-6	4	3	N
10 Lac	20 Oct. 2007	1	4	3	N
10 Lac	21 Oct. 2007	5	5	3	N
10 Lac	23 Oct. 2007	2	5	3	N
10 Lac	24 Oct. 2007	-3	4	3	N
10 Lac	06 Nov. 2007	-14	14	1	N
10 Lac	26 Jul. 2008	9	10	1	E